Thomas Potocar

Nucleation and layer growth of para-hexaphenyl on sputtered mica(001)

MASTER THESIS

For obtaining the academic degree
Diplom - Ingenieur

Diploma Programme of Technical Physics

Graz University of Technology

Supervisor:
Ao.Univ.-Prof. Dipl.-Ing. Dr.techn. Adolf Winkler
Institute of Solid State Physics

Graz, June 2010

Thomas Potocar

Nukleation und Schichtwachstum von para-Hexaphenyl auf einer gesputterten Glimmer(001) Oberfläche

DIPLOMARBEIT

zur Erlangung des akademischen Grades
Diplom-Ingenieur

Diplomstudium Technische Physik

Graz University of Technology
Technische Universität Graz

Betreuer:

Ao.Univ.-Prof. Dipl.-Ing. Dr.techn. Adolf Winkler

Institut für Festkörperphysik

Graz, Juni 2010

Deutsche Fassung:
Beschluss der Curricula-Kommission für Bachelor-, Master- und Diplomstudien vom 10.11.2008
Genehmigung des Senates am 1.12.2008

EIDESSTATTLICHE ERKLÄRUNG

Ich erkläre an Eides statt, dass ich die vorliegende Arbeit selbstständig verfasst, andere als die angegebenen Quellen/Hilfsmittel nicht benutzt, und die den benutzten Quellen wörtlich und inhaltlich entnommene Stellen als solche kenntlich gemacht habe.

Graz, am …… ……..
(Unterschrift)

Englische Fassung:

STATUTORY DECLARATION

I declare that I have authored this thesis independently, that I have not used other than the declared sources / resources, and that I have explicitly marked all material which has been quoted either literally or by content from the used sources.

…… ……..
date (signature)

Acknowledgment

This master thesis was written at the Institute of Solid State Physics, Technical University of Graz, in cooperation with the Institute of Physics, University of Leoben.
I specially would like to thank my supervisor Adolf Winkler for his great support and also the whole institute, inter alia Paul Frank, Frederik Weber and Martin Kornschober. Great thanks also go to Stefan Lorbek, Quan Shen and Christian Teichert from the University of Leoben for helpful ideas and the AFM measurements.
Additionally, I have to acknowledge my family and Elisabeth Fabian, as well as the Austrian Science Fund (FWF, Proj. No. P19197) for financial support.

Abstract

The morphology and structure of thin organic films are of utmost importance for the proper functioning of novel organic electronics, e.g. light emitting diodes (LEDs), displays, transistors, solar cells or sensors. The initial stages of layer growth are not entirely understood, for instance whether the well established model for inorganic film growth can also be applied to the nucleation and growth of large organic molecules.
In this work we focus on the nucleation and sub-monolayer growth of para-hexaphenyl (6P) on a Ar^+ sputtered mica(001) surface. 6P is a rod like organic molecule which can be used e.g. for blue LEDs and nano optic devices. The modification of the mica surface by sputtering leads to the formation of mounds, composed of standing molecules instead of needle like islands consisting of flat lying molecules on top of a wetting layer (complete monolayer) of also flat lying molecules. First the island shapes, densities, heights and molecule orientation were investigated by atomic force microscopy and transverse shear microscopy at samples with different coverages, temperatures and growth rates. The main issue of this work is the determination of the critical island size. The critical island size governs the further layer growth and depends on the inter-molecular forces between the monomers of the film material and the substrate. Thus, the manipulation of the critical island size is of great importance for the final structure and morphology of the film. Three different ways to determine this were performed here. The variation of the growth rate, the island area distribution and finally the capture zones area distribution have been used.
The experiments were done under ultra-high vacuum conditions. The following experimental techniques were used: Auger electron spectroscopy (AES), quartz microbalance, thermal desorption spectroscopy (TDS) and also ex-situ atomic force microscopy (AFM) and transverse shear microscopy (TSM).

Kurzfassung

Die Morphologie und Struktur dünner organischer Schichten ist von wesentlicher Bedeutung für die Funktionalität organischer elektronischer Bauteile, wie zum Beispiel Leuchtdioden (LEDs), Displays, Transistoren, Solar Zellen und Sensoren. Das Anfangsstadium des Schichtwachstums ist noch nicht völlig verstanden, diesbezüglich auch die Frage ob Verfahren des anorganischen Wachstums für organische Moleküle übernommen werden können.
Im Rahmen dieser Diplomarbeit haben wir uns mit der Nukleation und dem Sub-Monolayer Wachstum von para-Hexaphenyl (6P) auf der mit Ar^+ Ionen gesputterten Oberfläche von Glimmer(001) beschäftigt. 6P ist ein stäbchenförmiges organisches Molekül, bestehend aus sechs Phenylringen, welches unter anderem für blau leuchtende LEDs verwendet werden kann. Die Veränderung der Glimmeroberfläche durch Sputtern führt zur Bildung von Inseln, die sich aus aufrechtstehenden Molekülen zusammensetzen, wohingegen sich auf einer nichtgesputteren Oberfläche ein wetting layer (volle Monolage) aus flach liegenden Molekülen ausbildet, auf dem sich nadelförmige Inseln mit ebenfalls flach liegenden Molekülen befinden. Zunächst wurde das Wachstum der Inseln bezüglich ihrer Form, Dichte, Höhe und Molekülorientierung bei unterschiedlicher Bedeckung, Temperatur und Aufdampfrate untersucht. Die Hauptaufgabe dieser Arbeit lag dabei in der Bestimmung der kritischen Inselgröße (d.h. der Anzahl der Moleküle, die notwendig sind um einen stabilen Keim zu bilden, minus eins). Die kritische Inselgröße legt das weitere Wachstum der Schicht fest, sie hängt ab von den Kräften, die zwischen den Molekülen untereinander sowie zwischen den Molekülen und dem Substrat herrschen. Hierfür wurden drei verschiedene Berechnungsmethoden verwendet, erstens mittels unterschiedlicher Aufdampfraten, zweitens über die Verteilung der Inselgrössen und schließlich durch die Verteilung der Grössen der Einfangzonen der Inseln.
Die Experimente wurden unter ultrahochvakuum Bedingungen durchgeführt. Folgende Messmethoden kamen dabei zur Anwendung: Augerspektroskopie (AES), Schwingquarz zur Schichtdickenmessung, Thermodesorptionsspektroskopie (TDS), sowie ex-situ Rasterkraftmikroskopie (AFM) und Transverse Shear Mikroskopie (TSM).

Contents

Symbols and abbreviations

α-peak ... Multilayer peak, desorption of zero order
β-peak ... Monolayer peak, desorption of first order
Θ ... Coverage
6P ... Para-hexaphenyl
acc. to ... According to
AES ... Auger electron spectroscopy
AFM ... Atomic force microscopy
chap ... Chapter
corr. ... Corrected
DLA ... Diffusion limited aggregation
E_{Des} ... Desorption energy
equ ... Equation
eV ... Electron volt ($1\ eV = 1.602 \cdot 10^{-19}\ J$)
fig ... Figure
f(u) ... Scaling function
i ... Critical cluster size for nucleation
LED ... Light emitting diode
LN_2 ... Liquid nitrogen
ML ... Monolayer
MW ... Average value
pos ... Position
PVD ... Physical vapour deposition
QMS ... Quadrupole mass spectrometer
r ... Growth rate
R ... Gas constant ($R = 2\ cal/(mol \cdot K)$)
SEM ... Scanning electron microscope
T ... Temperature
t ... (Deposition) time
tab ... Table
TMP ... Turbo molecular pump
TSM ... Transverse shear microscopy
TDS ... Thermal desorption spectroscopy
u ... Atomic mass unit ($1\ u = 1.66 \cdot 10^{-27}\ kg$)
UHV ... Ultra-high vacuum
uncorr. ... Uncorrected

1. Introduction

Thin organic films have attracted enormous interest in the recent years because of their importance for novel organic electronics, e.g. light emitting diodes (LEDs), displays, transistors, solar cells or sensors [1], [2], [3]. Although there exist already many applications, there is still a considerable lack in the basic understanding of film formation.
In this work we consider the initial stages of the layer growth from para-hexaphenyl (6P) on mica(001).
Para-hexaphenyl is a rod like organic molecule, which shows blue electroluminescence and can be easily evaporated in ultra-high vacuum by molecular beam Knudsen cells.
Mica is a popular substrate material for epitaxial layer growth investigations. It can be easily cleaved and is thermally stable up to 1000 K. The mica surface was modified via Ar^+ sputtering, because this leads to another growth behaviour [4].
The main issue of this work is the determination of the critical island size, since this governs the further layer growth. Three different ways to determine this were performed here. In chap.4.3.1 the variation of the growth rate, in chap.4.3.2 the island area distribution and in chap.4.3.3 the capture zones area distribution have been used.
For this purpose different samples with different coverages (chap.4.2.1), temperatures (chap.4.2.2) and growth rates (chap.4.2.3) were produced and investigated by ex-situ atomic force microscopy (AFM) and transverse shear microscopy (TSM). For the film preparation under ultra-high vacuum conditions (UHV), the following in-situ experimental techniques were used: Auger electron spectroscopy (AES), quartz microbalance, thermal desorption spectroscopy (TDS).

2. Theoretical background

2.1. Properties of para-hexaphenyl

Para-hexaphenyl is an aromatic hydrocarbon, which is also denoted as sexiphenyl, p-hexaphenyl, 6P, PHP, PSP, p-6P. In the following text, mainly the abbreviation 6P will be used. This rod like molecule (fig.2.1(a)) has a length of 2.7 nm and consists of six phenyl rings in para arrangement, where the opposite ends of the phenyl ring are occupied as shown in fig.2.1(b). In the gas phase the phenyl rings are skews against each other, whereas in the crystallized state the phenyl rings lie in one plane. The organic molecule para-hexaphenyl, made up of 36 carbon- and 26 hydrogen- atoms, has a mass of $m_{mol} = 458\ u$. But for the thermal desorption spectroscopy (TDS, chap.2.5.4) the mass 61 (C_5H) was used, which is a cracking product of 6P, because this showed the largest signal of the cracking pattern in the QMS. The condensed phase of 6P has a centered monoclinic unit cell (fig.2.1(c)) with the lattice constants:

$$a = 8.091\ \mathring{A},\ b = 5.568\ \mathring{A},\ c = 26.241\ \mathring{A},\ \alpha = 98.17°$$

The ground plane shows the herringbone structure of the molecules in top view (fig.2.1(d)).

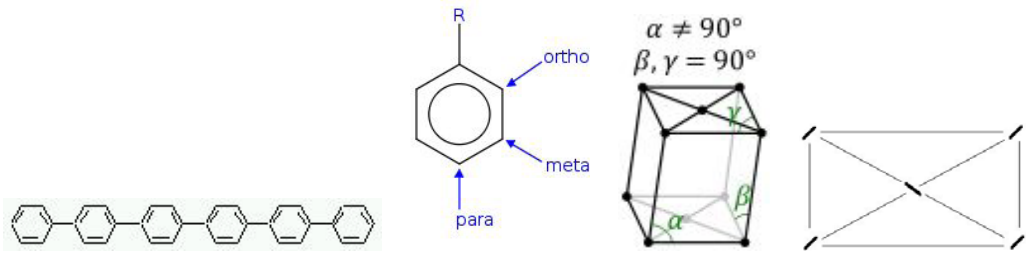

(a) Rod like 6P (b) Phenyl ring (c) Unit cell (d) Unit cell ground plane

Figure 2.1.: **Para-hexaphenyl.** (a) The rod like 6P molecule has a lenght of 2.7 nm. (b) In para arrangement the opposite ends of the phenyl ring are occupied. (c) Centered monoclinic unit cell with grid constants $a = 8.091\ \mathring{A}$, $b = 5.568\ \mathring{A}$, $c = 26.241\ \mathring{A}$, $\alpha = 98.17°$. (d) The ground plane of the centered monoclinic unit cell shows a top view of the molecules in herringbone arrangement.

2.2. Properties of mica

Mica[1] is a common rock-forming mineral, which exists in various types - for instance [5]:

- Potash mica (muskovite): $KAl_2[AlSi_3O_{10}](OH,F)_2$
- Magnesia mica (biotite): $K(Mg,Fe^{II})_3[AlSi_3O_{10}](OH,F_2)$
- Lithion mica (lepidolithe): $(K,Li)Al_2[AlSi_3O_{10}](OH,F)_2$ (in isomorphic mixture with potash mica)
- Lithion iron mica (zinnwaldite): mixed crystals of magnesia and lithion mica

(OH,F_2) e.g. means that either OH or F_2 exists on this site. The here used mica muskovite consists of potassium, aluminium, silicon and oxygen in the following chemical compound:

$$KAl_2(AlSi_3)O_{10}(OH)_2$$

The particles are arranged in a layer structure, according to fig.2.3, one can see the monoclinic crystal system with the lattice plane (001) in side view, the distance between plane A and B is 10 $\mathring{A}$. After cleaving (along plane A or B), the surface consists of potassium. The crystal system is monoclinic with the lattice constants:

$$a = 5.1998\ \mathring{A},\ b = 9.0266\ \mathring{A},\ c = 20.1058\ \mathring{A},\ \alpha = 95.782^\circ$$

Industrially, mica is used for example as substitute of glass, electrical isolator or dielectric in capacitors. In fig.2.2, mica is shown in it's natural appearance.

Figure 2.2.: **Mica muskovite** in nature.

[1]The german name is 'Glimmer' and also known as 'Katzensilber' or 'Katzengold'. The english notation comes from the latin 'micare', to glitter.

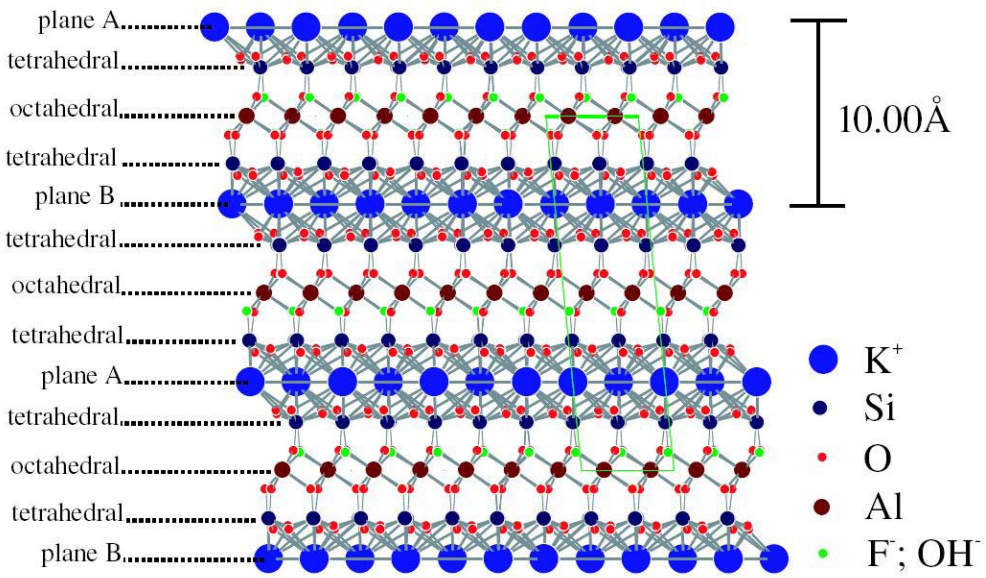

Figure 2.3.: **The mica is arranged in a layer structure.** One can see the crystal structure (monoclinic) of mica muskovite with the lattice plane (001) in side view. After cleaving (plane A or B), the potassium forms the surface. In this work mica with OH and not F was used [4].

2.3. Growth behaviour

2.3.1. Growth modes

One can distinguish between three possible modes of crystal growth on surfaces as illustrated in fig.2.4 at three different coverages Θ denoted in monolayer ML [6].

Frank van der Merwe growth
In (a) the 'layer' or 'Frank van der Merwe' growth mode is shown, in this connection the atoms (or molecules) of the deposit are more strongly bound to the substrate, than to each other. First, a wetting layer (complete monolayer) is formed on the surface, the following layers are less tightly bound (monotonic decrease), toward the value for a bulk crystal of the deposit. This growth mode occurs in the case of adsorbed gases on graphite and on several metals, in some metal-metal and semiconductor-semiconductor systems.

Stranski-Krastanov growth
At the 'layer plus island' or 'Stranski-Krastanov' growth mode (b) a wetting layer is formed on the substrate. With increasing coverage islands are formed on the top of this layer. This growth mode occurs in metal-metal, metal-semiconductor and gas-metal systems including 6P on unsputtered mica.

Volmer-Weber growth
In the 'island' or 'Volmer-Weber' growth mode (c), islands are formed directly on the substrate surface. The atoms (or molecules) of the deposit are more strongly bound to each other than to the substrate. This growth mode occurs in many systems of metals on insulators and also 6P on sputtert mica.

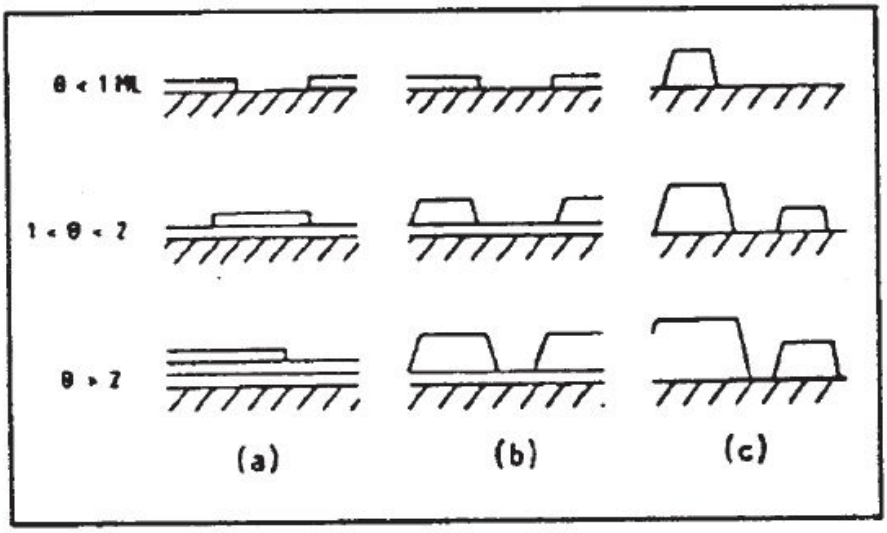

Figure 2.4.: **Sketch of the three crystal growth modes.** (a) 'Frank van der Merwe' or 'layer' growth, (b) 'Stranski-Krastanov' or 'layer plus island' growth, (c) 'Volmer-Weber' or 'island' growth, Θ... Coverage/ML [6].

2.3.2. Diffusion limited aggregation

The growth of islands can often be described by diffusion limited aggregation (DLA) [7], [8]. In this model, the islands grow by sticking of diffusing particles, if they contact the cluster. The fractal dimension of this islands is about 1.6 [9].
In fig.2.5 the computer model of a fractal island with 3600 particles from the classical DLA (hit and stick process) is shown. A simulation of this growth is given in Ref. [10].

The real growth of submonolayer islands differs from that in two important points [11]:

- Edge diffusion (atoms relax to a lower energy site, the higher the rate of edge diffusion, the grater the branch thickness.)
- Island growth in the presence of other islands (the islands compete for the available diffusing monomeres.)

Depending on the growth conditions, e.g. substrate temperature, growth rate, one gets compact or ramified islands. DLA growth predicts compact islands at high temperatures and ramified islands at low temperatures. The characteristic parameter for describing the island shapes is the fractal dimension. Values higher than 1.6 imply another growth mechanism, which is different from that in the DLA model [12].

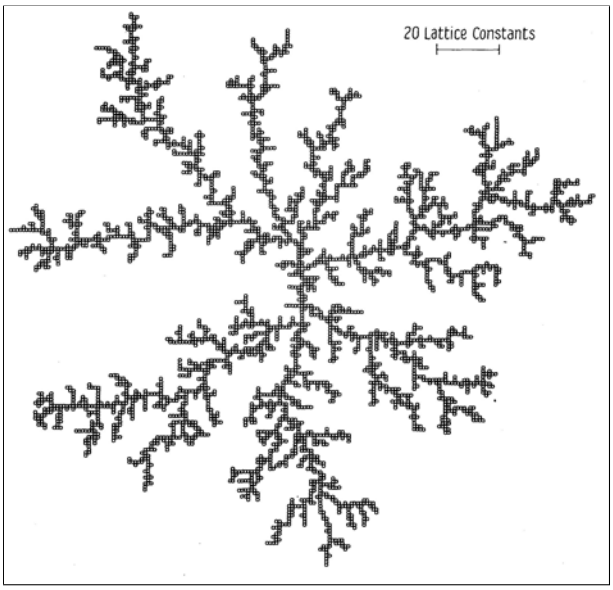

Figure 2.5.: **Classical DLA growth.** Computer model from an island with 3600 particles. A 'hit and stick process' gives a fractal with a Hausdorff dimension of about 1.6 [9].

2.4. Critical cluster size for nucleation

On the substrate, impinging molecules are diffusing on the surface as long as they do not encounter some other molecules. Not till then, the molecules start to form stable nuclei.
One less than the number of molecules which are necessary to form a stable nucleus, is called the critical cluster size for nucleation, as illustrated in fig.2.6. Note that for 6P the particles are not point like. The nucleation can be described by the diffusion mediated growth, which involves four different steps [13]:

- **1st step**
  Initially, monomers diffuse on an almost bare substrate, and when a critical number of them meet, a stable nucleus is formed.
- **2nd step**
  In a second (intermediate) step, adsorbents still nucleate new islands but also start aggregating into existing ones.
- **3rd step**
  Then, in the aggregation regime, the incoming material only aggregates into existing islands.
- **4th step**
  Finally, islands are growing together.

The island density increases until the 3rd step is reached, in this so called aggregation regime (saturated island density) different methods, as described in the following chapters (different growth rates, scaling theory and Voronoi analysis), were used to determine the critical nucleation size.

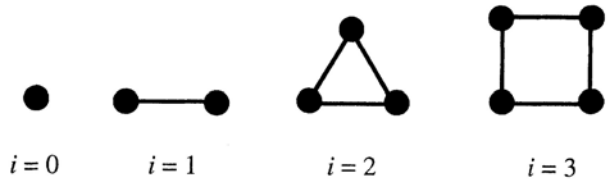

Figure 2.6.: **Stable island configurations** for different critical island sizes from $i = 0$ (freezing of monomeres) to 3 [14].

2.4.1. Different growth rates

The island density n_x (n_0 is the available adsorption sites) can be changed experimentally by variation of the deposition rate r and substrate temperature T in the following form [7]:

$$\frac{n_x}{n_0} = \eta(\Theta, i)\left(\frac{4 \cdot r}{\nu_0 \cdot n_0}\right)^{\kappa} \cdot exp\left(\frac{i \cdot E_{diff} + E_i}{(i+2)R \cdot T}\right) \tag{2.1}$$

This equation is valid in case of complete condensation, i.e. when desorption of the monomers can be ignored. η is a weak function of Θ ($\approx 0.1 - 1$). ν_0 is the hopping frequency for diffusion, E_{diff} the diffusion energy of adatoms and E_i the binding energy of the critical cluster. In the exponent $\kappa = i/(i+2)$, i means the critical cluster size for nucleation. To determine the critical cluster size, one has to plot $ln(n_x)$ vs. r, the slope B of a linear fit is therefore:

$$B = \kappa = \frac{i}{i+2} \tag{2.2}$$

As a result one gets for the critical nucleation size:

$$i = \frac{2}{\frac{1}{B} - 1} \tag{2.3}$$

A drawback of this method is that one must produce a couple of samples for only one result at a fixed temperature.

2.4.2. Scaling theory

Another way to obtain the critical cluster size is given by the so called scaling theory, where the distribution of the island areas is used [13], [14], [15], [16]. The distribution of islands of size a per unit area (denoted as N_a in μm^{-4}) can be measured by AFM

and can be ploted for different coverages Θ. Each graph has a well defined maximum at A (mean value of a), which increases with increasing coverage and the distribution broadens. After rescaling acc. to:

$$N_a(\Theta) = \Theta A(\Theta)^{-2} f(u) \tag{2.4}$$

the different distributions collaps into only one empirical scaling function $f(u)$. An analytical expression for the scaled island size distribution is given in the following term:

$$f(u) = C_i u^i exp(-b_i i u^{1/b_i}) \tag{2.5}$$

with $u = a/A$. The numerical values of the parameters are fixed by the implicit hypergeometrical equations:

$$\frac{\Gamma[(i+2)b_i]}{\Gamma[(i+1)b_i]} = (ib_i)^{b_i} \tag{2.6}$$

and

$$C_i = \frac{(ib_i)^{(i+1)b_i}}{b_i \Gamma[(i+1)b_i]} \tag{2.7}$$

An illustration of the scaling function (equ.2.5) is given in fig.2.7 where one can compare the different critical nucleation sizes from $i = 1$ to 6. The best fit of the measured size distribution to equ.2.5 for differnt i gives the critical island size.

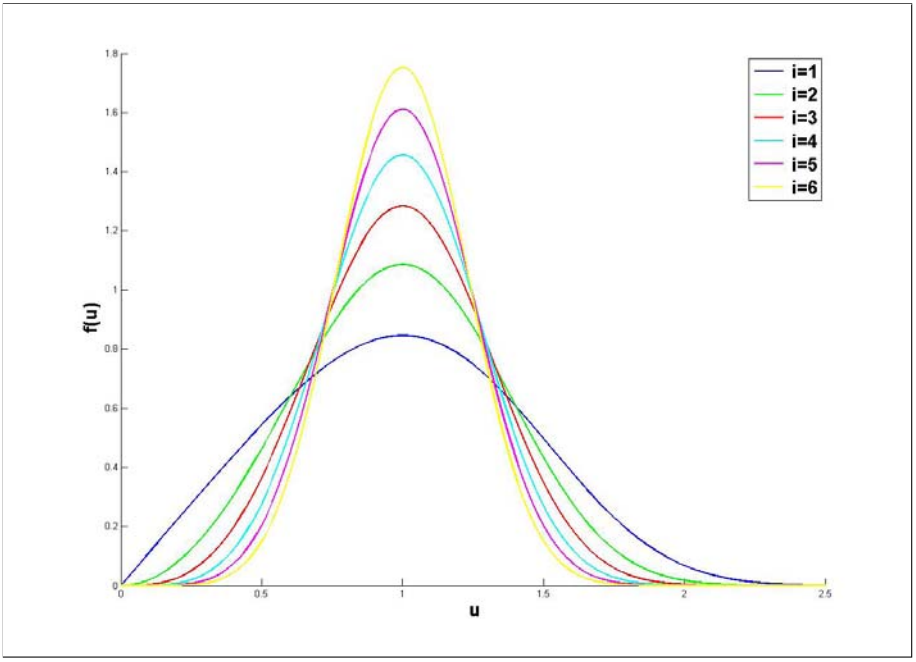

Figure 2.7.: **Scaling function** with different critical nucleation sizes from $i = 1$ to 6 acc. to $f(u) = C_i u^i exp(-b_i i u^{1/b_i})$, $u = a/A$ (a: island size, A: mean value of a).

2.4.3. Voronoi analysis

Another evaluation methode is based on the so called Voronoi tesselation, where the critical island size can be derived from the islands capture zone distribution [17]. This

zones can roughly be described by Voronoi polygons as illustrated in fig.2.8.

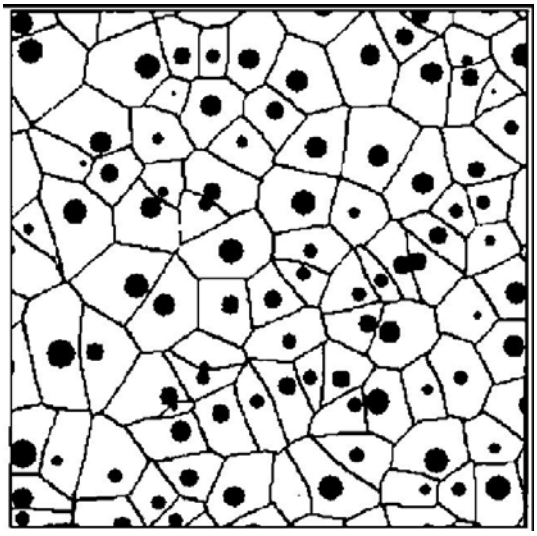

Figure 2.8.: **Voronoi tesselation**. The boundaries of a Voronoi polygon of an island (black circles) are in the half distance beetween the nearest neighbour islands [17].

The size distribution P of the capture zones can be descibed by the generalized Wigner surmise:

$$P_\beta(s) = a_\beta s^\beta exp(-b_\beta s^2) \tag{2.8}$$

with $s = v/V$ (v: Voronoi polygon size, V: mean value of v) and the parameter β:

$$\beta = \frac{2}{d}(i+1) \tag{2.9}$$

where d is the dimension. For condensation in 2 dimensions, $d = 2$ and hence $\beta = i + 1$. The two constants a_β and b_β are given by:

$$a_\beta = 2\Gamma\Big(\frac{\beta+2}{2}\Big)^{\beta+1}/\Gamma\Big(\frac{\beta+1}{2}\Big)^{\beta+2} \tag{2.10}$$

$$b_\beta = \Big[\Gamma\Big(\frac{\beta+2}{2}\Big)/\Gamma\Big(\frac{\beta+1}{2}\Big)\Big]^2 \tag{2.11}$$

As like as in the scaling theory, the best fit of the measured size distribution with equ.2.8 for differnt i gives the critical island size.

2.5. Analytical methods

2.5.1. Auger electron spectroscopy (AES)

Auger electron spectroscopy (AES, after Pierre Auger) is a common analytical technique to measure the chemical composition of a surface. This method is based on the Auger effect, where an impinging electron (2-10 keV) from an electron gun ionizes an atom in the material, which is to be examined. The so created hole in one of the inner shells (core hole) is filled either by

- an electron from an energetically higher level, where the energy is released by emitting a characteristic X-ray photon or
- an outer electron, where the energy is transmitted in a radiationless process (Auger effect) to another electron.

This so called Auger electron leaves the atom with a characteristic kinetic energy and can be classified by the involved energy levels. For instance a KL_1L_2 Auger electron means that the atom is primarily ionized in the K shell, this hole is filled by an electron of the L_1 shell and the emitted electron comes from the L_2 shell. Therefore three electrons are involved in the Auger process, hence H and He do not produce Auger electrons. The kinetic energy of course depends on the involved energy levels and can be approximated as follows:

$$E_{KL_1L_2} = E_K - E_{L_1} - E_{L_2} - \Phi - \Delta E_r \tag{2.12}$$

Where Φ is the necessary energy to bring an electron from the Fermi level to the vacuum level (work function). Furthermore, one must take into account that the energy levels of the ionized atom shift in comparison to the neutral atom, expressed with the relaxation energy ΔE_r.
The Auger spectra for all elements are recorded in a so called Auger atlas [18]. Further information can be found in the corresponding literature [19].

2.5.2. Atomic force microscopy (AFM)

The atomic force microscope is part of the family of scanning probe microscopes [7]. The first scanning probe microscope, the scanning tunneling microscope (STM, 1981) is restricted to electrically conducting surfaces [7]. With the AFM it became possible to get a three dimensional picture of surfaces also of insulating materials. However very rough samples can not be investigated.
The surface is scanned by a small sharp tip, which is mounted on a cantilever. The distance between the tip and the sample surface is so small that atomic-range forces act between them. This force can be determined by detecting the deflection of the cantilever by several methods:

- An STM measures the cantilever deflection
- Laser beam with a position sensitve photo detector
- Optical interferometry
- Capacitance change between cantilever and an additional electrode

- Electrically by a cantilever fabricated from piezoresistive material

The cantilever is typically $150 - 250\ \mu m$ long, normal tips are $7 - 15\ \mu m$ high and have an end radius of $5 - 10\ nm$ (fig. 2.9). The tip is moved over the sample (or the sample under the tip) by a piezoelectric scanner. The image size is therefore small compared to SEM (max. $100x100\ \mu m$).

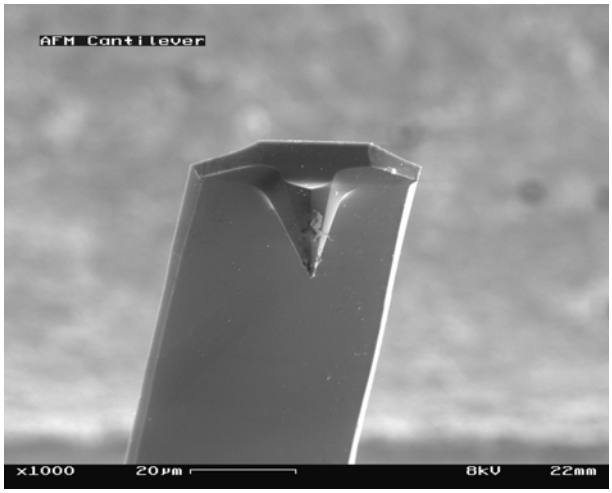

Figure 2.9.: **Cantilever with tip** in atomic force microscope (magnification $1000x$) [20].

The AFM can be used in different modes. The distance from tip to sample used for AFM imaging defines the mode of operation (fig.2.10):

- Contact mode
- Non-contact mode
- Intermittent-contact mode

AFM contact mode
The tip to sample distance is only a few Ångstrom (soft contact). The tip is affected by a repulsive force as shown in fig.2.10 (Lennard Jones potential). For this mode one uses a cantilever with a low spring constant to avoid damaging of the probed surface. The tip-sample interaction causes the cantilever to bend following the change in surface topography.
Concerning the use of a feedback control one can distinguish between the constant-height mode and the constant-force mode. To create an image in the constant-height mode, the scanner height is fixed and the cantilever deflection is monitored (fast scan speed). In constant-force mode, the cantilever deflection is fixed and the scanner height is monitored (limited scan speed).

AFM non-contact mode
The tip to sample distance is $1 - 10\ nm$ (little or no contact). The tip is affected by a weak attractive force. For this mode stiffer cantilevers are necessary. The cantilever is in vibration near its resonant frequency ($100 - 400\ kHz$), with a typical amplitude of a few tens of $\AA$. The cantilever resonance frequency changes according the interaction with

the surface. The non-contact mode is advantageous for studying soft or elastic samples.

AFM intermittent-contact mode
The tip is closer to the sample and vibrates with a greater amplitude than that in the non-contact mode. This mode is also called 'tapping-mode', because the cantilever tip barely touches (taps) the surface. This mode is advantageous for surfaces with high topographical corrugation.

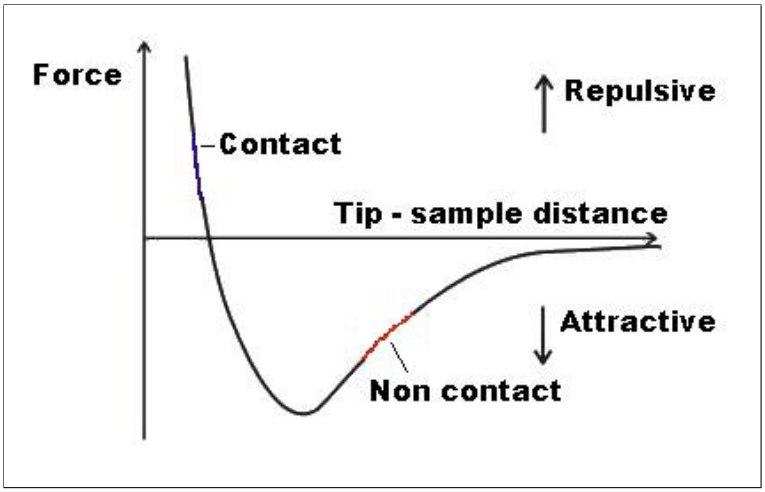

Figure 2.10.: **Force on the AFM tip versus distance from the sample surface (Lennard Jones potential).** In contact mode the distance of the tip from the sample is only a few $\mathring{A}$ (repulsive force). In non-contact mode the distance is $1 - 10\ nm$ (weak attractive force).

2.5.3. Transverse shear microscopy (TSM)

The 6P molecules stands not exactly perpendicular to the surface, each island has its own tilt direction, as sketched in fig.2.11. This can be measured by TSM which is a special mode of conventional lateral force microscopy (LFM) [21].

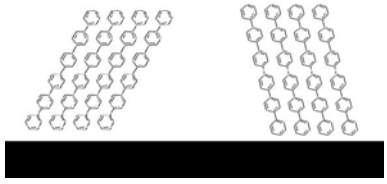

Figure 2.11.: **6P Islands** with different molecule orientations.

The cantilever is scanned parallel to its long axis in contact mode (see fig.2.12). The normal deflection is used as topographic signal and the lateral torsion of the cantilever is used to measure the crystallographic orientation. In trace and retrace scan directions, morphology induced signals are the same, while signals induced by crystallography are opposite. To correct the topographical effects, the final image is created by a subtraction $((trace\ signal - retrace\ signal)/2)$ [22].

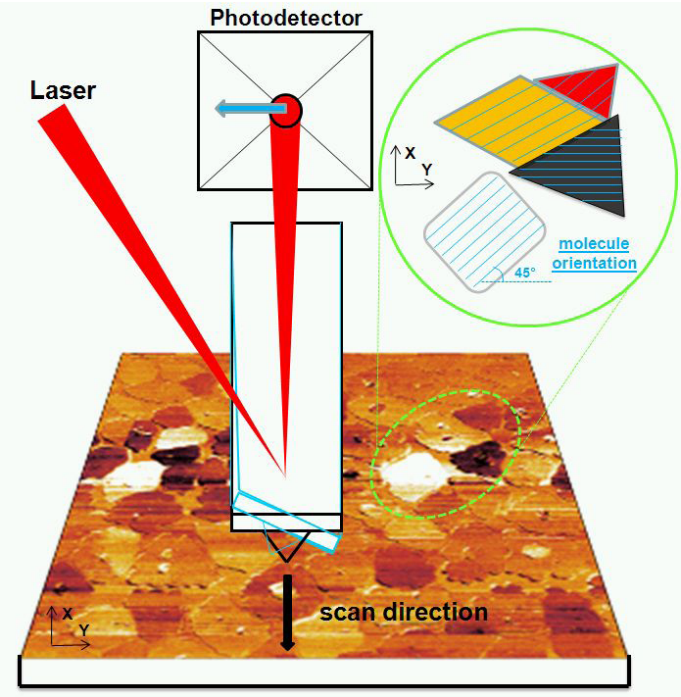

Figure 2.12.: **TSM principle.** The cantilever is scanned parallel to its long axis in contact mode and can be deflected in normal and lateral direction, depending on the molecular orientation (different contrast) as sketched in the inset. Picture: Quan Shen, privat communication.

2.5.4. Thermal desorption spectroscopy (TDS)

To obtain thermal desorption spectra, a sample with previously adsorbed particles is heated with a temperature program in UHV. In the temperature program the heating rate β, the start and end temperature can be chosen. The now desorbing particles can be detected by a mass spectrometer. This partial pressure versus temperature or time provides informations for the determination of kinetic and thermodynamic parameters of desorption processes, such as:

- Desorption order from the peak shape
- Desorption energy from the peak temperature
- Number of desorption states from the number of desorption peaks
- Coverage from the peak area

A general relation between desorption rate r and temperature T is given by the Polanyi-Wigner equation [7].

$$r = -\frac{d\Theta}{dt} = \nu_n \Theta^n exp\Big(-\frac{E_{Des}}{R \cdot T}\Big) \tag{2.13}$$

Here, ν_n is the frequency factor, n the desorption order, Θ the coverage, E_{Des} the desorption energy and R the gas constant with approximately 2 $\frac{cal}{K \cdot mol}$.

Coverage

The coverage is defined as

$$\Theta = \frac{N_{ad}}{N_{ad}^{max}} \tag{2.14}$$

Where N_{ad} is the number of adsorbed particles and N_{ad}^{max} the maximum number of adsorbable particles.

Frequency factor

ν_n is the frequency factor, one can interpret ν_1 as frequency of attempts of the adsorbed particle to desorb. For small molecules a frequency factor of 10^{13} Hz is commonly assumed.

Desorption order

Desorption of zero order ($n = 0$)

In this case the desorption rate is independent from the coverage. The zero order desorption occurs in the multilayer regime and has the following characteristics:

- Exponential increase of r vs. temperature
- Steep decrease of r, if the adsorbate is no longer available
- The maximum of desorption shifts to higher temperature with increasing coverage

Desorption of first order ($n = 1$)

The first order desorption occurs if single particles desorb directly and has the following characteristics:

- Asymmetric spectrum with steeper decrease at higher temperature
- The temperature of the desorption rate maximum is independent of coverage
- The temperature of the desorption rate maximum is dependent of the heating rate

Desorption of second order ($n = 2$)

The second order desorption occurs if two atoms recombine during desorption and has the following characteristics:

- Symmetric peak
- Peak maximum shifts with increasing initial coverage to lower temperatures

Desorption energy

Determination of the desorption energy for zero order desorption

One can obtain the desorption energy from a simple analysis [23]. A plot $ln(r)$ vs. $1/T$ of the TD spectra gives with the logarithmic Polanyi-Wigner equation 2.13 for zero order desorption ($n = 0$):

$$ln(r) = ln(\nu_0) + ln(\Theta_{max}) - \frac{E_{Des}}{R} \cdot \frac{1}{T} \tag{2.15}$$

the desorption energy from the slope of this plot. The frequency factor ν_0 can be determined from the intercept.

Determination of the desorption energy for first order desorption

The desorption energy can be determined by the so called heating rate variation method, which is based on the collection of a series of spectra with the same coverage but different heating rates β. From each spectrum, the temperature of the desorption rate maximum T_m is determined. The derivation starts with the substitution of the time t in the Polanyi-Wigner equ.2.13 by the temperature T, with $dt = (1/\beta) \cdot dT$

$$\frac{d\Theta}{dT} = -\frac{1}{\beta}\nu_1 \cdot \Theta \cdot exp\Big(-\frac{E_{Des}}{R \cdot T}\Big) \tag{2.16}$$

For the maximum of the desorption rate at $T = T_m$, the condition:

$$0 = \frac{dr}{dT} = \frac{d^2\Theta}{dT^2} \tag{2.17}$$

must be fulfilled:

$$\frac{d^2\Theta}{dT^2} = \frac{d\Theta}{dT} + \Theta \cdot \frac{E_{Des}}{R \cdot T_m^2} \tag{2.18}$$

Inserting equ.2.16 provides:

$$\frac{E_{Des}}{R \cdot T_m^2} = \frac{\nu_1}{\beta} \cdot exp\Big(-\frac{E_{Des}}{R \cdot T_m}\Big) \tag{2.19}$$

The logarithm of this equation yields:

$$ln\Big(\frac{T_m^2}{\beta}\Big) = \frac{E_{Des}}{R \cdot T_m} + ln\Big(\frac{E_{Des}}{\nu_1 \cdot R}\Big) \tag{2.20}$$

The plot $ln(T_m^2/\beta)$ vs. $1/T_m$ gives the desorption energy from the slope and the frequency factor from the intercept.

Another methode to approximate the desorption energy E_{Des} for $n = 1$ is given by the Redhead equation [7]:

$$E_{Des} = R \cdot T_m \cdot \Big[ln\Big(\frac{\nu_1 T_m}{\beta}\Big) - ln\Big(\frac{E_{Des}}{RT_m}\Big)\Big] \tag{2.21}$$

This equation follows from solving equ.2.19, where R is the gas constant and T_m the temperature of the desorption rate maximum. It can be shown that:

$$ln(E_{Des}/RT_m) \approx 3.64 \tag{2.22}$$

3. Experimental

A mica slice of 1 cm^2 with a thickness smaller than 0.05 mm was cleaved in air by adhesive tape. The cleaved mica was immediately mounted on a steel plate of the sample holder (fig.3.1(a)) by tantalum fixation wires (fig.3.1(b)). The sample holder was immediately placed into the ultra-high vacuum chamber. With the rotatable sample holder it is possible to place the sample in front of each instrument (fig.3.4), cool the sample with LN_2 and heat it. After one day the pressure reaches about 10^{-8} $mbar$. The desired temperature of the mica during the film growth was reached by resistive heating and cooling with LN_2. The temperature was measured by a Ni-NiCr thermocouple, attached to the steel plate.

(a) Sample holder (b) Mica attached to the steel plate.

Figure 3.1.: **Sample holder.** (a) With the sample holder it is possible to move the sample in x, y, z direction and rotate the sample holder within the vacuum chamber. (b) shows a magnification of the mica mounted on the steel plate of the sample holder by tantalum fixation wires, on the right one can see the Ni-NiCr thermocouple. On the rear side of the steel plate Ø 0.25 mm tantalum wires are spot welded, whereby the sample can be heated by ohmic heating.

The substrate surface was modified by 10 min Ar^+ sputtering with 600 V at a pressure of $5 \cdot 10^{-7} mbar$. For thermal desorption spectroscopy a multiplexed quadrupole mass spectrometer was used, typically the mass $m = 61$ u was measured. Auger electron spectroscopy was used to measure the chemical composition of the mica surface.
The 6P films were grown by physical vapour deposition (PVD) from a home made Knud-

sen cell (see fig.3.2), the thickness was measured by a quartz microbalance. After the film growth the heating was switched off and the temperature decreased because of LN_2 cooling (110 K), afterwards the temperature increased to room temperature within several hours, until the ready sample could be investigate with ex-situ AFM (chap.3.2).

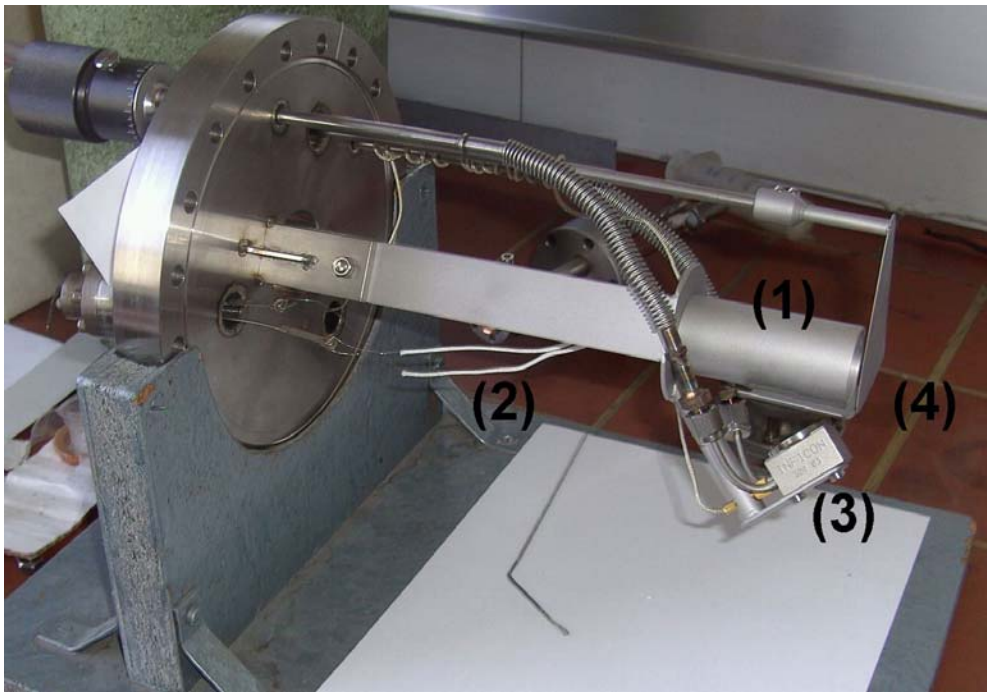

Figure 3.2.: **With the help of the Knudsen cell it is possible to bring the 6P on the substrate.** (1) Chamber with 6P powder, (2) heating wires, (3) quartz microbalance, (4) shutter, different positions enable an evaporation on the quartz microbalance or sample only, on both or none.

3.1. Ultra-high vacuum setup

In fig.3.3 one can see the ultra-high vacuum chamber with the corresponding instruments. Two rotary vane pumps (Pfeiffer DUO20 and DUO010M) and three turbo molecular pumps (Leybold Turbovac 361 and two Pfeiffer TMU521) and also a TMP (Pfeiffer TMU 071P) for the sample holder was used. The pressure was measured with a Bayard Alpert gauge (Leybold IE 514 Ionivac). The gaskets consist of copper as usual, except the one between the sample holder and the vacuum chamber, this one consists of rubber for a faster mounting and removal of the sample holder.
In fig.3.4 one can see the inside of the vacuum chamber, as seen from the port where the Knudsen cell is attached. In the middle one can see the substrate mounted on the sample holder, on the right the AES.

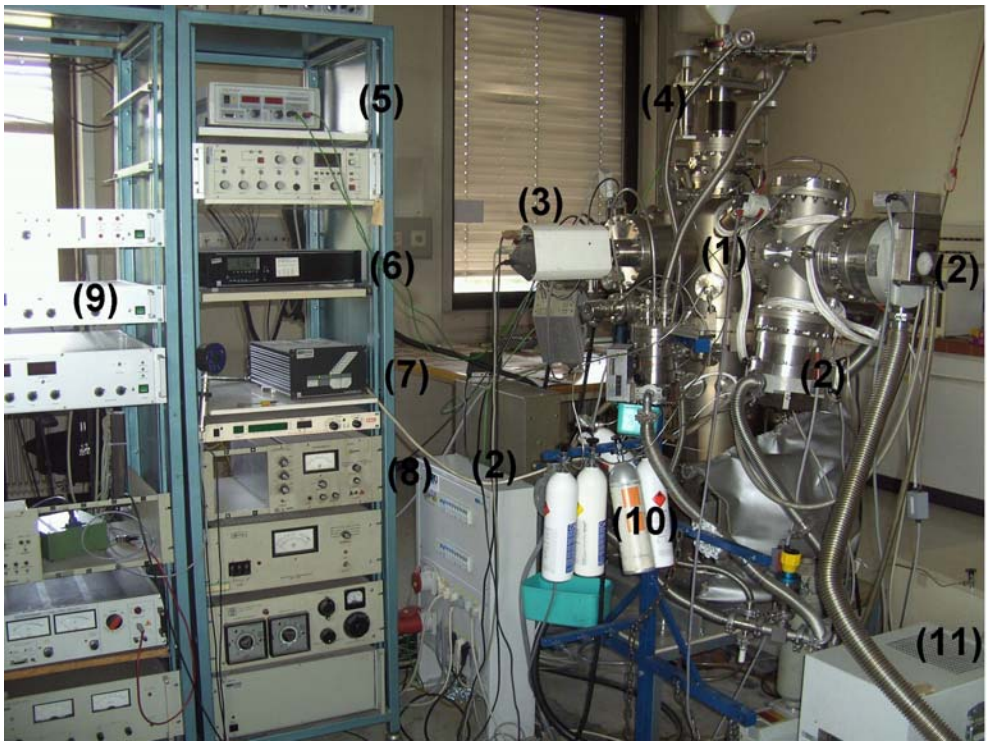

Figure 3.3.: **UHV setup.** (1) Vacuum chamber, (2) turbo molecular pump, (3) quadrupole mass spectrometer, (4) sample holder, (5) power supply for Knudsen cell heating, (6) pressure display, (7) turbo molecular pump controller, (8) sputter gun controller, (9) Auger electron spectroscopy controller, (10) argon bottle, (11) water cooling for turbo molecular pumps.

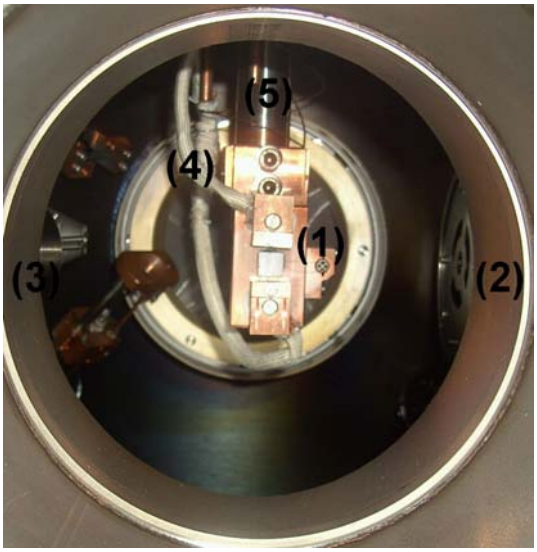

Figure 3.4.: **Vacuum chamber from inside.** (1) Mica sample on the steel plate of the sample holder, (2) Auger electron spectrometer, (3) Ar^+ sputter gun (not visible), (4) heating wires, (5) tube of the sample holder with LN_2 inside.

3.2. Atomic force microscopy

After the removal of the ready samples from the vacuum chamber the surface was investigated by atomic force microscopy (chap.2.5.2) at five different positions (fig.4.10), with the AFM from TU Graz, Institute of Solide State Physics (fig.3.5(a)) and also for a better accuracy with an AFM at the University of Leoben (fig.3.5(b)). A tutorial of the used AFM on the TU Graz is given in [24], detailed information can be found in the manuals of the manufacturer [25] and [26]. The treatment and evaluation of the AFM pictures were done by Gwyddion (chap.A.4) [27].

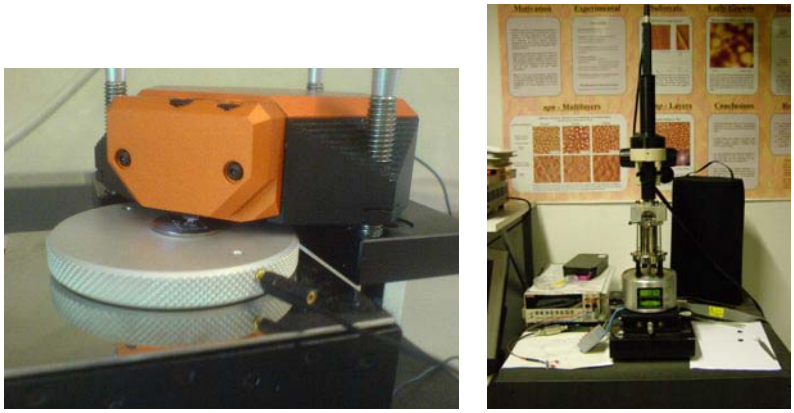

(a) AFM TU Graz (b) AFM Leoben

Figure 3.5.: **AFM** TU Graz and Leoben.

At TU Graz the ex-situ AFM Nanosurf easyScan2 was used in the dynamic force mode with a NCLR cantilever. For a better measurement the AFM is placed on a antivibration system (active vibration isolation system TS 150, fig.3.6). At the University of Leoben a Digital Instruments Nanoscope IIIa MultiMode AFM (fig.3.5(b)) was used in tapping mode under ambient conditions (standard silicon tip, spring constant $k = 40\ N/m$).

Figure 3.6.: **Vibration isolation** system TS 150.

4. Results and discussion

4.1. Sample investigation and preparation

4.1.1. Freshly installed mica

The mica was cleaved in air and directly placed into the vacuum chamber, the surface was investigated by Auger electron spectroscopy (AES), which provides information about the chemical constitution. Artefacts because of charging were barely observed, despite the fact that mica has a bad conductivity. In fig.4.2(a) the AES from a freshly installed mica, in the range from $50 - 550\ eV$ is depicted. The curve is the average value of the AES from five different positions (MW). It shows the expected elements which mica consists of (compare in addition fig.2.3) [18] :

- Al, aluminium: 68 eV; measured: 60 eV
- Si, silicon: 92 eV; measured: 75 eV
- K, potassium: 252 eV; measured: 243 eV
- O, oxygen: 510 eV; measured: 502 eV

And also

- C, carbon: 272 eV; measured: 263 eV

which is not a part of mica, it is caused by cleaving in air [28]. The difference between the measured and expected energy values is due to a chemical shift and a not exactly calibrated analyser. In fig.4.2(b), 4.2(c) and 4.2(d) only the Al/Si, K/C and O peaks at different positions and their average value curves (MW) are depicted, at all positions the peaks have almost the same height. The positions are given in fig.4.1.

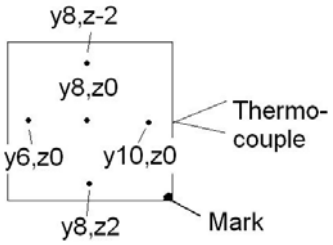

Figure 4.1.: **AES positions on the samples**, with y as abscissa and z as ordinate, the distance in y and z direction between each point is 2 mm.

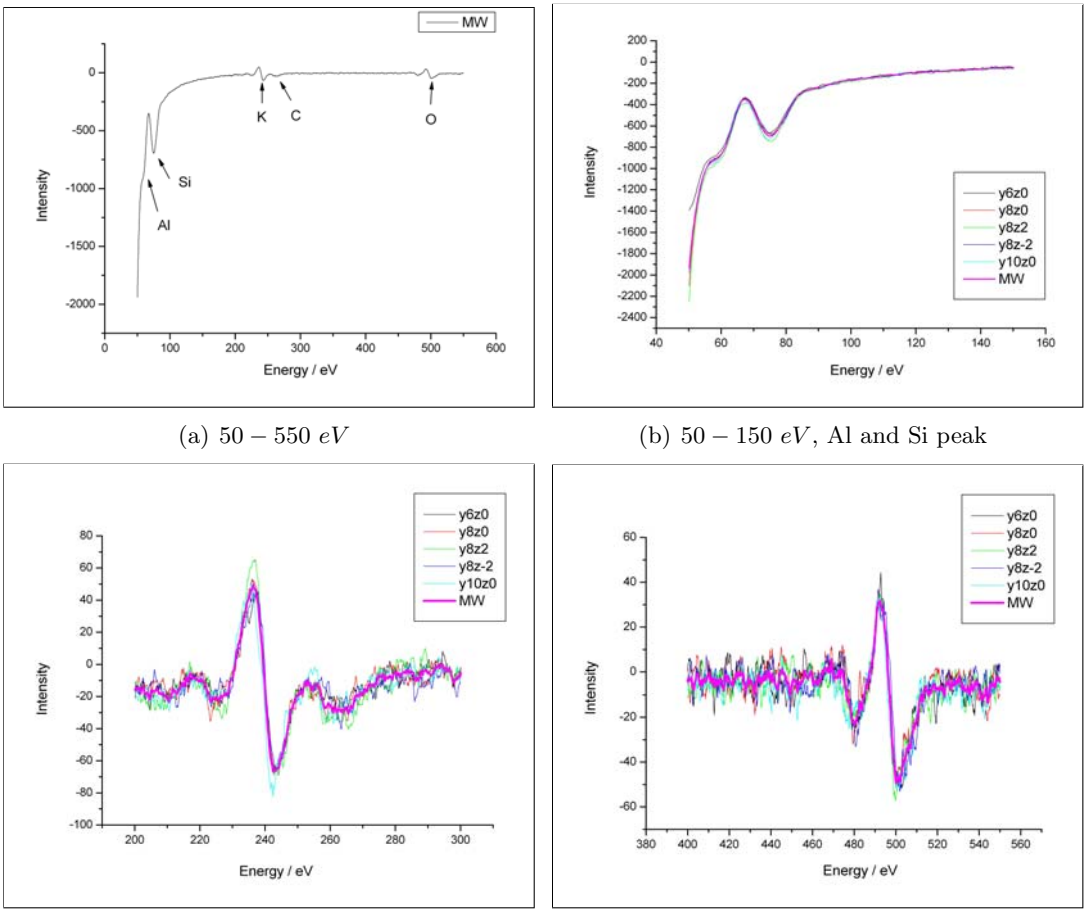

(a) $50 - 550\ eV$

(b) $50 - 150\ eV$, Al and Si peak

(c) $200 - 300\ eV$, K and C peak

(d) $400 - 550\ eV$, O peak

Figure 4.2.: **AES of a freshly installed mica**, it shows the expected elements which mica consists of: aluminium (60 eV), silicon (75 eV), potassium (243 eV) and oxygen (502 eV). Because of cleaving in air also carbon (263 eV) is visible. MW... Average value of five different positions (y6z0, y8z0, y8z2, y8z-2, y10z0) acc. to fig.4.1.

4.1.2. Preparation of the samples

The preparation of the samples for coverage (see chap.4.2.1), temperature (chap.4.2.2) and growth rate series (chap.4.2.3) was implemented as follows:

- Cleaving the mica in air
- Immediately installed in ultra-high vacuum
- Heating to 1000 K with 2 K/s
- Sputtering for 10 min, 600 V, $p = 6 \cdot 10^{-7}$ $Torr$, $T = 110$ K
- Heating to 1000 K with 2 K/s

Then the sample is ready for the 6P growth by physical vapour deposition (PVD). In the following subsections the infuence of each step will be discussed.

4.1.3. Influence of cleaving in air

To get a smooth surface, the mica sample was cleaved by an adhesive tape (fig.4.3). Fig.4.4(a) shows the AFM image from mica as received, a cross section (fig.4.4(b)) along the line '1' gives information of the roughness of the surface, structures up to 10 nm are visible, with the adhesive tape cleaving (fig.4.4(c) and 4.4(d)) one can get a much smoother surface with a roughness of about one Ångstrom (information to the treatment of the AFM images are given in chap.A.4). If the cleaved sample remains in air the carbon increases with increasing time in air [28], therefore all samples were immediately installed in ultra-high vacuum after cleaving.

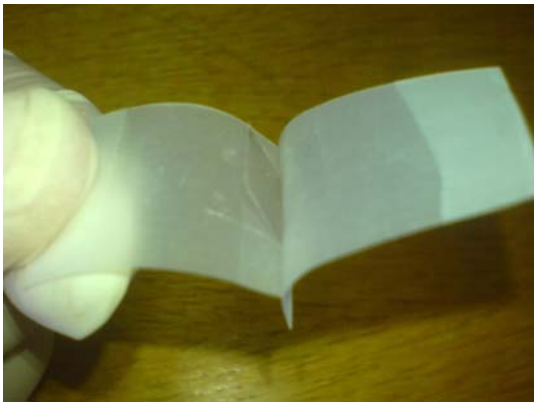

Figure 4.3.: **Cleaving the mica by an adhesive tape.** In the middle one can see the transparent cleaved mica and a mica layer on each side of the tape.

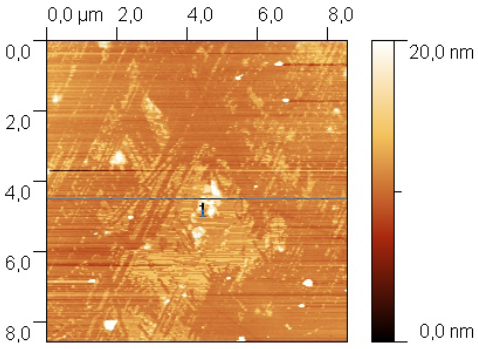

(a) AFM of the mica as received.

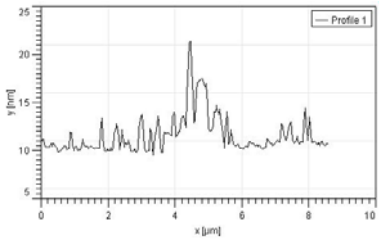

(b) Cross section from line 1 in (a), roughness: $R_q = 1.94\ nm$.

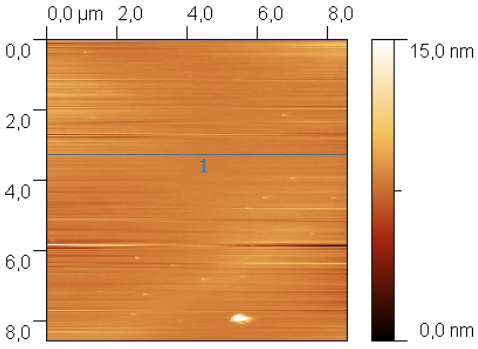

(c) AFM of the cleaved mica.

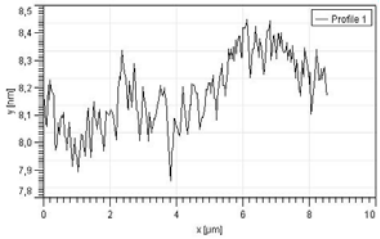

(d) Cross section from line 1 in (c), roughness: $R_q = 0.09\ nm$.

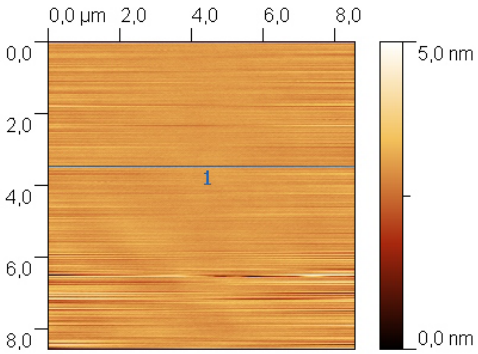

(e) AFM of the cleaved and sputtered mica.

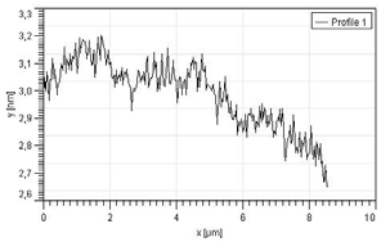

(f) Cross section from line 1 in (e), roughness: $R_q = 0.07\ nm$.

Figure 4.4.: **Surface roughness of mica** as received (a,b), cleaved by an adhesive tape (c,d) and additionally sputtered for 10 *min* (e,f). R_q... Root mean square roughness.

4.1.4. Influence of heating

To get a clean surface for the 6P growth, the samples were heated up to 1000 K. To investigate the influence of this temperature increase on the mica, the sample was repeatedly heated as follows:

- 300 K to 373 K with 1 K/s
- 300 K to 473 K with 1 K/s
- 300 K to 1000 K with 1 K/s

The corresponding Auger electron spectra (fig.4.5) show the average values of the AES from five different positions (MW) on the sample (see fig.4.1). Surprisingly the carbon (fig.4.5(b)) increases with repeated heating, however the potassium, aluminium, silicon (fig.4.5(a)) and oxygen (fig.4.5(c)) remains constant. Probably carbon contributions in the bulk segregate to the surface upon heating.

Repeated heating to hight temperature can cause blisters on the mica, as shown in fig.4.6, where the determination of the desorption energy by the 'heating rate variation methode' (see chap.4.4.1) was performed. In fig.4.6(a), one can also see the dendritic 6P islands growing over this blisters. This blisters are probably caused by water inlays in mica.

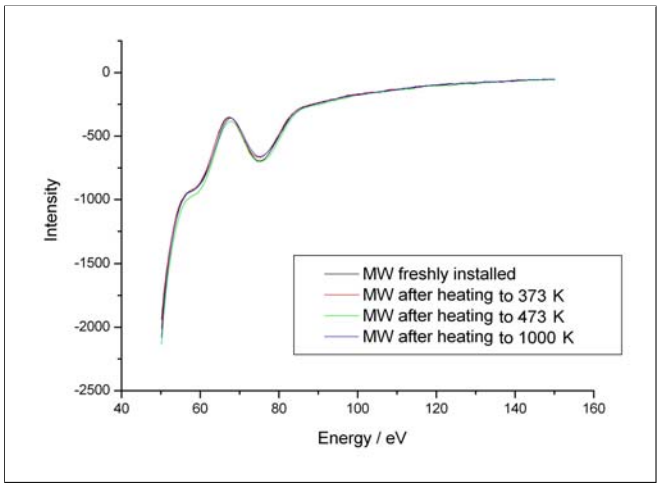

(a) $50 - 150\ eV$, Al and Si peak

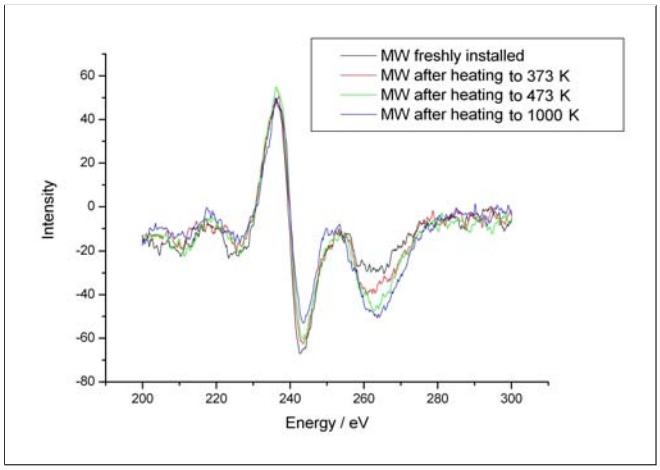

(b) $200 - 300\ eV$, K and C peak

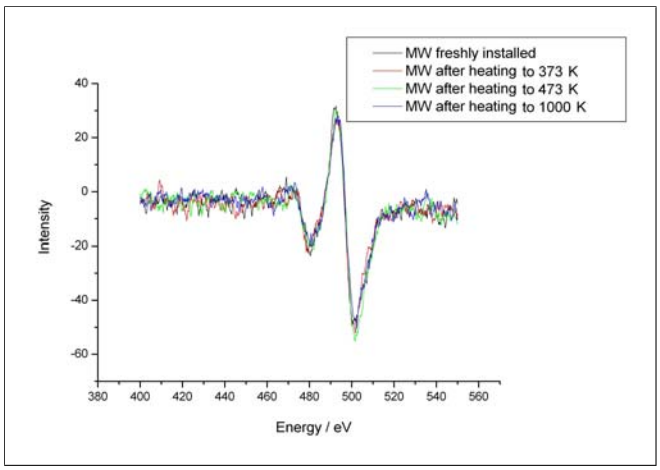

(c) $400 - 550\ eV$, O peak

Figure 4.5.: **AES from repeatedly heated mica.** (a) Aluminium ($60\ eV$) and silicon ($75\ eV$) peak remains constant after heating. (b) The carbon ($263\ eV$) increases with repeated heating. (c) The oxygen peak ($502\ eV$) remains constant after heating. MW... Average value of five different positions over the sample.

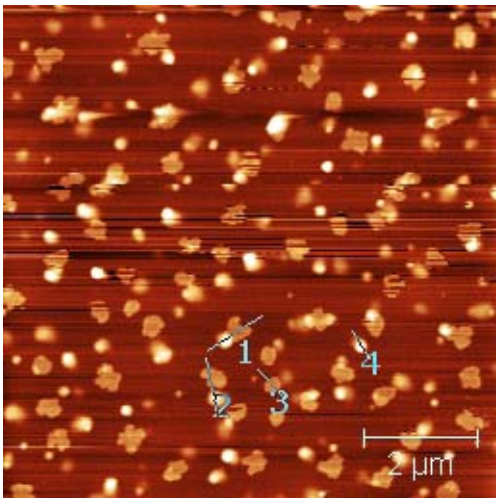

(a) AFM image of blisters and 6P islands ($T = 300\ K$, 0.08 ML, $z = 8\ nm$).

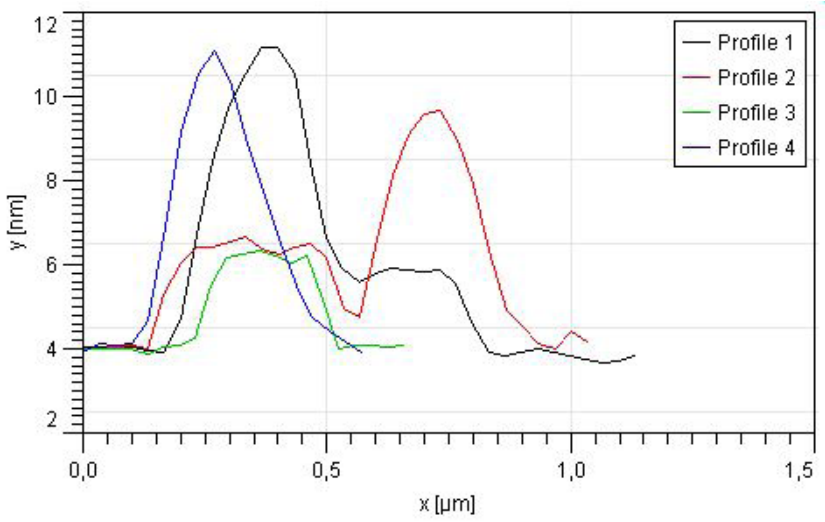

(b) Cross sections from the lines in (a).

Figure 4.6.: **AFM of mica with blisters and 6P islands.** (a) AFM image ($8.6x8.6\ \mu m$) of 6P on mica with blisters from sample 1, pos. B, caused by heating due to water inlays. (b) The cross sections from the lines in (a) show a different height of the blisters and the 6P islands.

4.1.5. Infuence of sputtering

The 6P film formation on unsputtered mica(001) has been studied by several groups [29], [30], [31], [32]. The roughness of the sputtered surface without 6P in comparison to the unsputtered surface is shown in fig.4.4(d) and 4.4(f), it is also in the range of one Ångstrom. However sputtering leads to an amorphous surface, this can considerably influence the growth of 6P [4]. In fig.4.7 one can see the TDS and AFM of 6P on mica before and after sputtering. Fig.4.7(a) is an AFM image of mica with 1.25 ML 6P which is not sputtered, one can see the well known needles, consisting of flat lying molecules. In comparison to this, we see on the sputtered mica in fig.4.7(b) islands, consisting of standing molecules.

In fig.4.7(c) a TDS of 6P on the unsputtered mica shows a mono-(wettiglayer, at about 950 K) and multilayer peak (at about 900 K) and also a peak at about 500 K caused by a faster temperature increase of the fixations wires than the mica. These stated temperatures are measured on the steel plate and describe not the real temperature of the mica. The temperature can be corrected as described in chap.A.1. On the sputtered mica (fig.4.7(d)) the monolayer peak is no longer present. Contamination with carbon also leads to an extinction of the wetting layer [4].

In fig.4.8 one can see the AES from the same sample as in fig.4.5 with an additional treatment:

- Heating from 145 K to 1000 K with 2 K/s
- Sputtering for 10 min, 600 V, $p = 6 \cdot 10^{-7}$ $Torr$, $T = 110$ K
- Heating from 135 K to 1000 K with 2 K/s
- Growth of 0.23 ML 6P

The red line in fig.4.8(b) at 263 eV shows the carbon caused by heating, one can see that the carbon decreases after sputtering to the same value as on the freshly installed mica (black line). However, the potassium (fig.4.8(b)) and oxygen (fig.4.8(c)) increases and the silicon and aluminium shifts to higher energies (fig.4.8(a)) after sputtering.

After the deposition of 0.24 ML 6P on mica, we can prove the expected increase of the carbon (fig.4.8(b), blue line), since 6P consists of carbon and also a decrease of the potassium peak may be due to carbon shielding, however oxygen remains constant.

Insufficiently sputtered mica leads to both, islands and needles (fig.4.9). In the cross sections (fig.4.9(c)) through the structures in fig.4.9(b) one can see islands with upright standing molecules with a height of 2.7 nm and on top needles, consisting of flat lying molecules.

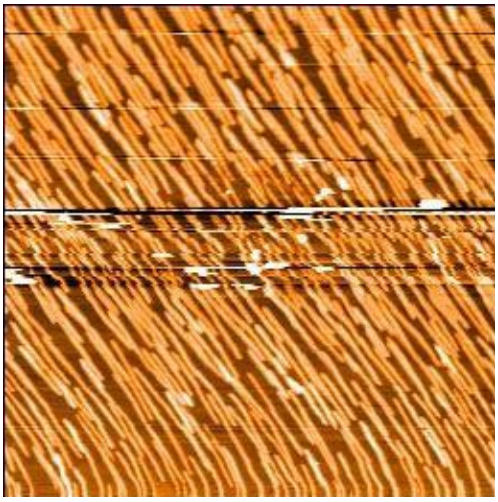

(a) AFM image ($8.6x8.6\ \mu m$) from a freshly installed mica with 1.25 ML 6P.

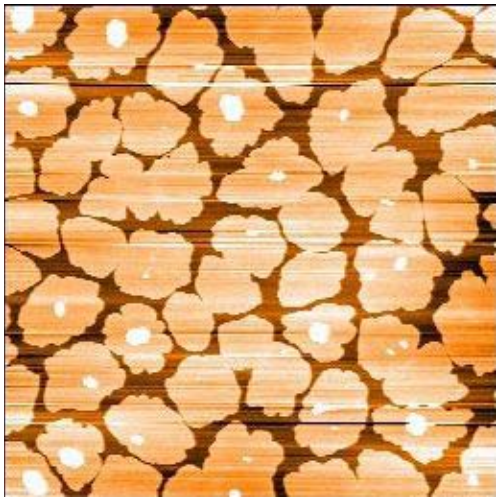

(b) AFM image ($8.6x8.6\ \mu m$) from sputtered mica with 0.87 ML 6P.

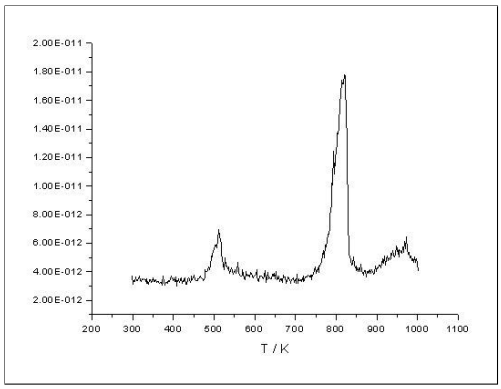

(c) TDS from 6P on freshly installed mica (0.87 ML, 2 K/s).

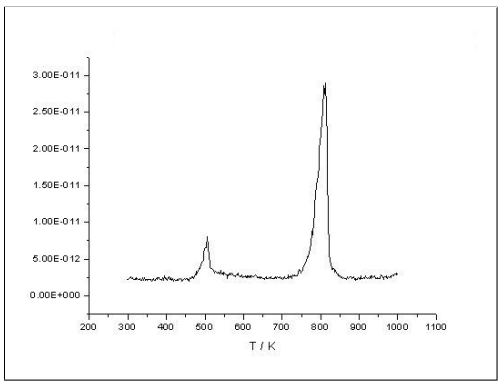

(d) TDS from 6P on sputtered mica (0.87 ML, 2 K/s).

Figure 4.7.: **Influence of sputtering.** (a) AFM image from a freshly installed mica, one sees the well known needles. (b) AFM image from sputtered mica, the 6P forms now islands. (c) TDS from 6P on freshly installed mica. The peak at about 950 K (500 K with correction acc. to chap.A.1) belongs to a wetting layer. (d) Sputtering leads to an extinction of the wetting layer.

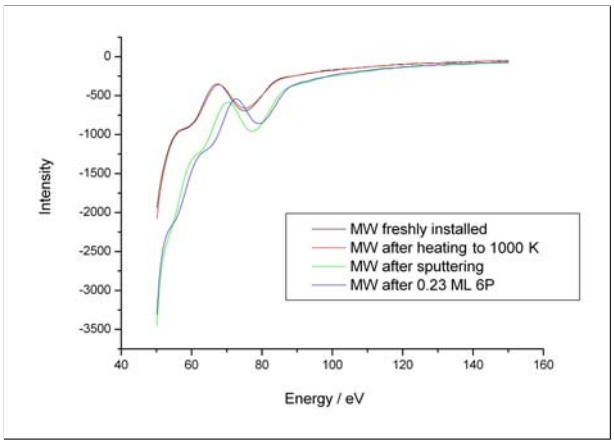

(a) $50 - 150\ eV$, Al and Si peak

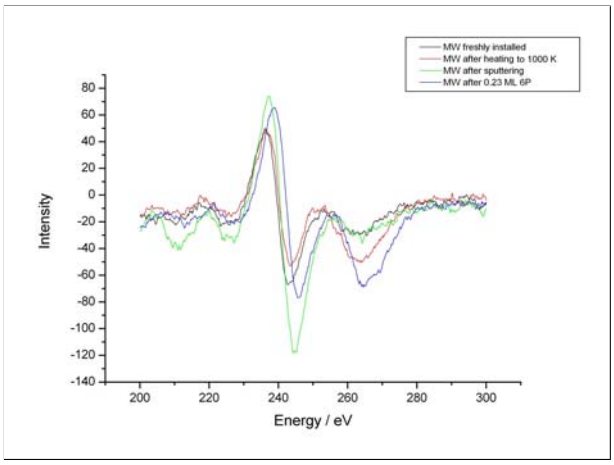

(b) $200 - 300\ eV$, K and C peak

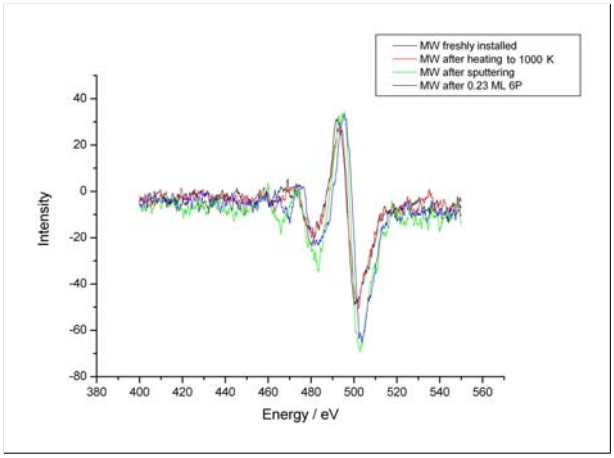

(c) $400 - 550\ eV$, O peak

Figure 4.8.: **AES from sputterd mica.** MW ... Average value of five different positions on the sample (fig.4.1). (a) The silicon and aluminium peak shifts to higher energies after sputtering. (b) The red line (heating to 1000 K) is the same as in fig.4.5, the carbon decreases after sputtering and increase after the deposition of 6P. (c) The oxygen increases after sputtering and remains constant after the deposition of 6P.

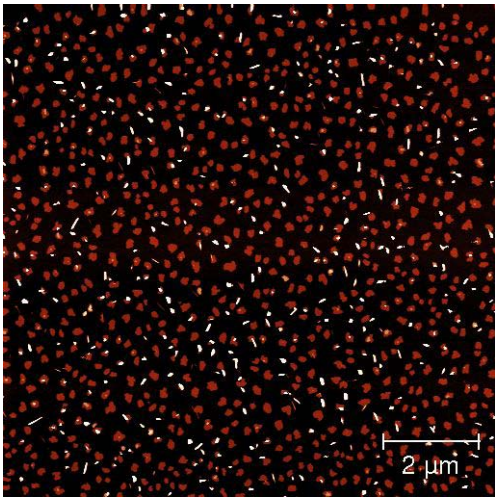

(a) AFM image ($10x10\ \mu m$) with islands and needles ($z = 10\ nm$).

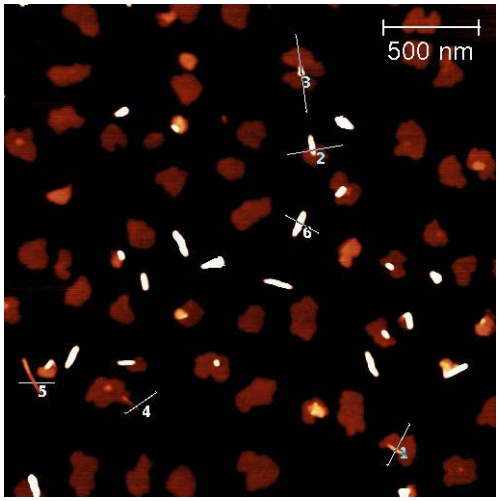

(b) AFM image ($2.5x2.5\ \mu m$), magnification of (a).

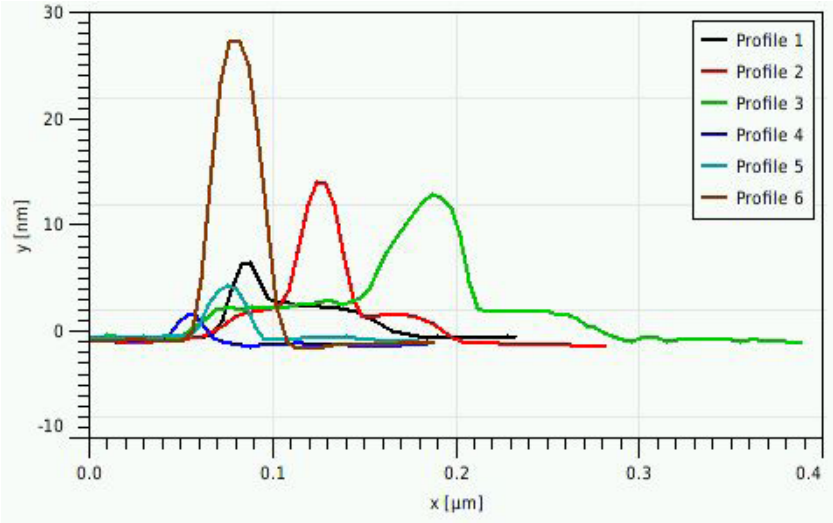

(c) Cross sections along the lines in (b).

Figure 4.9.: **AFM of 6P on insufficiently sputtered mica**. (a) AFM image of 0.22 ML 6P on insufficiently sputtered mica ($T = 300\ K$). In (b) one can see a magnification of the islands and needles from (a). In (c) the cross sections along the lines in (b) shows islands with standing molecules and on top needles, consisting of flat lying molecules.

4.2. Growth behaviour of 6P on sputtered mica(001)

In this chapter the island shapes, densities, heights and molecule orientation of para-hexaphenyl (6P) on sputtered mica were investigated by AFM and TSM at samples with different coverages (chap.4.2.1), temperatures (chap.4.2.2) and growth rates (chap.4.2.3). The treatment and evaluation of the AFM pictures were done by Gwyddion (chap.A.4). These fundamental investigations were used in chap.4.3 for the determination of the critical cluster size for nucleation. Each sample was investigated by AFM at five different positions (fig.4.10), with the AFM from TU Graz and also for a better accuracy by the University of Leoben. The thickness calibration was done as described in chap.A.3. Unfortunately, the quartz microbalance was not cooled, so also in some cases a temperature shift correction was necessary, chap.A.2.

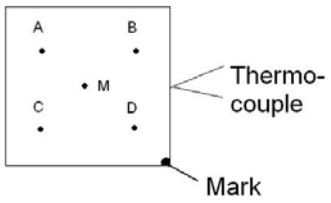

Figure 4.10.: **AFM positions** on the samples.

4.2.1. Different coverages

The first sample series describes the growth of 6P at different coverages (with nearly the same growth rate), the substrate temperature during the island growth was kept at room temperature (300 K). In fig. 4.11 AFM images with coverages from 0.08 to 1.25 monolayer (ML, chap.A.3) are depicted. A 6P monolayer is a single layer of standing molecules, with about $5.4 \cdot 10^{13}$ $molecules/cm^2$ [33].

Island shapes
At low coverages dendritic islands are visible (fig.4.11(a)), at hight coverages (fig. 4.11(d)) the islands become more compact and straight boundaries between coalescenting islands appears. With increasing coverage one can see in fig. 4.11(e) to 4.11(g) (and also in fig. 4.18) the first layer closing.

Island densities
In tab.4.1 and 4.2 the island densities at different sample positions and the corresponding average values of each sample are listed. Also fig.4.12 shows the average value of the island densities, the first point is not in the aggregation regime, the island density is not saturated (2nd step in the diffusion mediated growth, chap.2.3). The last point is lower because the islands grow together (4th step). So the fit for the middle three points gives about (1.8 ± 0.5) μm^{-2} (from $10x10$ μm AFM images, Uni Leoben) and (2.1 ± 0.5) μm^{-2} (from $8.6x8.6$ μm AFM images, TU Graz) for the island density in the aggregation regime.

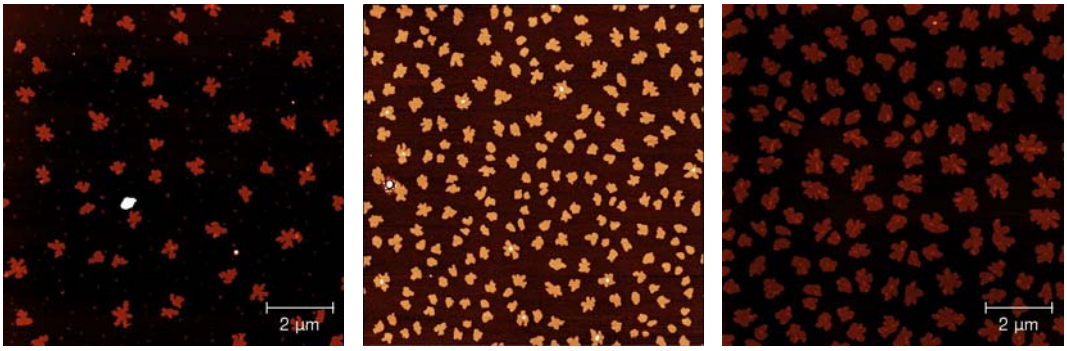

(a) 0.08 ML, r = 0.0157 ML/min, pos. M

(b) 0.21 ML, r = 0.0207 ML/min, pos. B

(c) 0.33 ML, r = 0.0340 ML/min, pos. M

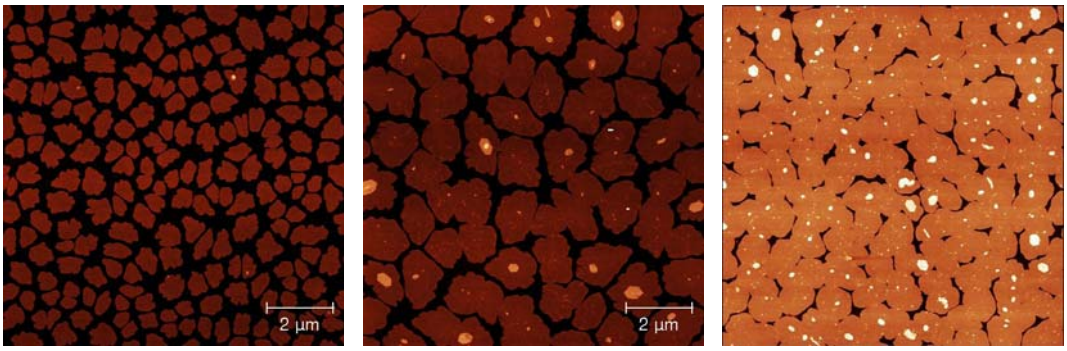

(d) 0.61 ML, r = 0.0238 ML/min, pos. M

(e) 0.87 ML, r = 0.0199 ML/min, pos. M

(f) 0.98 ML, r = 0.0175 ML/min, pos. M

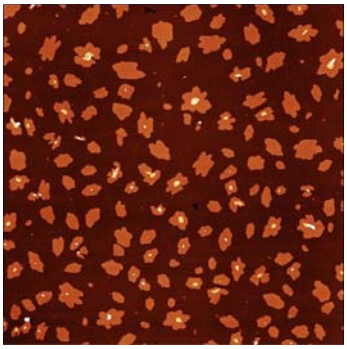

(g) 1.25 ML, r = 0.0265 ML/min, pos. C

Figure 4.11.: **AFM images ($10x10\ \mu m$) with different 6P coverages on mica** at 300 K from 0.08 to 1.25 monolayer (ML). One sees at low coverages dendritic islands (a) and with increasing coverage (b,c,d) the islands grow together (e). Then islands in the second layer start to grow (e,f,g). Pos... Position on the sample acc. to fig.4.10.

Table 4.1.: **Island densities** at different coverages (in μm^{-2}), from $10x10$ μm AFM images (Uni Leoben). Pos... Positions on the sample acc. to fig.4.10, MW... Average value. The average value in the aggregation regime (bold type) is (1.8 ± 0.5) μm^{-2}.

Coverage / ML	Pos. M	Pos. A	Pos. B	Pos. C	Pos. D	MW
0.08	0.51	1.45	0.72	1.03	0.48	0.8 ± 0.3
0.21	-	-	2.15	-	2.16	2.2 ± 0.1
0.33	1.22	1.33	1.21	1.32	1.37	1.3 ± 0.1
0.61	2.01	1.93	1.78	2.32	1.91	2.0 ± 0.3
0.87	0.60	0.58	0.75	0.76	0.71	0.7 ± 0.1

Table 4.2.: **Island densities** at different coverages (in μm^{-2}), from $8.6x8.6$ μm AFM images (TU Graz). Pos... Positions on the sample acc. to fig.4.10, MW... Average value. The average value in the aggregation regime (bold type) is (2.1 ± 0.5) μm^{-2}.

Coverage / ML	Pos. M	Pos. A	Pos. B	Pos. C	Pos. D	MW
0.08	1.41	-	1.35	1.56	-	1.4 ± 0.2
0.21	-	2.59	2.06	2.29	2.57	2.4 ± 0.4
0.33	1.50	1.51	2.18	1.69	1.69	1.7 ± 0.5
0.61	2.34	2.24	1.97	2.46	2.03	2.2 ± 0.3
0.87	0.81	0.61	0.65	0.95	0.68	0.7 ± 0.3

Island heights

In fig.4.13(a) one can see the sample with 0.87 ML, the height distribution (fig.4.13(c)) and the corresponding cross section (fig.4.13(b)). The average of the values in tab.4.3, where the island heights from different positions of each sample are listed, gives the island height of (2.3 ± 0.5) nm. This is about the length of a 6P molecule (2.7 nm), indicating that the islands are composed of standing molecules. These molecules have also a small tilt from the surface normal. The measured height also depends on the AFM normal force. With high normal force the layer is thicker as with low normal force, probably this is caused by the softness difference from mica to 6P.

Orientation of the molecules

The molecules are not standing exactly perpendicular to the surface, each island has its own tilt direction. This can be shown by transverse shear microscopy (TSM)[1], see chap.2.5.3. In fig.4.14(a) a topographic image of a 0.24 ML sample and the corresponding TSM picture (fig.4.14(b)) are shown. On the TSM image, islands with different contrast mean different crystallographic orientations. One sees a random distribution of the island molecule orientation.

[1] performed by Quan Shen, University of Leoben

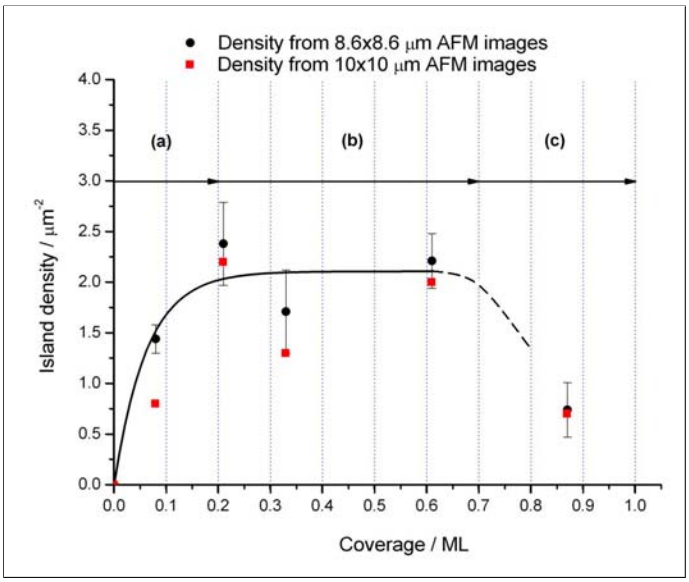

Figure 4.12.: **Island density** with increasing coverage from $8.6x8.6\ \mu m$ (and also $10x10$ μm) AFM images. (a) Low- and intermediate coverage regime, (b) in the aggregation regime, the island density is $(2.1 \pm 0.5)\ \mu m^{-2}$, (c) coalescence and percolation regime.

Table 4.3.: **Island heights** (in nm), MW... Average value, the average of this values is $(2.3 \pm 0.5)\ nm$.

Coverage / ML	Pos. M	Pos. A	Pos. B	Pos. C	Pos. D	MW
0.08	2.9	2.5	2.8	3	2.6	**2.8**
0.21	2.6	2.6	2.4	-	2.6	**2.6**
0.33	1.8	1.8	1.8	1.8	1.7	**1.8**
0.61	2.3	2.2	2.1	2.3	2.2	**2.2**
0.87	2	2.2	2	1.8	1.8	**2.0**

Second layer

It is surprising that so little material is in the second layer (see fig.4.11(e)), this means a low Ehrlich-Schwoebel barrier [34]. As described below, in fig.4.11(e) and 4.11(f) the shape of the islands in the second layer is hexagonal. In fig.4.11(g) the first layer is closed and the third layer is already visible. Hence, the second layer has a higher Ehrlich-Schwoebel barrier, in other words, less material can move to the underlying layer.
A TSM picture with material in the second layer is given in fig.4.15, with increasing coverage islands coalesce. A different molecule orientation within one island is shown in fig.4.15(b)(1).

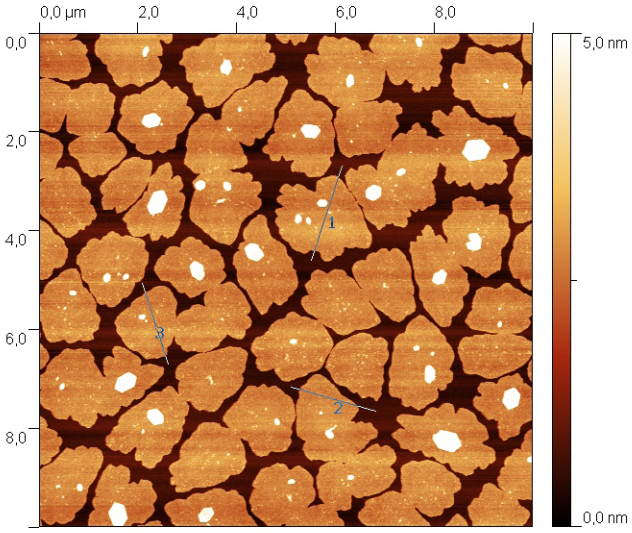

(a) AFM image of 0.87 ML 6P, pos. A.

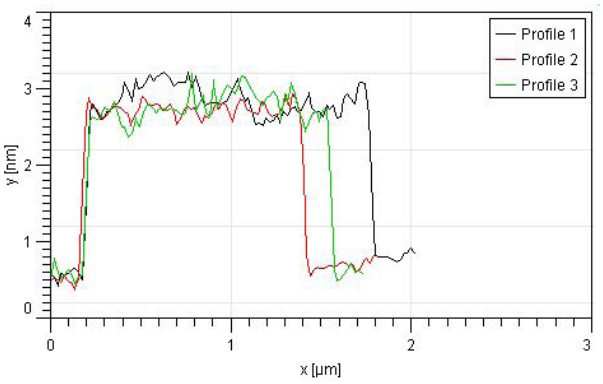

(b) The cross sections acc. to (a), give 2.2 nm for the island height.

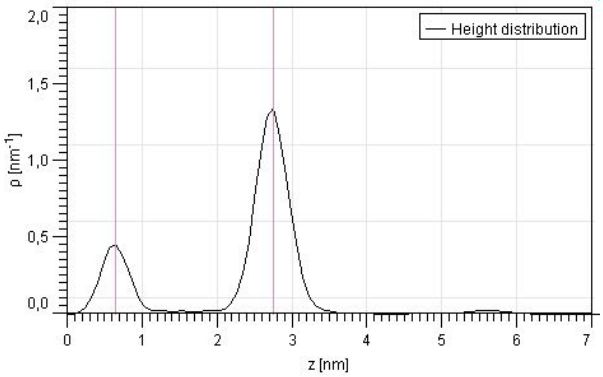

(c) Height distribution from (a), between the 2 vertical lines the heigth is 2.2 nm.

Figure 4.13.: **Islands height** of the sample with 0.87 ML 6P on sputtered mica, we see that the islands consist of standing molecules (the length of 6P is 2.7 nm).

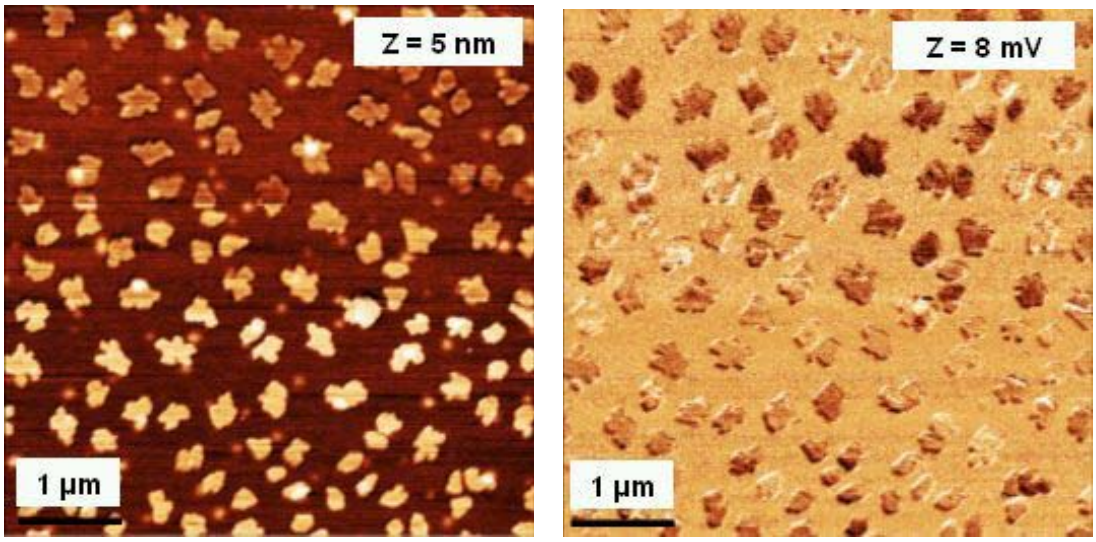

(a) AFM image of 0.24 ML 6P. (b) TSM image from topography in (a).

Figure 4.14.: **Topography and corresponding TSM image** of 0.24 ML 6P on sputtered mica, different contrast means different crystallographic orientations.

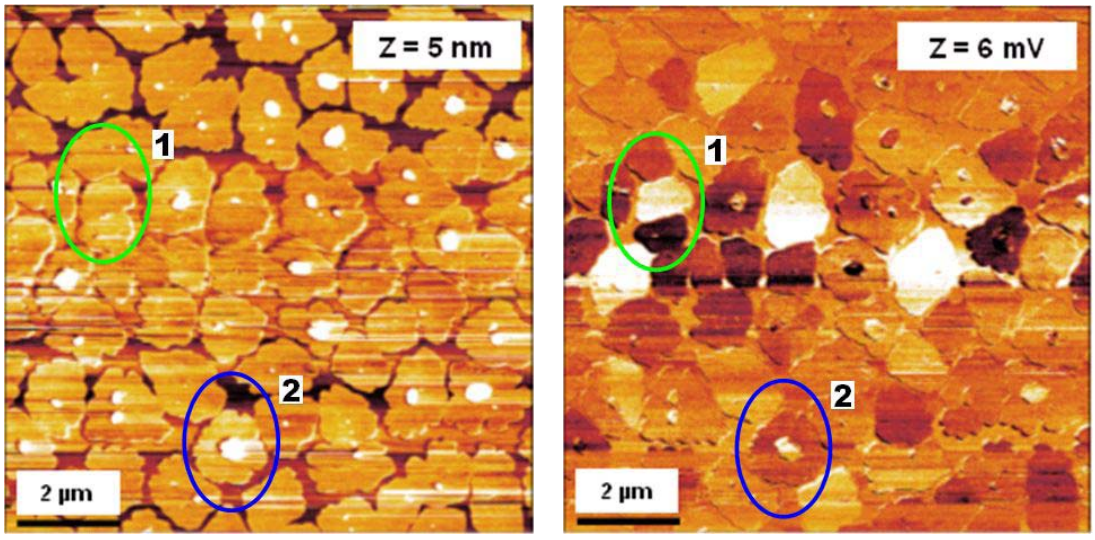

(a) AFM image of 0.87 ML 6P. (b) TSM image from topography in (a).

Figure 4.15.: **Topography and corresponding TSM image** of 0.87 ML 6P on sputtered mica with material in the second layer. (1)... One coalescented island with different molecule orientations. (2)... Hexagonal island in the second layer with another crystallographic orientation as the layer below.

Hexagonal islands in the second layer
Surprisingly, one can see that at 0.87 ML (fig.4.11(e)) hexagonal islands are appearing in the second layer. Fig.4.11 ($10x10$ μm image size) and 4.18 ($2.1x2.1$ μm image size) shows the first layer closing and the behaviour of the hexagonal islands with increasing coverage. At 0.87 ML (fig.4.11(e) and 4.18(a)), a few compact hexagons with a height of about 2.7 nm become visible, at 0.98 ML (fig.4.11(f) and 4.18(c)), the islands below become larger and the hexagons are beginning to lose their shapes. At 1.25 ML (fig.4.11(g) and 4.18(e)), the layer below is closed and the third layer is visible. The hexagons get a more dendritic shape, a possible reason for this behaviour is that the diffusion along the island rim is not large enough to reach the equilibrium shape.
TSM measurement show that these hexagonal islands often exhibit a different crystallographic orientation as the layer below (fig.4.15(b)(2)).
As mentioned in chap.2.1, the bulk of 6P has a monoclinic crystal structure, so the boundaries of the hexagon must follow certain directions in the unit cell. To find these directions, we measured the angles and compared it with the ones in this unit cell. In fig.4.16, one can see the measured angle of all corners of a hexagon from sample 5 with 0.87 ML (down on the right in fig.4.11(e)). These angles are also appearing in fig.4.17 in the specified directions. For instance, the angle with about 99° occurs between the [13] and [-1-1] direction and about 129° between the [13] and [-13] direction.

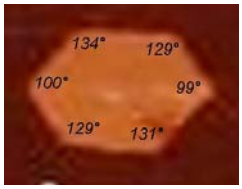

Figure 4.16.: **Angle of a hexagon** from the sample 5 with 0.87 ML (down on the right in fig.4.11(e)).

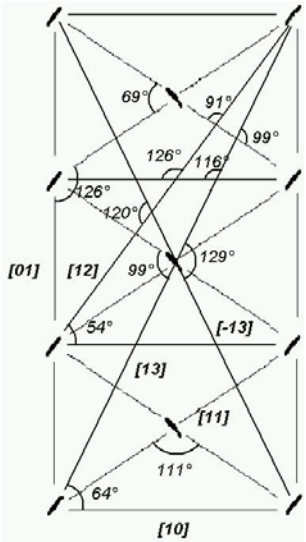

Figure 4.17.: **Angles in the ground plane of the monoclinic unit cell from 6P**. From fig.4.16 99° occur between the [13] and [-1-1] direction and 129° between the [13] and [-13] direction.

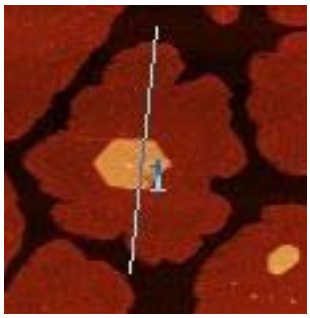

(a) 0.87 ML, $z = 10\ nm$

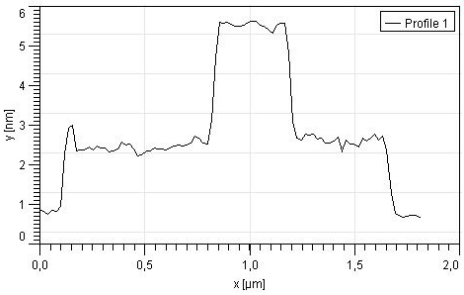

(b) Cross section of 0.87 ML.

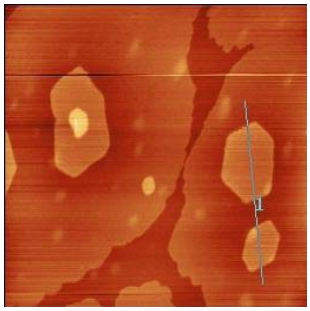

(c) 0.98 ML, $z = 15\ nm$

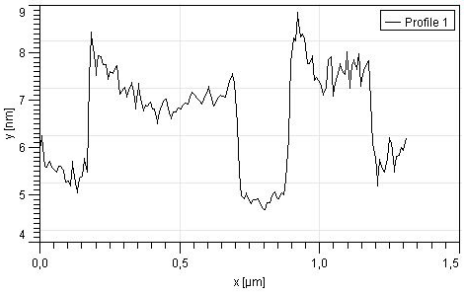

(d) Cross section of 0.98 ML.

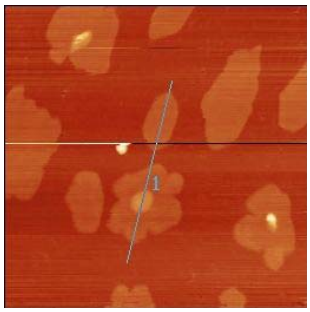

(e) 1.25 ML, $z = 30\ nm$

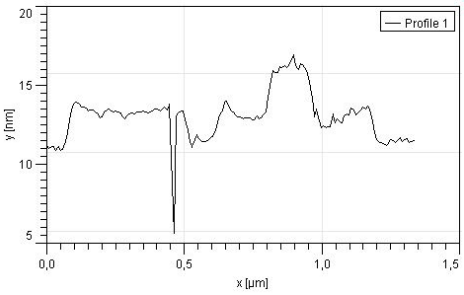

(f) Cross section of 1.25 ML.

Figure 4.18.: **First layer closing and behaviour of the hexagonal islands with increasing coverage.** A compact hexagon on top of an island is shown in (a). The cross sections (line '1' in the corresponding AFM image) gives a height of about 2.7 nm (b,d,f). At higher coverage the islands below become larger and the hexagons are beginning to lose their shapes (c). At 1.25 ML, the layer below is closed and the hexagons get a dendritic shape (e).

4.2.2. Influence of the substrate temperature

The second sample series describes the growth of 6P at different substrate temperatures during the island growth (with nearly the same growth rate of 0.02 ML/min and a constant coverage of about 0.21 ML). In fig.4.19, AFM images with substrate temperatures from 150 K to 400 K are depicted, the desorption of 6P takes place above 450 K [35].

Island shapes
As mentioned in chap.2.3, the DLA growth predicts compact islands at high temperatures and ramified islands at low temperatures, but here the shape of the islands developed from small compact islands at low temperature to dendritic and fractal like islands at higher temperature. A possible explanation is given in [12], where another growth mechanism forms the stable compact islands by the dissociation and reorganization of a metastable disorder film. This film results from immediately frozen molecuels after impinging on the substrate surface at low temperature.
On the samples at 350 K (fig.4.19(d)) and 400 K (fig.4.19(e)), smaller islands with the same heigth are appearing besides the big islands (bimodal island size distribution). In the vicinity of the big islands, the small ones are not present (denuded zones).

Island densities
In tab.4.4 and 4.5, the island densities at different substrate temperatures from different sample positions and corresponding average values are listed as obtained with two different AFMs. As mentioned in chap.2.4.1, the island density decreases with increasing temperature, acc. to equ.2.1.

The measured values from tab.4.5 are plotted in fig.4.20, one can see a nearly exponential decrease. However, a closer look in form of a logarithmic plot from the island density vs. $1/T$, as given in fig.4.21, show at higher temperatures ($>$ 300 K) a bend in the plot. Since the slope of this curves corresponds to:

$$\frac{i \cdot E_{diff} + E_i}{(i+2) \cdot R}$$

one has to assume that the change of the slope indicates a change of the critical island size i at the higher temperature (chap.4.3).

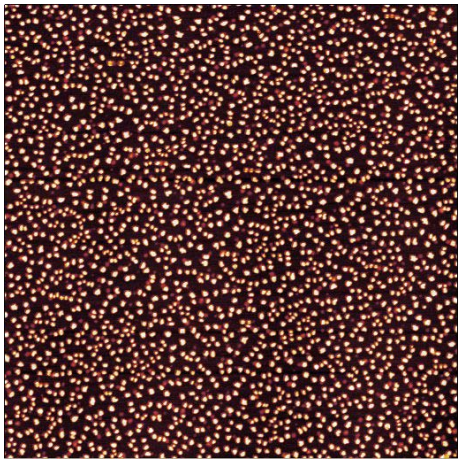

(a) $T = 150\ K$, $0.22\ ML$, $r = 0.0252\ ML/min$, pos. M

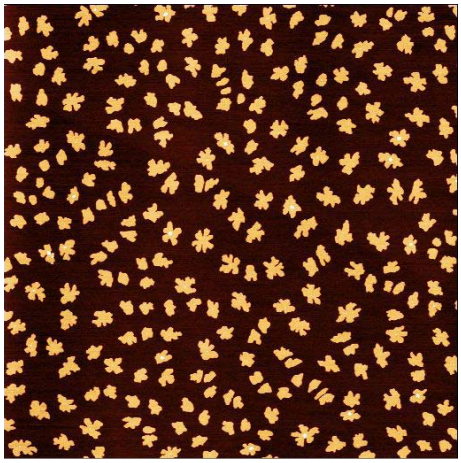

(b) $T = 250\ K$, $0.21\ ML$, $r = 0.0231\ ML/min$, pos. M

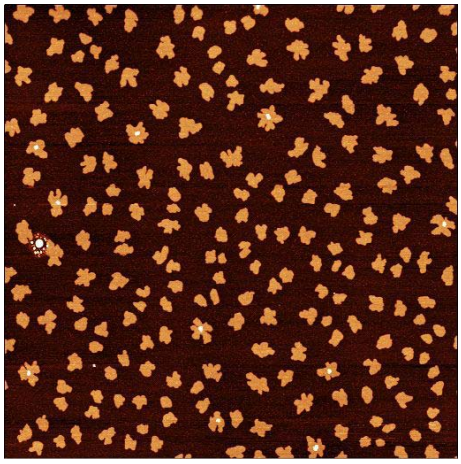

(c) $T = 300\ K$, $0.21\ ML$, $r = 0.0207\ ML/min$, pos. B

(d) $T = 350\ K$, $0.20\ ML$, $r = 0.0189\ ML/min$, pos. M

(e) $T = 400\ K$, $0.21\ ML$, $r = 0.0231\ ML/min$, pos. M

Figure 4.19.: **AFM images ($10x10\ \mu m$) of 6P on mica at different substrate temperatures**. The shape of the islands developed from small compact islands at low temperature to dendritic and fractal like islands at higher temperature. Also surprising is a bimodal island size distribution at higher temperatures (d,e).

Table 4.4.: **Island densities** at different temperatures, from $10x10\ \mu m$ AFM images (Digital Instruments Nanoscope AFM, Uni Leoben), at 350 K and 400 K only the big islands were taken into account.

Temperature / K	Pos. M	Pos. A	Pos. B	Pos. C	Pos. D	MW
150	24.16	32.32	55.04	39.92	35.44	37 ± 15
200	-	-	-	-	-	-
250	2.69	3.13	-	3.28	2.67	2.9 ± 0.3
300	-	-	2.15	-	2.16	2.2 ± 0.1
350	0.19	0.20	-	0.24	0.30	0.23 ± 0.05
400	0.11	0.09	0.08	0.07	0.10	0.09 ± 0.02

Table 4.5.: **Island densities** at different temperatures, from $8.6x8.6\ \mu m$ AFM images (Nanosurf easy scan2 AFM, TU Graz), at 350 K and 400 K only the big islands were taken into account.

Temperature / K	Pos. M	Pos. A	Pos. B	Pos. C	Pos. D	MW
150	27.47	32.45	50.84	38.94	33.75	37 ± 15
200	8.56	12.66	5.25	10.71	6.14	8.7 ± 4
250	3.3	-	-	3.16	-	3.2 ± 0.1
300	-	2.6	2.06	2.29	2.57	2.4 ± 0.3
350	0.3	0.3	-	0.28	0.26	0.28 ± 0.03
400	0.08	0.11	0.11	0.1	0.11	0.10 ± 0.01

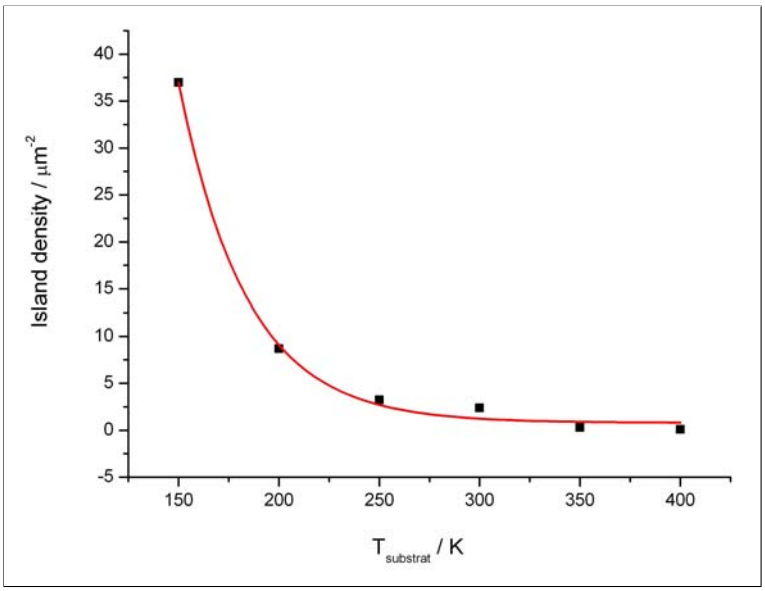

Figure 4.20.: **Island densities at different substrate temperatures** from 8.6x8.6 μm AFM images. One sees that the island density decreases with increasing temperature.

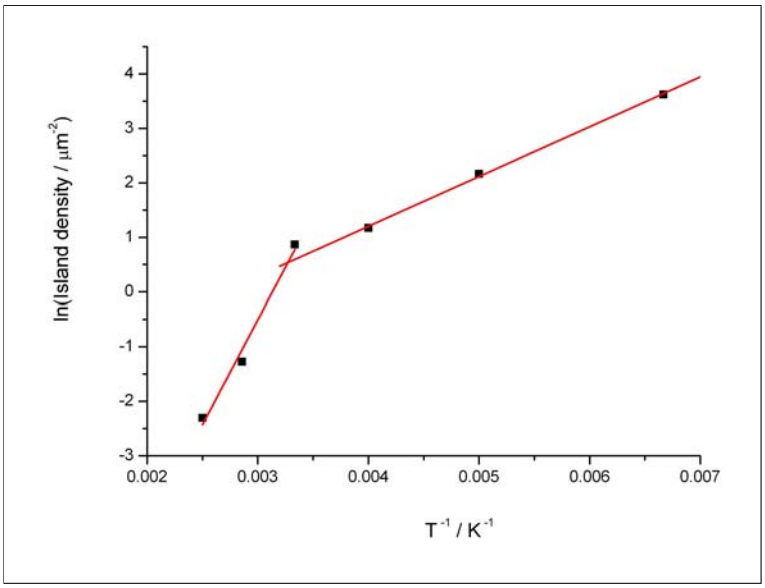

Figure 4.21.: **Island density vs. inverse temperatures** from 8.6x8.6 μm AFM images. The different slope at higher temperatures ($> 300\ K$) indicates a change of the critical island size. At 350 K and 400 K, only the big islands were taken into account.

4.2.3. Variation of the growth rate

The third sample series describes the growth of 6P at different growth rates, the substrate temperature during the island growth was kept at room temperature (300 K) and the coverages of all samples are nearly constant.

Island shapes
In fig.4.22, AFM images with different growth rates from 0.0207 ML/min to 0.481 ML/min are depicted. At small growth rates dendritic islands and at high growth rates small compact islands are visible.

Island densities
In tab.4.6 and tab.4.7, the island densities at different growth rates from different sample positions and corresponding average values are listed, as measured at the TU Graz and the University of Leoben. As mentioned in chap.2.4.1, the island density increases with increasing growth rate acc. to equ.2.1. A plot of the island density from tab.4.6 and tab.4.7 is given in fig.4.23. These informations are used in chap.4.3.1 for the determination of the critical cluster size.

Table 4.6.: **Island densities** at different growth rates, from $10x10$ μm AFM images.

Growth rate / ML/min	Pos. M	Pos. A	Pos. B	Pos. C	Pos. D	MW
0.0207	-	-	2.15	-	2.16	2.2 ± 0.1
0.0451	6.25	10.11	9.04	4.11	4.44	7 ± 3
0.1167	12.14	10.37	9.10	13.87	12.84	12 ± 3
0.2958	21.44	20.24	32	8.8	18.88	20 ± 10
0.4810	24.56	26.32	21.12	29.04	28.48	26 ± 4

Table 4.7.: **Island densities** at different growth rates, from $8.6x8.6$ μm AFM images.

Growth rate / ML/min	Pos. M	Pos. A	Pos. B	Pos. C	Pos. D	MW
0.0207	-	2.6	2.06	2.29	2.57	2.4 ± 0.3
0.0451	7.03	5.41	8.11	-	5.11	6 ± 2
0.1167	14.82	13.25	11.63	14.71	14.6	14 ± 2
0.2958	18.71	14.87	17.14	20.55	27.04	20 ± 6
0.4810	31.96	-	-	-	-	32

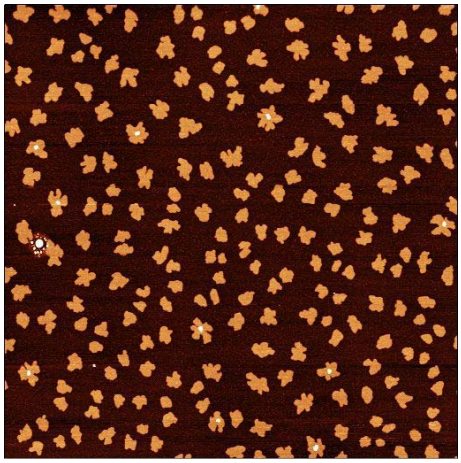

(a) r=0.0207 ML/min, 0.21 ML, pos. B

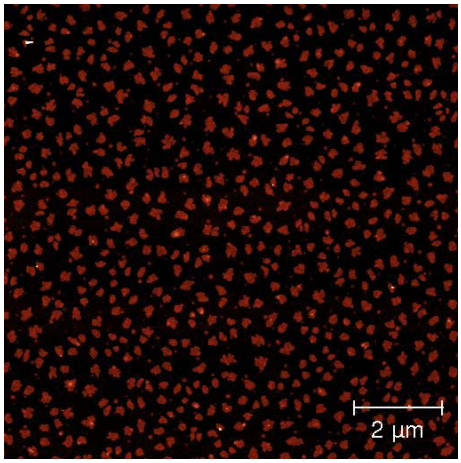

(b) r=0.0451 ML/min, 0.24 ML, pos. M

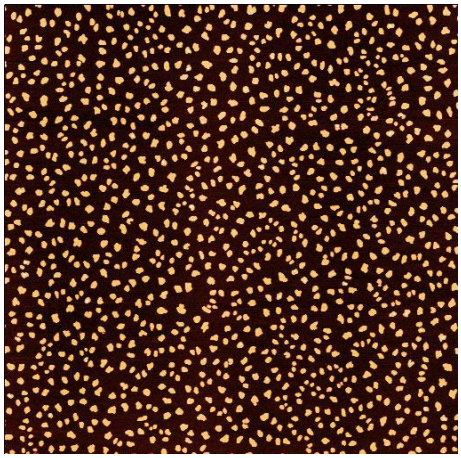

(c) r=0.1167 ML/min, 0.26 ML, pos. M

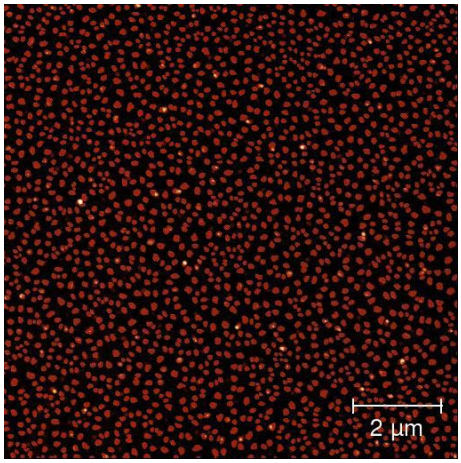

(d) r=0.2958 ML/min, 0.27 ML, pos. M

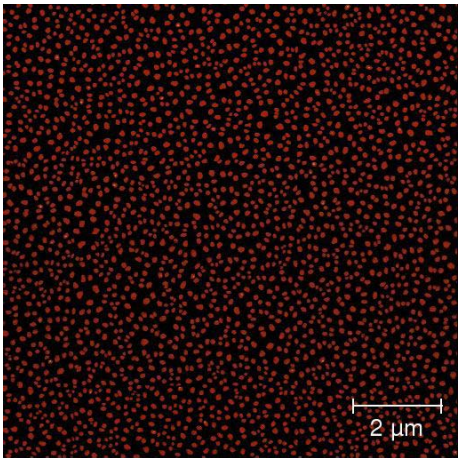

(e) r=0.4810 ML/min, 0.27 ML, pos. M

Figure 4.22.: **AFM images ($10x10$ μm) of 6P on mica with different growth rates** from 0.0207 ML/min to 0.481 ML/min. At small growth rates dendritic islands and at hight growth rates small compact islands are visible.

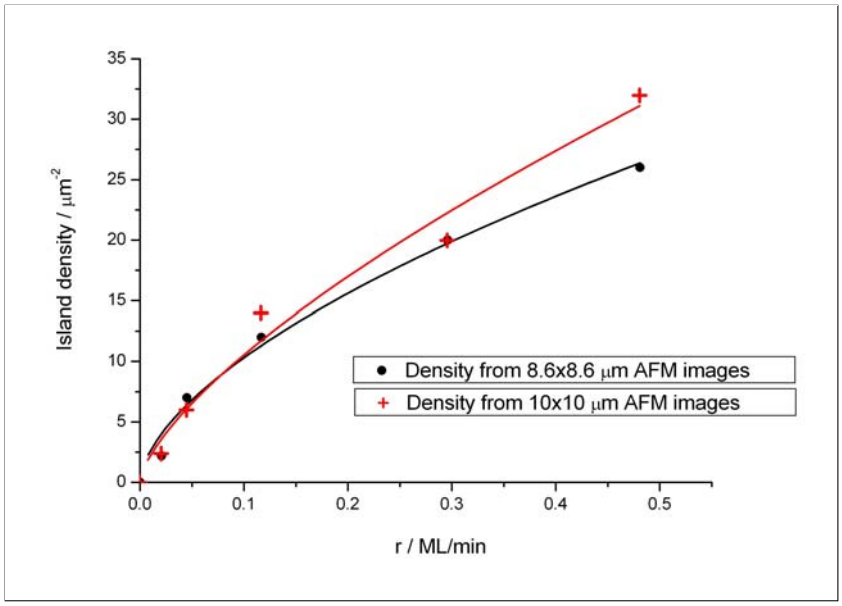

Figure 4.23.: **Island density** at different growth rates, from $10x10\ \mu m$ (tab.4.6) and $8.6x8.6\ \mu m$ (tab.4.7) AFM images. One can see that the island density increases with increasing growth rate acc. to equ.2.1.

4.3. Critical cluster size for nucleation

On the sputtered mica, impinging rod like 6P molecules are diffusing (flat lying) on the surface as long as they encounter some other molecules. Not till then, the molecules stand up and form a stable island. One less than the number of molecules which are necessary to form a stable nucleus, is called the critical cluster size for nucleation (see chap.2.4). There are different ways to determine this, in chap.4.3.1, the variation of the growth rate, in chap.4.3.2, the island area distribution and in chap.4.3.3, the capture zones area distribution will be used (performed by Stefan Lorbek, University of Leoben).

4.3.1. Critical cluster size determined with different growth rates

In chapter 4.2.3 the island density as a function of the growth rate is recorded (fig.4.23). From this we obtain the critical cluster size for nucleation as follows:

- Plot $ln(island\ density)$ versus $ln(growth\ rate)$, see fig.4.24
- The slope B of a linear fit gives the result: $i = \frac{2}{\frac{1}{B}-1}$

See chap.2.4.1 for the derivation.

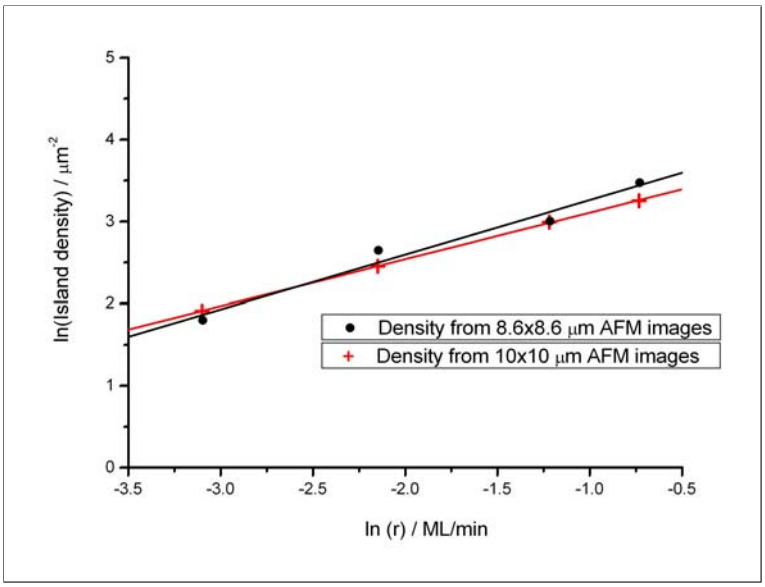

Figure 4.24.: **Determination of the critical cluster size i for nucleation.** Plot of $ln(island\ density\ /\mu m^{-2})$ vs. $ln(growth\ rate)$ with a linear fit, from $10x10\ \mu m$ AFM images: intercept $A = 3.68096$ and slope $B = 0.56946$ and from $8.6x8.6\ \mu m$ AFM images: $A = 3.9220$ and $B = 0.66635$.

This method gives for samples no. 2, 18, 20, 22 (see tab.A.2) with growth rates from 0.0451 to 0.4810 ML/min at 300 K substrate temperature: from $10x10\ \mu m$ AFM images: $i = 2.6$ and from $8.6x8.6\ \mu m$ AFM images: $i = 3.9$. This corresponds to the critical cluster size at 300 K of $i = 3 \pm 1$.

4.3.2. Critical cluster size determined by scaling theory

In this case, as described in chap.2.4.2 a normalised distribution of the island areas was performed. The best fit of this distribution with the scaling function 4.1 gives the critical nucleus size i.

$$f(u) = C_i u^i exp(-b_i i u^{1/b_i}) \tag{4.1}$$

The numerical values of the parameters are fixed by the implicit hypergeometrical equations:

$$\frac{\Gamma[(i+2)b_i]}{\Gamma[(i+1)b_i]} = (ib_i)^{b_i} \tag{4.2}$$

and

$$C_i = \frac{(ib_i)^{(i+1)b_i}}{b_i \Gamma[(i+1)b_i]} \tag{4.3}$$

whereas Γ is the gamma function:

$$\Gamma(x) = \int_0^\infty t^{x-1} e^{-t} dt \tag{4.4}$$

Determination of the scaling function parameters

First the parameters b_i and C_i were determined for different i, according to equ.4.2 and 4.3. The b_i was obtained by the point of intersection of the left and right side of equ.4.2. In fig.4.25, for instance $i = 1$, the red line corresponds to the left side of equ.4.2 and the blue one to the right. In tab.4.8, the determined values for b_i and C_i for i up to 6 are listed.

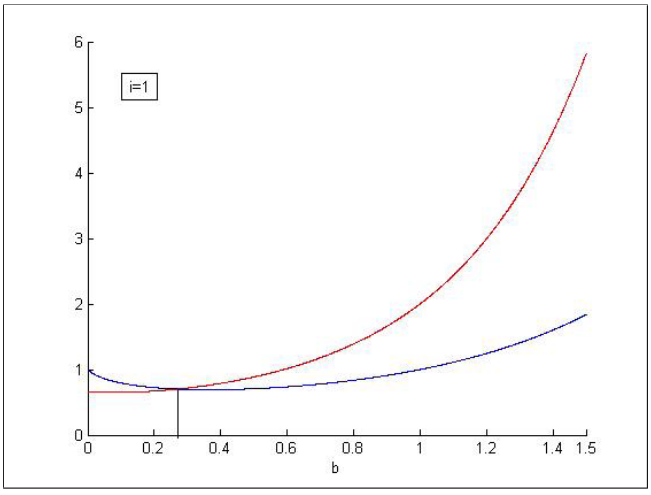

Figure 4.25.: **Determination of the scaling parameter** b_1. The red line corresponds to the left side of equ.4.2 and the blue one to the right. The point of intersection is at $b_1 = 0.2715$.

Table 4.8.: **Determined scaling parameters** b_i, C_i and i acc. to equ.4.2 and 4.3.

i	b_i	C_i
1	0.2715	1.1091
2	0.2976	1.9678
3	0.3086	3.2385
4	0.3145	5.1214
5	0.3182	7.9036
6	0.3207	11.9963

Island size distribution

The island size distribution was determined by Gwyddion (chap.A.4) with the help of a mask (fig.A.4(f)). This corresponding ASCII file was load in a Matlab program (chap.A.5) where a histogram of this distribution was compared with the scaling function equ.4.1 for different i. The best match gives the critical cluster size i, as shown in tab.4.9 for different AFM images and corresponding average values MW of different positions. Fig.4.26 to 4.28 show the average value of the island size distribution from tab.4.9. An error because of less coverage, due to artefact removal in the AFM image especially at the border, appears (higher distribution). Also because of a wrong average value of the island areas A due to artefacts, a peak shift and height error may be observed.

From the scaling theory one observes: $i = 3 \pm 1$.

Table 4.9.: **Scaling theory.** The critical cluster size i was determined from the island size distribution of $10x10$ μm AFM images at different positions (MW... Average value). At higher substrate temperatures (sample 9 and 17) there are insufficient islands for a distribution.

Sample no.	Parameter	Pos. M	Pos. A	Pos. B	Pos. C	Pos. D	MW
1	0.08 ML	3	3	3	2-5	3	3
14	0.21 ML	-	-	3	-	4	3
3	0.33 ML	2	3	3	3	3	3
4	0.61 ML	3	3	3	3	3	3
15	150 K	3	3	2	3	3	2
16	200 K	-	-	-	-	-	-
8	250 K	3	3	-	3	2	3
14	300 K	-	-	3	-	4	3
14	0.021 ML/min	-	-	3	-	4	3
2	0.045 ML/min	3	3	-	3	3	3
18	0.117 ML/min	4	3	3	4	4	3-4
20	0.296 ML/min	3	2	2	3	2	2-3
22	0.481 ML/min	2	3	3	3	2	2-3

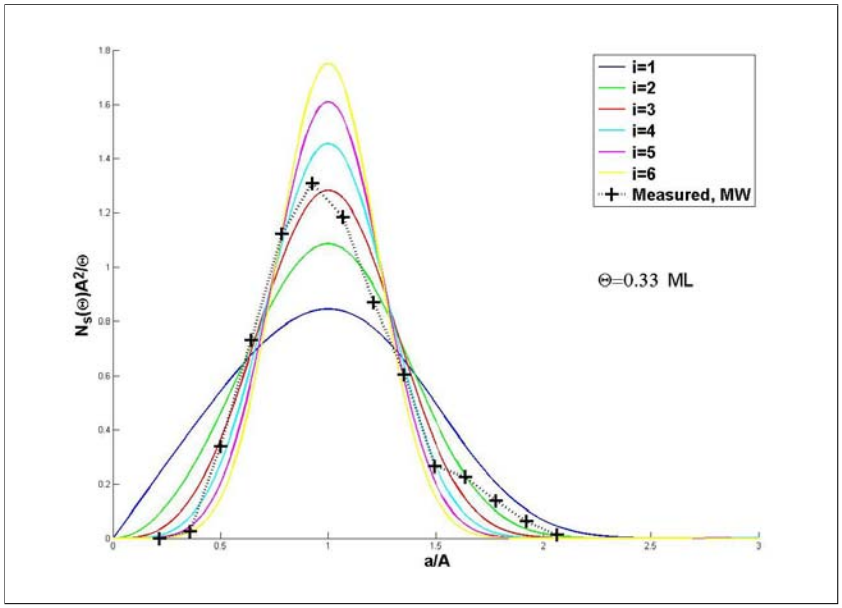

(a) Scaling theory, sample 3

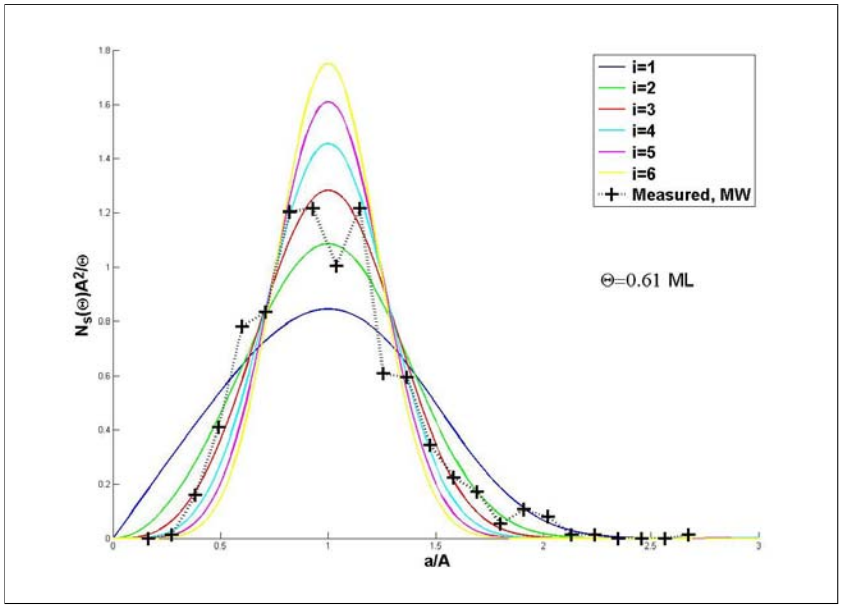

(b) Scaling theory, sample 4

Figure 4.26.: **Critical cluster size i determined by scaling theory.** Scaled distribution from islands of size a (with mean value A), at different 6P coverages $\Theta = 0.33\ ML$ and $0.61\ ML$ at a substrate temperature of $T = 300\ K$; $i = 3$, MW... Average value of different positions on the sample, see tab.4.9.

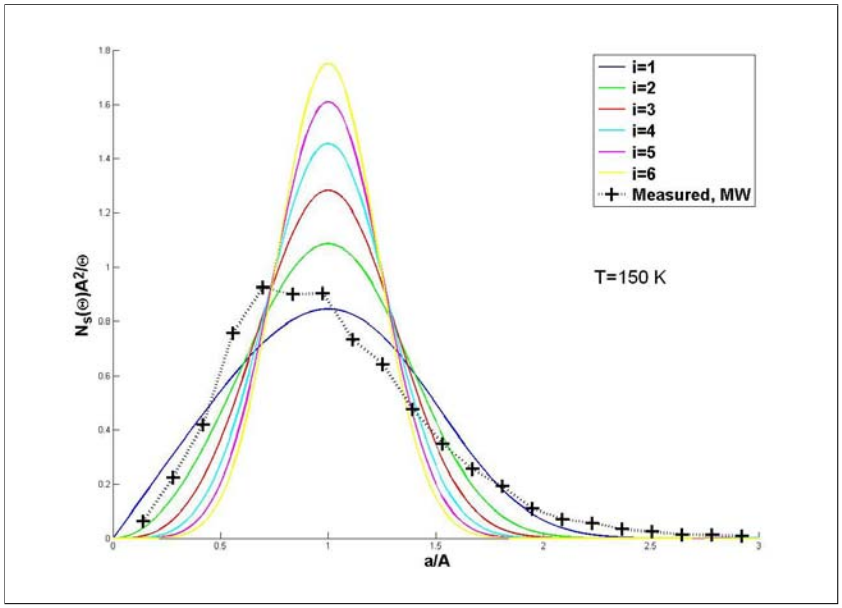

(a) Scaling theory sample 15

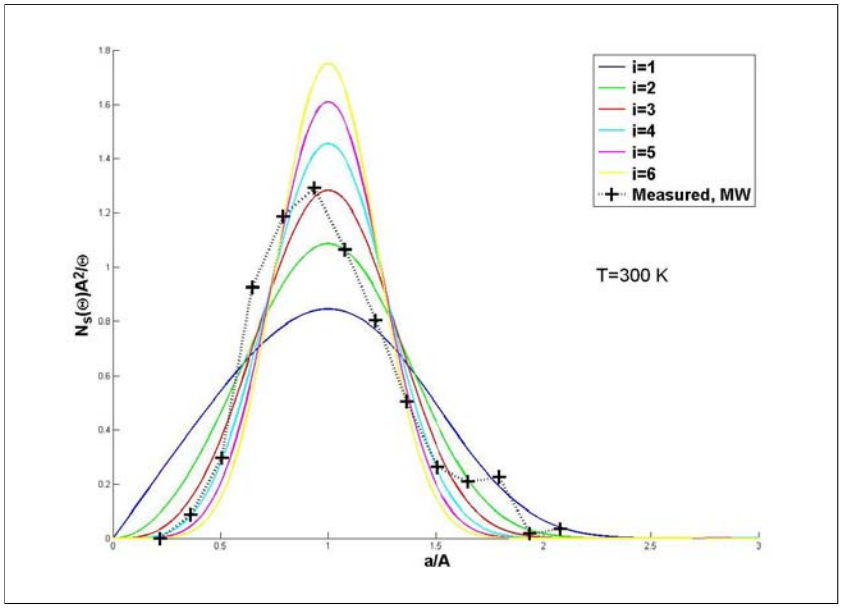

(b) Scaling theory sample 14

Figure 4.27.: **Critical cluster size i determined by scaling theory.** Scaled distribution from islands of size a (with mean value A), at different substrate temperatures $T = 150\ K$ $(i = 2)$ and $T = 300\ K$, $\Theta = 0.22\ ML$ $(i = 3)$, MW... Average value of different positions on the sample, see tab.4.9.

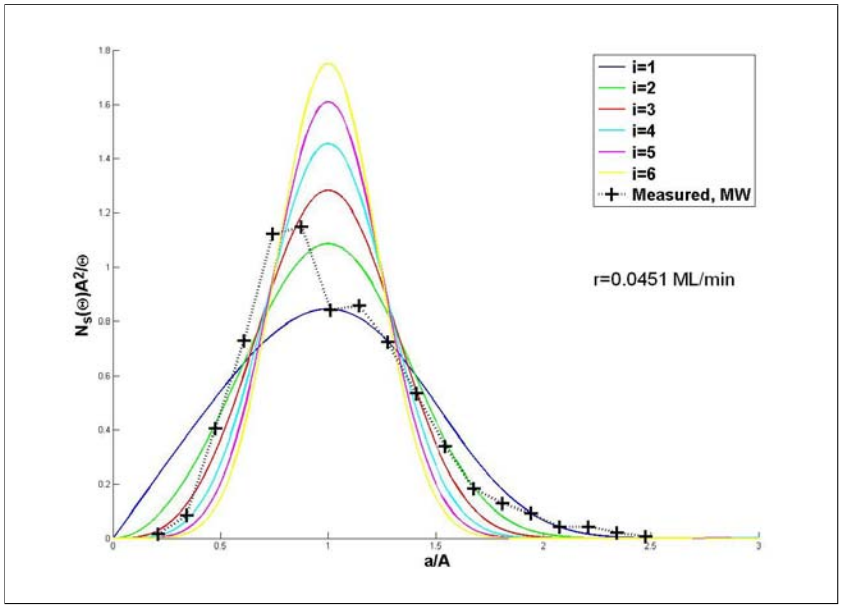

(a) Scaling theory, sample 2

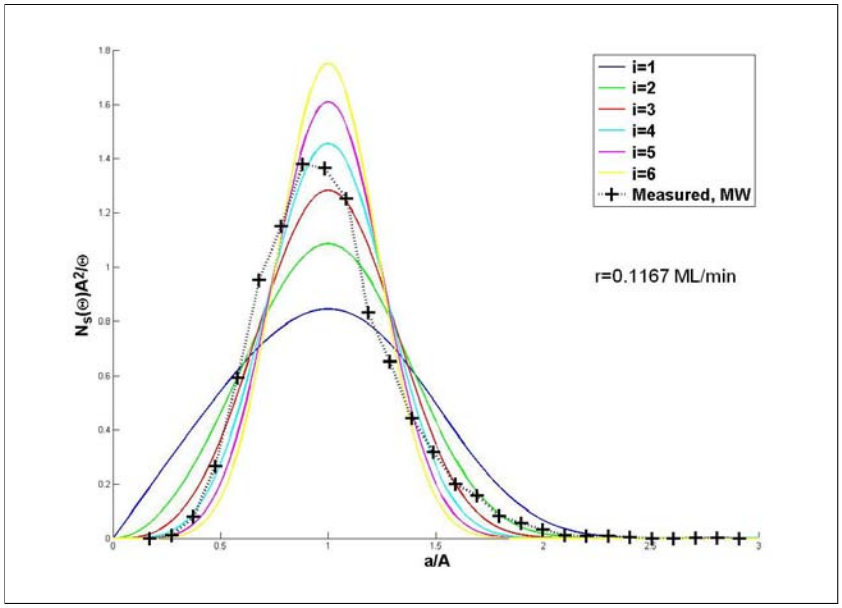

(b) Scaling theory, sample 18

Figure 4.28.: **Critical cluster size i determined by scaling theory.** Scaled distribution from islands of size a (with mean value A), at different growth rates 0.045 ML/min ($i = 3$) and 0.117 ML/min ($i = 3 - 4$) at $T = 300\ K$, $\Theta = 0.25\ ML$, MW... Average value of different positions on the sample, see tab.4.9.

4.3.3. Critical cluster size determined by Voronoi analysis

This evaluation method[2] (chap.2.4.3) starts with the so called Voronoi tesselation (fig.4.29), where a matlab program determines the centers of the islands in the AFM picture. Around each island a zone of the half distance to all nearest neighbours is established. This zones are called capture zones of the islands, their normalised area distribution is depicted in fig.4.30 from sample 2 with 0.24 ML 6P. The best fit with the generalized Wigner surmise (GWS):

$$P_\beta(s) = a_\beta s^\beta exp(-b_\beta s^2) \tag{4.5}$$

gives the critical nucleus size i. For the parameters see chap.2.4.3.
This is only possible for coverages up to 0.33 ML, because at heigher coverage the islands are too big and they already touching each other, this makes it impossible for the program to distinguish between different islands.
For samples with 0.08, 0.24 and 0.33 ML coverage at 300 K substrate temperature, this methode gives $i = 4 \pm 1$.

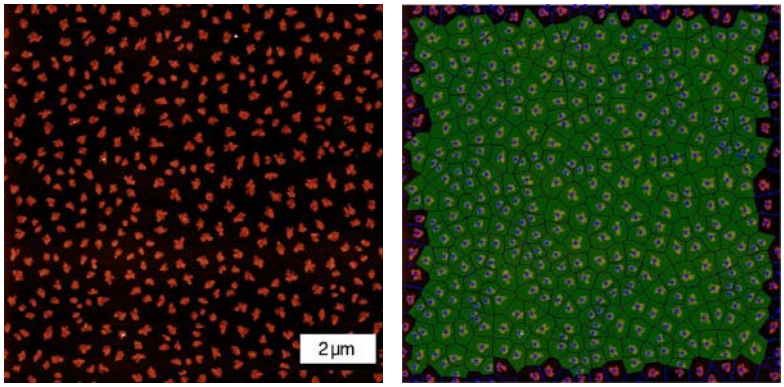

(a) AFM image of sample 2, pos. B (b) Voronoi tesselation

Figure 4.29.: **Voronoi tesselation.** AFM image of 6P on sputtered mica without and with tesselation by a matlab program.

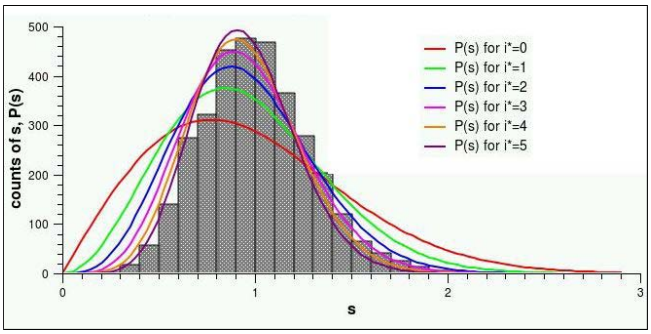

Figure 4.30.: **Voronoi analysis**. One sees the normalised capture zone size distribution and the generalized Wigner surmise (equ.4.5) for different i from sample 2 (0.24 ML 6P), the best match gives the critical cluster size $i = 4 \pm 1$.

[2]performed by Stefan Lorbek, University of Leoben

4.4. Determination of the desorption energy and frequency factor

In this section, the desorption energy (E_{Des}) and the frequency factor (ν_n, see chap.2.5.4) for the monolayer were determined by the heating rate variation method and for the multilayer by the method as described in chap.2.5.4 for zero order desorption.

4.4.1. Monolayer

Heating rate variation method

In the thesis by Frank [4], the desorption energy for the monolayer was determined by the Redhead formula (equ.2.21) by using the frequency factor from the multilayer ($\nu_0 = 10^{25}\ Hz$). To determine the frequency factor for the monolayer directly, the heating rate variation method was used. This method is based on the collection of a series of spectra with the same coverage but different heating rates β. From each spectrum, the temperature of the monolayer (β_1) desorption rate maximum is determined.

The concrete procedure was done in the following way:

- Recording spectra with about 1 ML coverage and heating rates from 0.2 to 5 K/s
- Read out the temperature of the peak maxima
- Offset alignment
- E_{Des} (uncorrected) from the slope of plot $ln(\beta/T_m^2)$ vs. $1/T_m$
- ν_1 (uncorrected) from the intercept of this plot
- Temperature correction
- E_{Des} (corrected) from the slope of plot $ln(\beta/T_m^2)$ vs. $1/T_m$
- ν_1 (corrected) from the intercept of this plot

In tab.4.10, the temperature values of the peak maxima are shown, the correction was done as described in chap.A.1. With the equation 2.20, one gets from the linear fit ($y = A + B \cdot x$) in the plot fig.4.31:

- Intercept $A = 17.4$
- Slope $B = -29100$

This gives for the desoption energy and frequency factor:

Monolayer (uncorrected): $E_{Des} = 2.5\ eV$ and $\nu_1 = 1 \cdot 10^{12}\ Hz$

But here it is not taken into account, that the temperature of the mica is not the same as the temperature on the steel plate. With the temperature correction (chap.A.1), one gets a new plot (fig.4.32), it gives:

- Intercept $A = 44.3$

- Slope $B = -29492$

Table 4.10.: **Different heating rates.** β... Heating rate of the steel plate, β'... Heating rate of mica ($\beta' = \beta \cdot (T_{Ta} - T_{init})/(T_{\alpha-uncorr.} - T_{init})$), T_{Ta}... Temperature of the multilayer peak maximum from the fixation wires ($\pm$ 10 K), $T_{\alpha-uncorr.}$... Temperature of multilayer desorption from mica (not corrected), T_{β_1}... Temperature of the monolayer peak maximum ($\pm$ 10 K), the TD spectra startet at an initial temperature of $T_{init} = 300\ K$ (chap.A.1).

$\beta\ K/s$	$\beta'\ K/s$	T_{Ta}	$T_{\alpha-uncorr.}$	$T_{\beta_1}(uncorr.)$	$T_{\beta_1}(corr.)$
5	1.83	504	857	957	541
4.5	1.64	501	853	955	538
4	1.46	500	847	946	536
3.5	1.31	500	836	948	542
3	1.13	498	826	939	541
2.5	0.94	495	821	933	537
2	0.75	493	818	926	533
1.5	0.56	490	806	917	532
1	0.38	486	794	913	531
0.8	0.3	486	790	904	529
0.6	0.23	480	784	896	522
0.5	0.19	477	781	885	515
0.4	0.15	479	775	884	520
0.3	0.11	475	768	891	521
0.2	0.08	477	763	872	519

This gives for the desorption energy and frequency factor:

Monolayer (corrected): $E_{Des} = (2.6 \pm 0.3)\ eV$ and $\nu_1 = 5.3 \cdot 10^{23\pm2}\ Hz$

This frequency factor is significantly larger than the commonly assumed frequency factor $\nu = 10^{13}\ Hz$ for small molecules.

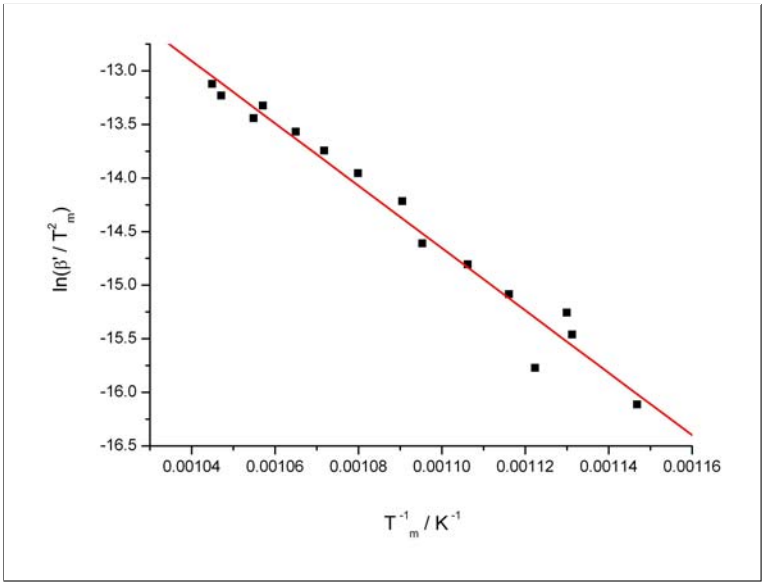

Figure 4.31.: **Heating rate variation method.** Plot of $ln(\beta'/T_m^2)$ vs. $1/T_m$ with no temperature correction, the 6P coverage is 1 ML. The linear fit gives: $E_{Des} = 2.5\ eV$ and $\nu_1 = 1 \cdot 10^{12}\ Hz$.

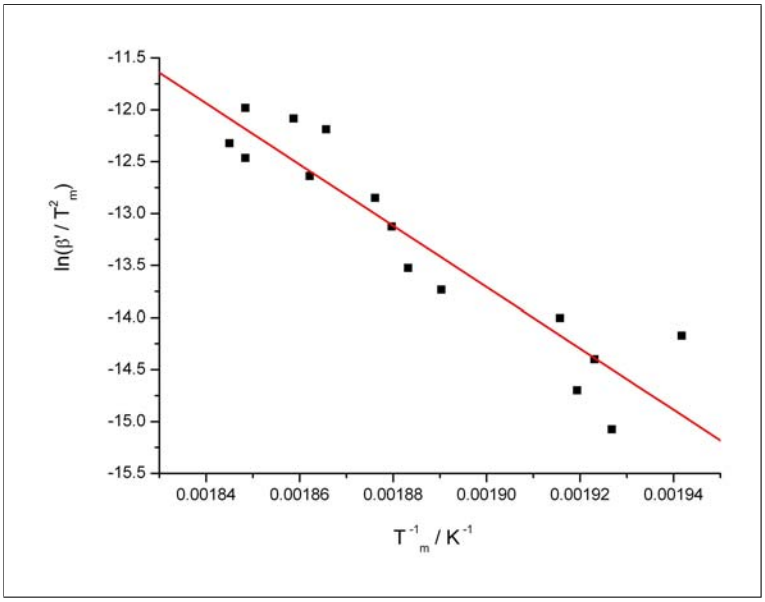

Figure 4.32.: **Heating rate variation method.** Plot of $ln(\beta'/T_m^2)$ vs. $1/T_m$ with temperature correction, the 6P coverage is 1 ML. The linear fit gives: $E_{Des} = (2.6 \pm 0.3)\ eV$ and $\nu_1 = 5.3 \cdot 10^{23\pm2}\ Hz$.

4.4.2. Multilayer

For the determination of the desorption energy of the multilayer, we use the method as described in chap.2.5.4 for zero order desorption and compare it with the evaporation enthalpy from the Knudsen cell. The multilayer desorption should be similar to the multilayer desorption energy of 6P from different substrates:

- 6P on Au(111) [33]: $E_{Des} = 2.4\ eV$

In fig.4.33, one can see the recorded TD spectra (mass 61) as a function of the measured temperature and corrected temperature acc. to chap.A.1. These spectra were used to determine the desorption energy as described in chap.2.5.4. The first peak comes from 6P deposited on the heating wires, a fast temperature increase leads to a narrow peak. The second peak comes from 6P on the fixation wires and the third from 6P on mica (multilayer). From the slope of the plot $ln(r)$ vs. $1/T$ (fig.4.34) and the Polanyi-Wigner equation for zero order desorption (4.6):

$$r = \nu_0 \Theta_{max} exp(-\frac{E_{Des}}{R \cdot T}) \tag{4.6}$$

one obtains:

- Without T-correction: $E_{Des} = (3.1 \pm 0.1)\ eV$
- With T-correction: $E_{Des} = (3.1 \pm 0.1)\ eV$

This is not in agreement with the literature value, also the desorption energy of the multilayer is here higher than that of the monolayer. We conclude, that a too small coverage ($4\ ML$) for a multilayer desorption was used. Additionally, the temperature correction for this method might not be good enough.

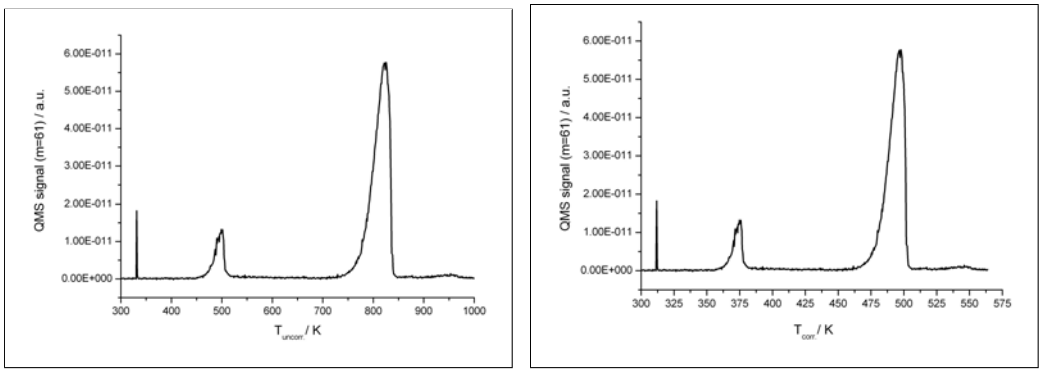

(a) Without T-correction (b) With T-correction

Figure 4.33.: **TD spectra from 6P on mica.** QMS signal of mass 61 as a function of the measured and corrected temperature. The multilayer peak at about 800 K (a) moves after correction (chapt.A.1) to about 500 K (b). The smaller peak comes from the desorption of 6P from the fixation wires. The heating rate is 1 K/s and the coverage is 4 ML.

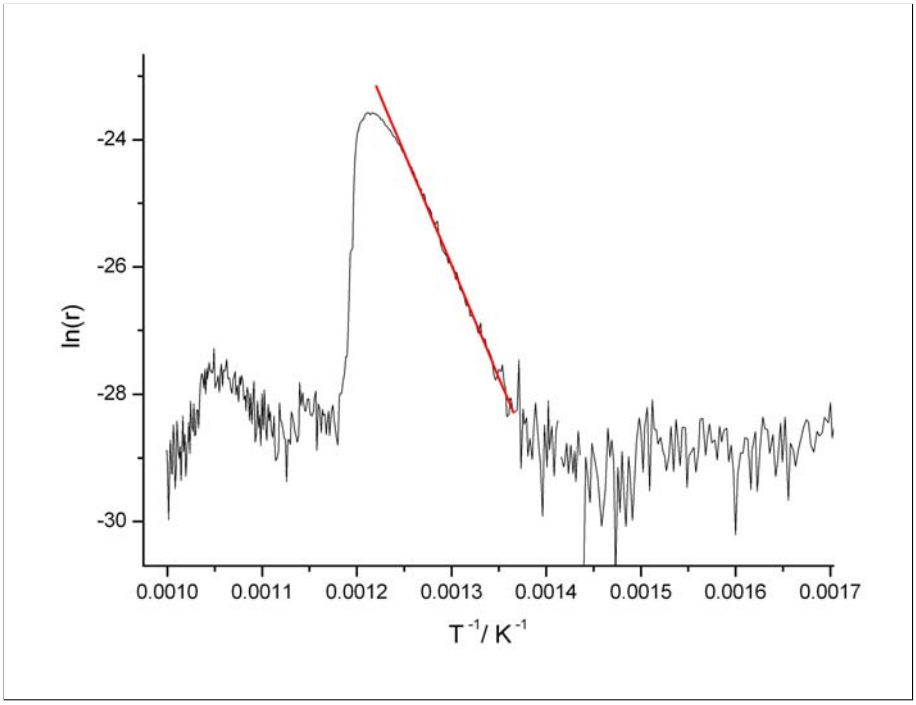

(a) Plot of $ln(r)$ vs. $1/T$ without T-correction. The linear fit ($y = A + B \cdot x$; $A = 20$, $B = -35368$) gives: $E_{Des} = (3.1 \pm 0.1)\ eV$.

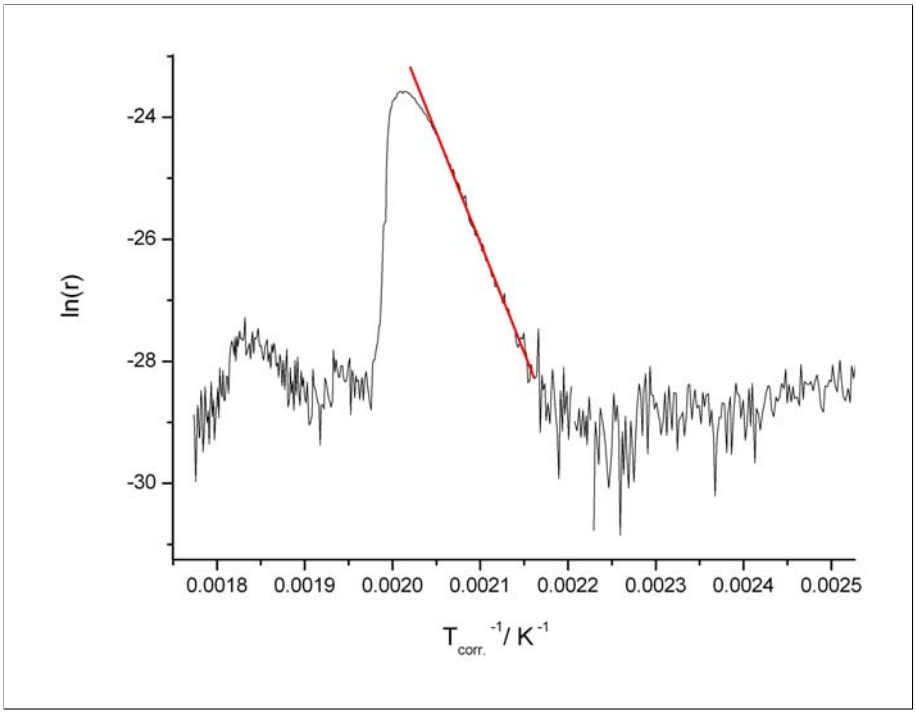

(b) Plot of $ln(r)$ vs. $1/T$ with T-correction. The linear fit ($y = A + B \cdot x$; $A = 49.5$, $B = -35991$) gives: $E_{Des} = (3.1 \pm 0.1)\ eV$.

Figure 4.34.: **Determination of the desorption energy of the multilayer.**

To determine the frequency factor for the multilayer one must use the absolute desorption rate r_{abs} (in $molecules/cm^2 s$), as described in [33].
According to fig.4.35, one obtains:

- Without T-correction: $\nu_0 = 1.40 \cdot 10^{19\pm5}\ Hz$
- With T-correction: $\nu_0 = 1.05 \cdot 10^{33\pm5}\ Hz$

In Ref. [33] a frequency factor (with T-correction) of $\nu_0 = 10^{25}\ Hz$ is given.

Evaporation enthalpy

The evaporation from the Knudsen cell (chap.3) can be used as an independent determination of the multilayer desorption energy. Fig.4.36(a) shows an exponential correlation of the evaporation rate (r) as a function of the temperature of the Knudsen cell. From the slope of the linear fit (B) in fig.4.36(b) and 4.37(b) and with:

$$r \propto e^{-\frac{H}{R \cdot T}} \tag{4.7}$$

one obtains for the evaporation enthalpy:

- Without correction: $H = (2.0 \pm 0.1)\ eV$
- With correction (chap.A.2): $H = (2.2 \pm 0.1)\ eV$

This is in agreement with the literature value for 6P multilayer desorption from Au(111) ($E_{Des} = 2.4\ eV$) [33]. The correction was necessary because of a not cooled quartz microbalance.

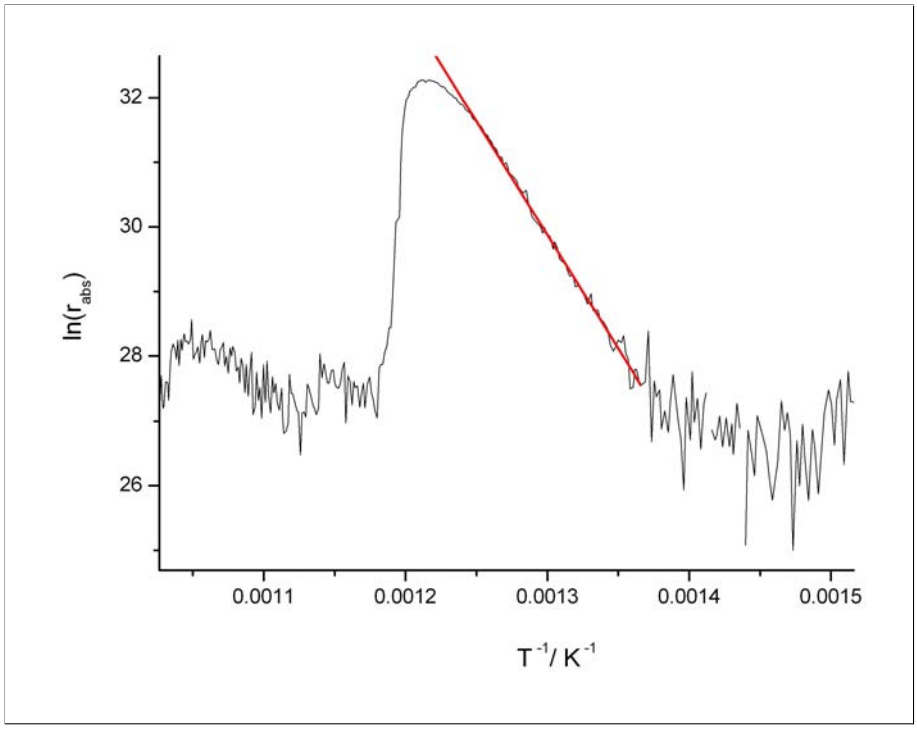

(a) Plot of $ln(r_{abs})$ vs. $1/T$ without T-correction. The linear fit ($y = A + B \cdot x$; $A = 75.6,\ B = -35172$) gives: $\nu_0 = 1.40 \cdot 10^{19\pm5}\ Hz$.

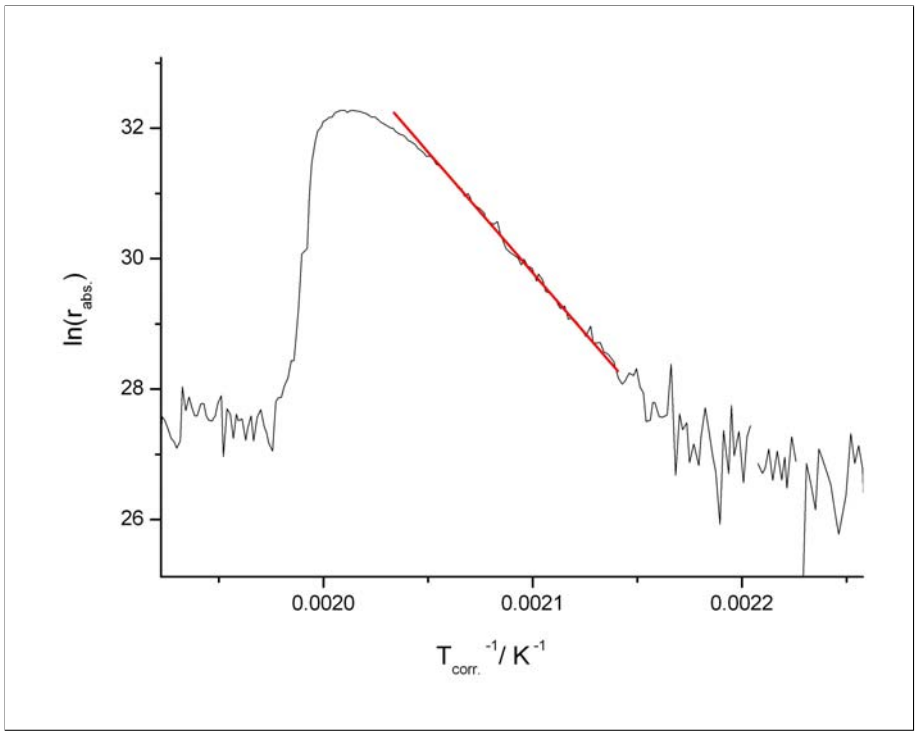

(b) Plot of $ln(r_{abs})$ vs. $1/T$ with T-correction. The linear fit ($y = A + B \cdot x$; $A = 107.6,\ B = -37032$) gives: $\nu_0 = 1.05 \cdot 10^{33\pm5}\ Hz$.

Figure 4.35.: **Determination of the frequency factor of the multilayer** with absolute desorption rate.

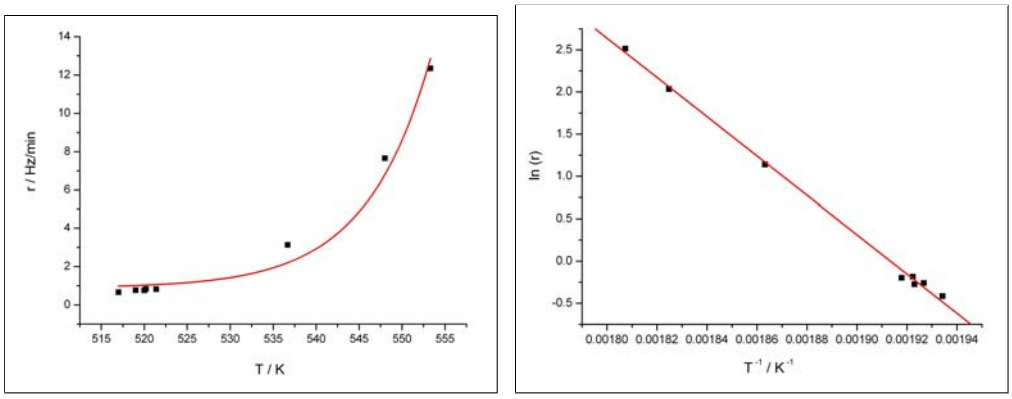

(a) r vs. T (b) $ln(r)$ vs. T^{-1}

Figure 4.36.: **Evaporation enthalpy without correction** acc. to chap.A.2. In (a), the evaporation rate vs. cell temperature shows an exponential behaviour. In (b), one sees a plot of $ln(r)$ vs. the inverse temperature, from the linear fit: $y = A + B \cdot x$, $(A = 44.5,\ B = -23273)$, one obtains the evaporation enthalpy: $H = (2.0 \pm 0.1)\ eV$.

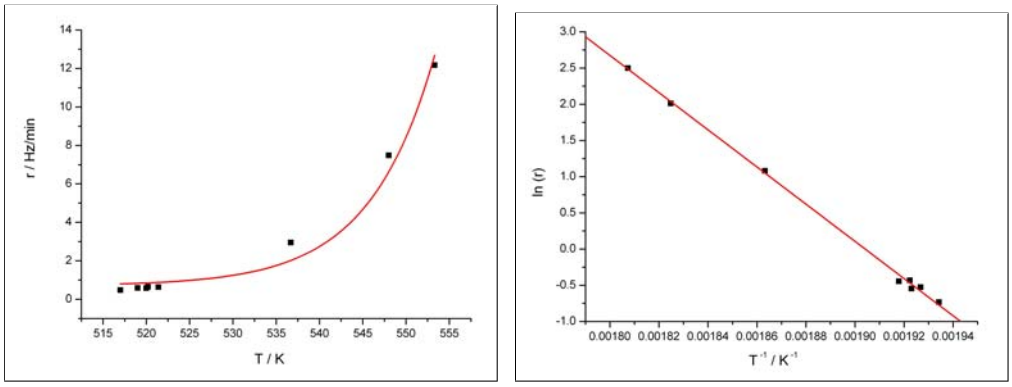

(a) r vs. T (b) $ln(r)$ vs. T^{-1}

Figure 4.37.: **Evaporation enthalpy with correction** acc. to chap.A.2. In (a), the evaporation rate vs. cell temperature shows an exponential behaviour. In (b), one sees a plot of $ln(r)$ vs. the inverse temperature, from the linear fit: $y = A + B \cdot x$, $(A = 48.9,\ B = -25677)$, one obtains the evaporation enthalpy: $H = (2.2 \pm 0.1)\ eV$, in agreement with the literature value for 6P multilayer desorption from Au(111) [33].

5. Summary and conclusions

In this work we focused on the nucleation and sub-monolayer growth of para-hexaphenyl (6P) on an Ar^+ sputtered mica(001) surface. The modification of the mica surface by sputtering leads to the formation of mounds consisting of standing molecules instead of needle like islands consisting of flat lying molecules on top of a wetting layer. The island shapes, densities, heights and molecule orientation of 6P on mica were investigated by atomic force microscopy (AFM) and transverse shear microscopy (TSM) at samples with different coverages (chap.4.2.1), temperatures (chap.4.2.2) and growth rates (chap.4.2.3). The main issue of this work was the determination of the critical island size, since this governs the further layer growth and film formation.

Growth behaviour

Samples at 300 K with different coverages show a constant island density from 0.2 to 0.6 ML (aggregation regime) of (2.1 ± 0.5) μm^{-2}. At low coverages, dendritic islands are visible, at higher coverages, the islands become more compact and straight boundaries between coalescing islands appear. The island height is (2.3 ± 0.5) nm, corresponding to roughly the length of the 6P molecule (2.7 nm), indicating that the islands are composed of standing molecules. The molecules are not standing exactly perpendicular to the surface, each island has its own tilt direction. With transverse shear microscopy (TSM), one sees a random distribution of the island molecule orientation. Surprisingly one can see that at and above 0.87 ML, hexagonal islands in the second layer appear.
On samples at low temperature the islands are compact and at higher temperature dendritic islands are visible. This is opposite to the classical behavior of metal film growth. At high temperature, additionally small islands are visible (bimodal island size distribution). In the vicinity of the big islands, the small ones are not present (denuded zones). The island density decreases with increasing temperature.
Samples at 300 K with small growth rates show dendritic islands and at hight growth rates small compact islands are visible. The island density increases with increasing growth rate.

Critical cluster size for nucleation

Three different methods to determine the critical cluster size for nucleation were applied. In chap.4.3.1 the variation of the growth rate, in chap.4.3.2 the island area distribution and in chap.4.3.3 the capture zones area distribution was used to determine the critical island size. From the different growth rates one obtains for $i = 3 \pm 1$ at a temperature of 300 K. The scaling theory also gives at this and lower temperature $i = 3 \pm 1$. At higher temperatures (> 300 K), a bend in the plot ln(island density) vs. $1/T$ is observed,

this indicates a change of the critical island size. The Voronoi tesselation method gives for samples with 0.08, 0.24 and 0.33 ML coverage at 300 K substrate temperature: $i = 4 \pm 1$. From all this we conclude that $i = 3 \pm 1$ and not unity, as assumed in the previous literature [34].

Desporption energy and frequency factor

Additionally, the desorption energy and frequency factor for the monolayer desorption was determined: $E_{Des} = (2.6 \pm 0.3)\ eV$ and $\nu = 5.25 \cdot 10^{23\pm2}\ Hz$. This frequency factor is significantly larger than the commonly assumed frequency factor $\nu = 10^{13}\ Hz$ for small molecules.
For the multilayer one gets $E_{Des} = (3.1 \pm 0.1)\ eV$, which is not in agreement with the literature value, probably due to an incorrect temperature correction or a too small amount of the multilayer coverage. The evaporation enthalpy of 6P is $H = (2.2 \pm 0.1)$ eV, in agreement with the literature value for 6P multilayer desorption from Au(111) ($E_{Des} = 2.4\ eV$).

A. Supplements

A.1. Temperature correction

The mica is mounted on a steel plate as shown in fig.A.1, where the thermocouple measures the temperature on the backside. Therefore the real temperature of the mica during heating, due to a bad conductivity, is different from the indicated one, depending on the heating rate. In fig.A.2, one can see the temperature increase of the steel plate compared to an assumption of the temperature increase of mica as a function of time. Equ.A.1 gives the corrected temperature of the mica.

$$T_{mica} = T_{init} + k_\beta \cdot (T_{tc} - T_{init}) \tag{A.1}$$

T_{init}... The steel plate and mica have the same temperature, typically $T_{init} = 300\ K$.
T_{tc}... Temperature measured by a thermocouple on the steel plate.

The slope k_β can be derived by the position of the tantalum peak in the TDS (T_{Ta}, which comes from the fixation wires) and the α-peak ($T_{\alpha-uncorr.}$, which comes from the mica).

$$k_\beta = \frac{T_{Ta} - T_{init}}{T_{\alpha-uncorr.} - T_{init}} \tag{A.2}$$

Figure A.1.: **Mica mounted on the steel plate.** The tantalum wires in the front fix the transparent mica sample on the plate, on these wires also 6P is deposited, hence in the TDS a so called 'tantalum' peak appears. The wires have nearly the same temperature as measured on the backside of the plate with the thermocouple on the right.

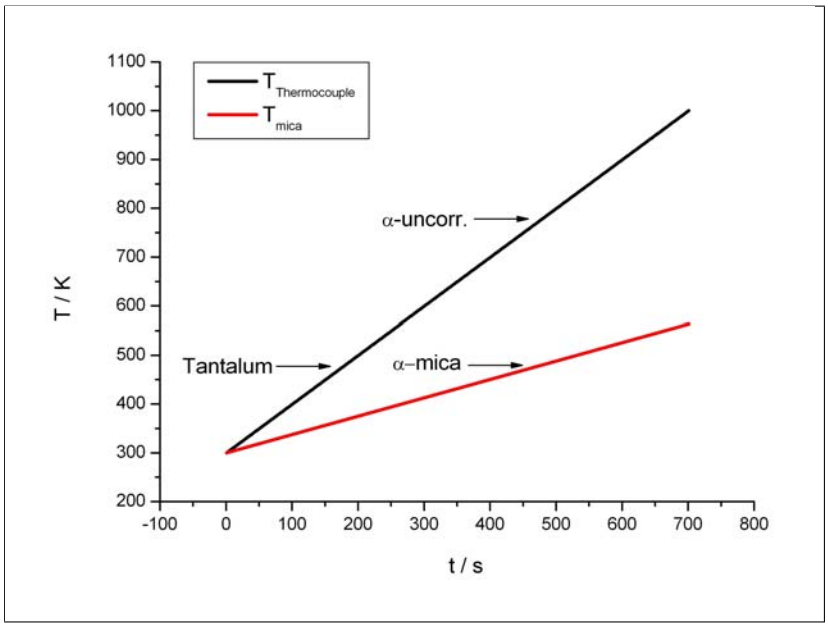

Figure A.2.: **The different temperature increase of the steel plate and the mica** is due to a bad heat conductivity, acc. to equ.A.1. The temperature of the tantalum peak should be equal to the multilayer desorption temperature.

A.2. Microbalance temperature shift correction

Unfortunately, the quartz microbalance was not cooled, so a temperature shift correction acc. to equ.A.3 was necessary.

$$\Theta_{corr.} = \Theta - (k \cdot t) \tag{A.3}$$

Where Θ is the uncorrected coverage in Hz, $\Theta_{corr.}$ the corrected value and t is the deposition time in s. To obtain the constant k in Hz/s, the quartz microbalance frequency change Δf in Hz at closed shutter was measured within a certain time Δt in s:

$$k = \frac{\Delta f}{\Delta t} = \frac{0.9}{300} = 0.003\ Hz/s \tag{A.4}$$

In tab.A.1, the corrected and uncorrected coverage and growth rates are depicted.

A.3. Thickness calibration

The coverage was determined by a quartz microbalance, the frequency change (in Hz, corrected value acc. to chap.A.2) indicates the deposited 6P on the sample. After the investigation by AFM the coverage was determined by Gwyddion (chap.A.4) in percentage of a full monolayer (ML). The correlation between the coverage as determined by the quartz microbalance and the AFM is shows in fig.A.3. Since for the 22 Hz case

Table A.1.: **Microbalance temperature shift correction**. Coverage (in Hz, in ML see chap.A.6and growth rate of the samples. After the investigation by AFM the coverage was determined by Gwyddion (chap.A.4) in percentage of a full monolayer (ML), t... Deposition time, corr... Corrected value.

Sample no.	t s	Coverage Hz	Coverage corr. Hz	Coverage AFM percentage	Growth rate ML/min	Growth rate corr. ML/min
1	312	3	2.06	8.75	0.0185	0.0157
14	596	7	5.21	22.59	0.0226	0.0207
3	577	10	8.27	32.23	0.0333	0.0340
4	1533	20	15.40	60.34	0.0251	0.0238
5	2631	30	22.11	79.21	0.0219	0.0199
21	3375	35	24.88	90.29	0.0200	0.0175
6	2820	40	31.54	99.95	0.0273	0.0265
8	550	7	5.35	22.22	0.0245	0.0231
9	638	7	5.09	21.12	0.0211	0.0189
15	513	7	5.46	24.30	0.0263	0.0252
16	505	7	5.49	14.00	0.0267	0.0258
17	549	7	5.35	12.50	0.0245	0.0231
19	1307	7	3.08	1.71	0.0103	0.0056
2	318	7	6.05	18.69	0.0424	0.0451
18	134	7	6.60	22.21	0.1005	0.1167
20	55	7	6.84	21.25	0.2458	0.2958
22	34	7	6.90	26.00	0.3961	0.4810

already 2nd layer formation takes place, this value was not taken into account for the determination of the proportionality. The linear fit gives for a full ML 25 Hz. This allows now the calibration of the quartz microbalance in terms of coverage.

A.4. Treatment and evaluation of the AFM images by Gwyddion

The programm Gwyddion was used for the treatment and evaluation of the AFM images, it can be free downloaded from [36]. In the following, the steps from the raw data to ready images are shown, detailed information of this program can be found in the manual [27]. In fig.A.4(a) one can see how the raw files look like, islands may not be visible. The 'match line correction' (fig.A.4(b)) aligns the individual scan lines. The 'polynomical background' of the given order (fig.A.4(c)) can be subtracted, 'horizontal scars' can also be removed (fig.A.4(d)). For a better illustration, the height can be rescaled in colours (fig.A.4(e)). Also cross sections from arbitrary lines can be extracted and some statistics can be done, for instance the island size distribution with the help of a mask (fig.A.4(f)).

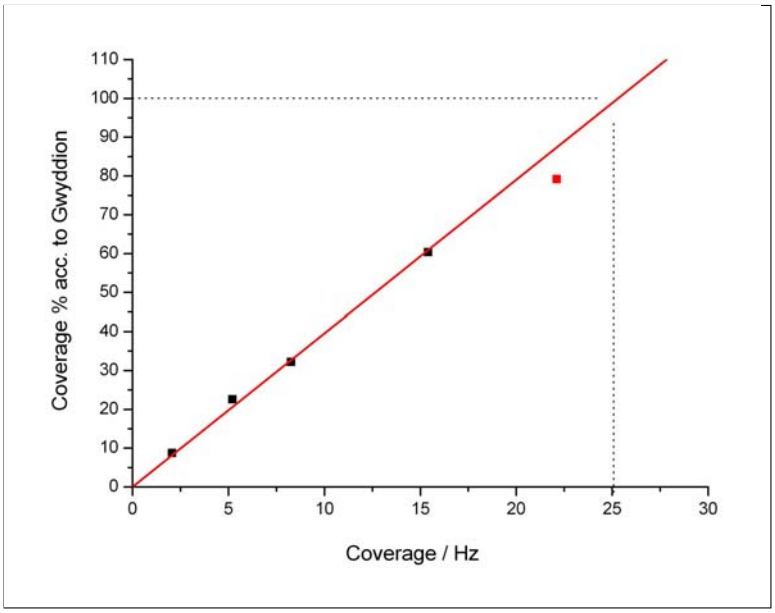

Figure A.3.: **Quartz microbalance thickness calibration.** The coverage of different samples were determined by Gwyddion (chap.A.4) in percentage of a full monolayer. A plot of this coverage vs. the corresponding displayed frequency change in Hz on the quartz microbalance, gives with the linear fit for a full ML 25 Hz.

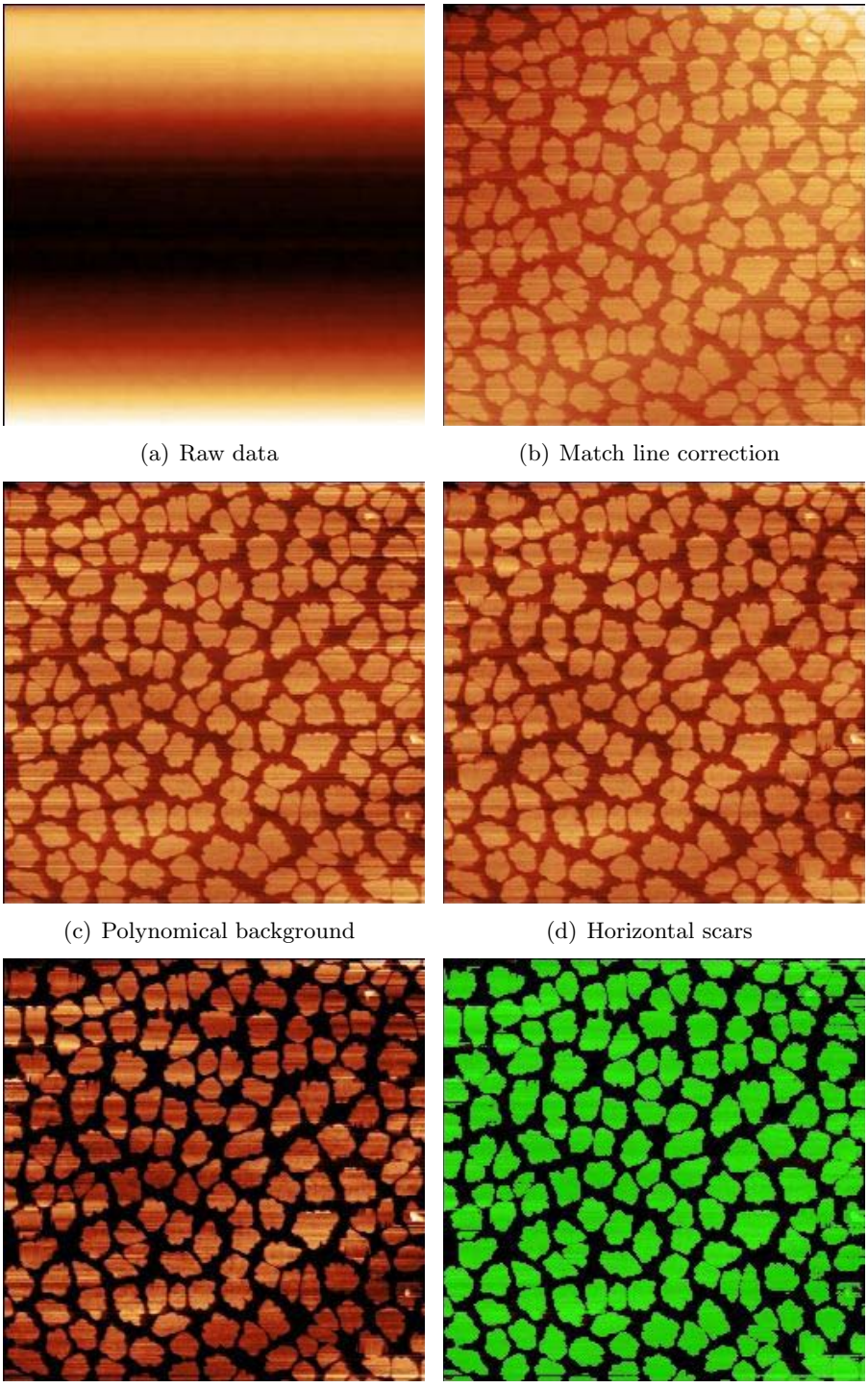

(a) Raw data (b) Match line correction

(c) Polynomical background (d) Horizontal scars

(e) Z-Scale in colours (f) Mask

Figure A.4.: **Treatment and evaluation of the AFM images by Gwyddion.** (a) Raw file of sample 4 (0.61 ML), (b) aligns the individual scan lines, (c) background subtraction, (d) removal of scars, (e) colour height scale, (f) with a mask one can read out the island areas.

A.5. Scaling theory matlab program

For the evaluation of the critical cluster size for nucleation, a matlab program was written as shown below. First the ASCII file (.txt) with the island sizes, exported by gwyddion, will be loaded. A histogram of this data with a selectable bin number is ploted and compared with the scaling function with different i. Note that N_a has the dimension μm^{-4}. The number of bins was chosen as large as possible. Also the AFM images with a mask, marking the individual islands, will be shown. Artefacts like half islands on the boarder, glitches, scars or touching islands in the AFM image, were removed. Some results are shown in fig.4.26 to 4.28.
As an example, the matlab code for sample 3 with average values from all positions is given here.

clear all; close all;
disp('Sample 3: average values of all positions');

$coverage = 0.33$
$bins = 15$
$imagesize = 10^2$

$P_M =' probe3 - posM'_{mask};$
$P_A =' probe3 - posA'_{mask};$
$P_B =' probe3 - posB'_{mask};$
$P_C =' probe3 - posC'_{mask};$
$P_D =' probe3 - posD'_{mask};$

$u_M = load('probe3 - posM.txt');$
$u_A = load('probe3 - posA.txt');$
$u_B = load('probe3 - posB.txt');$
$u_C = load('probe3 - posC.txt');$
$u_D = load('probe3 - posD.txt');$
$u = [u_M; u_A; u_B; u_C; u_D];$

$[n, x] = hist(u, bins);$
$n = n./5;$
$n = n./imagesize;$

$A = sum(u)./length(u). * 10^{(12)}$
$x = x. * 10^{(12)}./A;$

for $d = 1 : bins$
if $x(d) > 3, n(d) = NaN; x(d) = NaN;$ end
if $x(d) < 0.1, n(d) = NaN; x(d) = NaN;$ end
end

$binwidth = (max(u) - min(u)). * 10^{12}/bins;$
$n = n./binwidth;$

$coverage_{computed_M} = sum(u_M) * 10^{(12)}/imagesize$
$coverage_{computed_A} = sum(u_A) * 10^{(12)}/imagesize$
$coverage_{computed_B} = sum(u_B) * 10^{(12)}/imagesize$
$coverage_{computed_C} = sum(u_C) * 10^{(12)}/imagesize$
$coverage_{computed_D} = sum(u_D) * 10^{(12)}/imagesize$
$coverage_{computed} = (coverage_{computed_M} + coverage_{computed_A} + coverage_{computed_B} +$
$coverage_{computed_C} + coverage_{computed_D})/5$
$n = n. * (A)^2./coverage_{computed};$

figure(1)
$u = linspace(0, 3, 1000);$

for $i = 1 : 6$
if $i == 1, b = 0.2715; c =' b'$; end
if $i == 2, b = 0.2976; c =' g'$; end
if $i == 3, b = 0.3086; c =' r'$; end
if $i == 4, b = 0.3145; c =' c'$; end
if $i == 5, b = 0.3182; c =' m'$; end
if $i == 6, b = 0.3207; c =' y'$; end
$C = (i. * b)^{((i+1).*b)}./(b. * gamma((i + 1). * b));$
$f = C. * u.^i. * exp(-b. * i. * u.^(1/b));$
hold on; plot(u,f,c,'LineWidth',2)
end

plot(x,n,'k+:','MarkerSize',15,'LineWidth',3)

$xlabel('/fontsize20/bfa/A');\ ylabel('/fontsize20/bfN_a(/Theta)A^2//Theta');$
$legend('/fontsize20/bfi = 1',\ '/fontsize20/bfi = 2',\ '/fontsize20/bfi = 3',$
$'/fontsize20/bfi = 4',\ '/fontsize20/bfi = 5',\ '/fontsize20/bfi = 6',\ '/fontsize20$
$/bfMeasured,\ MW');$
hold off;

$imageM = imread(P_M,' bmp');$
$imageA = imread(P_A,' bmp');$
$imageB = imread(P_B,' bmp');$
$imageC = imread(P_C,' bmp');$
$imageD = imread(P_D,' bmp');$

figure(2), hold on;
subplot(2,3,1); image(imageM); xlabel('/fontsize15/bf M')
subplot(2,3,2); image(imageA); xlabel('/fontsize15/bf A')

subplot(2,3,3); image(imageB); xlabel('/fontsize15/bf B')
subplot(2,3,5); image(imageC); xlabel('/fontsize15/bf C')
subplot(2,3,6); image(imageD); xlabel('/fontsize15/bf D')
hold off;

A.6. Sample list

In tab.A.2, a list of all samples is shown, the numbers correspond to the chronology. The stated coverage and growth rate is the corrected value according to chapter A.2. The bold typed values show the different values within the coverage, temperature and growth rate series.

Table A.2.: **Sample list**. The stated values are corrected acc. to chap.A.2, T... Substrate temperature, ML... Monolayer.

Sample no.	Coverage ML	T K	Growth rate ML/min
1	**0.08**	300	0.0157
14	**0.21**	**300**	**0.0207**
3	**0.33**	300	0.0340
4	**0.61**	300	0.0238
5	**0.87**	300	0.0199
21	**0.98**	300	0.0175
6	**1.25**	300	0.0265
15	0.22	**150**	0.0252
16	0.22	**200**	0.0258
8	0.21	**250**	0.0231
9	0.20	**350**	0.0189
17	0.21	**400**	0.0231
19	0.12	300	**0.0056**
2	0.24	300	**0.0451**
18	0.26	300	**0.1167**
20	0.27	300	**0.2958**
22	0.27	300	**0.4810**

A.7. AFM images

In this chapter one can see the AFM images of different positions (fig.4.10) on the samples from tab.A.2 measured with the AFM from the University of Leoben. At similar positions, images of all samples were obtained by the AFM from TU Graz, only the sample 17 is shown in fig.A.17 for a comparison.

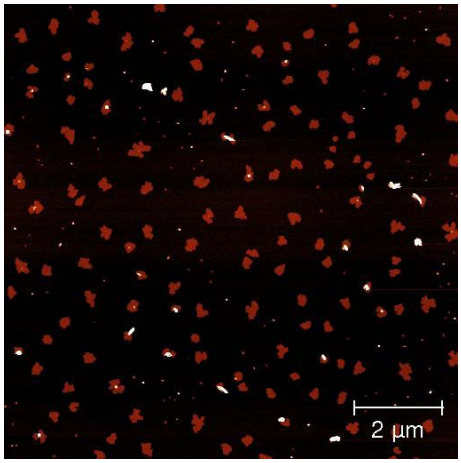

(a) Pos. A

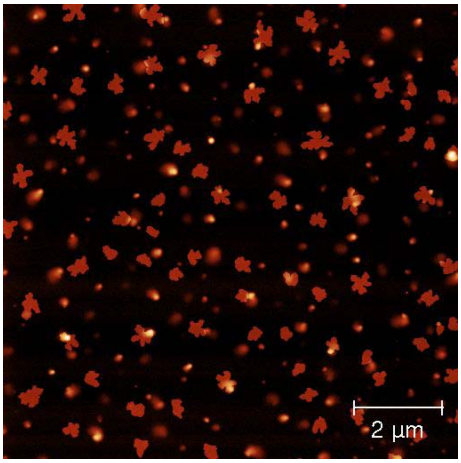

(b) Pos. B

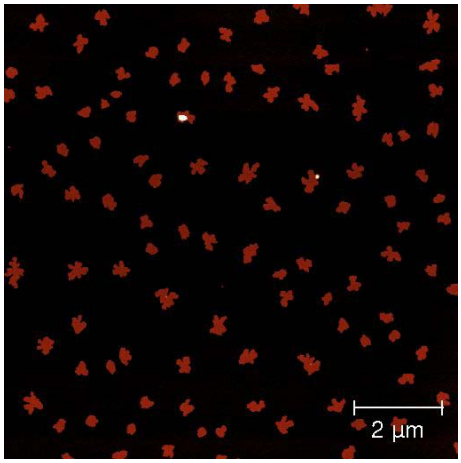

(c) Pos. C

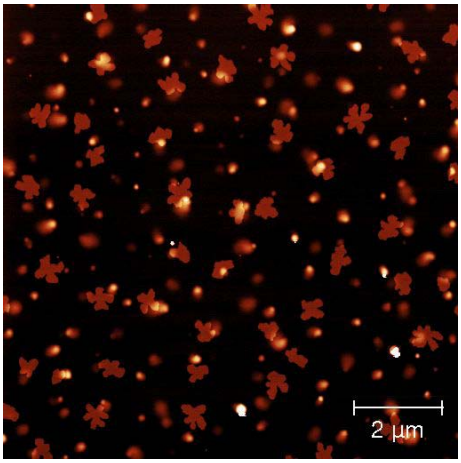

(d) Pos. D

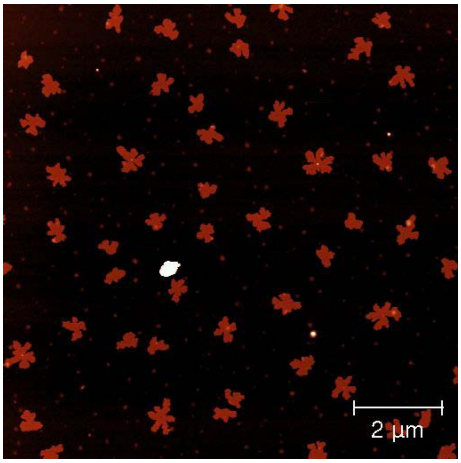

(e) Pos. M

Figure A.5.: **AFM images** ($10x10\ \mu m$) **of sample 1** at different positions acc. to fig.4.10, $\Theta = 0.08\ ML$.

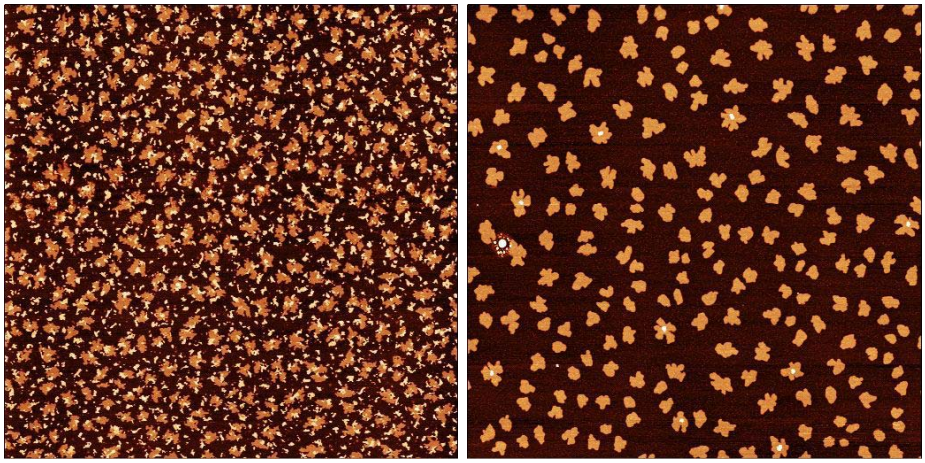

(a) Pos. A

(b) Pos. B

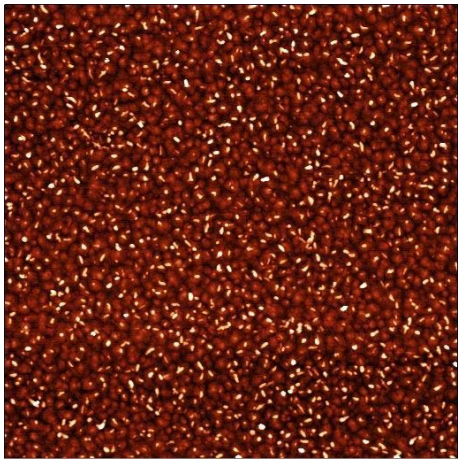

(c) Pos. C

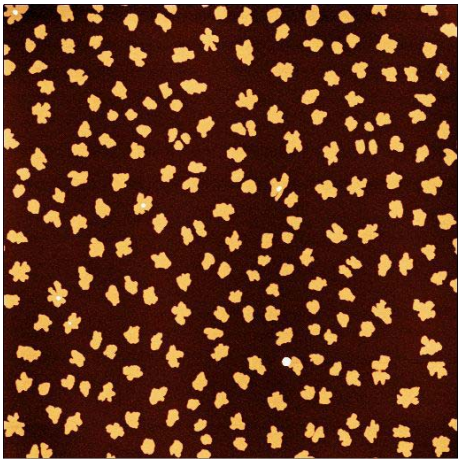

(d) Pos. D

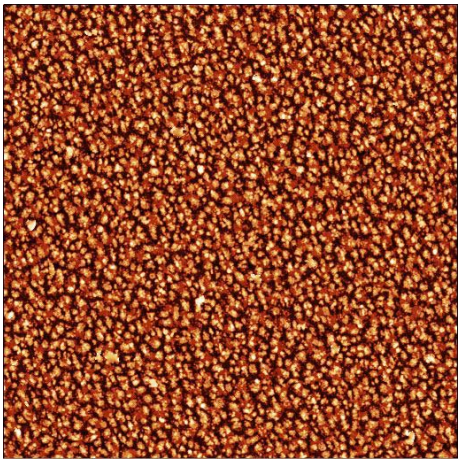

(e) Pos. M

Figure A.6.: **AFM images** ($10x10\ \mu m$) **of sample 14** at different positions acc. to fig.4.10, $\Theta = 0.21\ ML$.

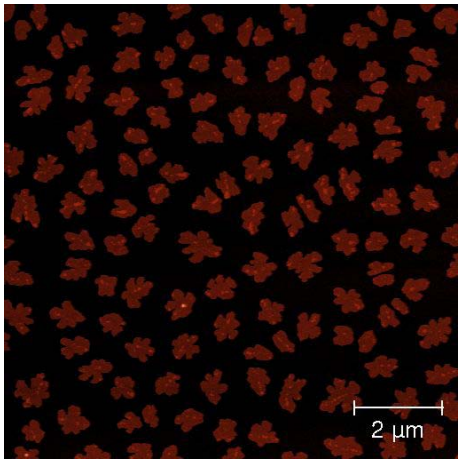

(a) Pos. A

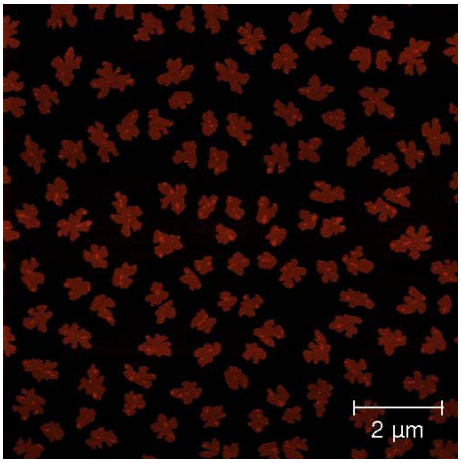

(b) Pos. B

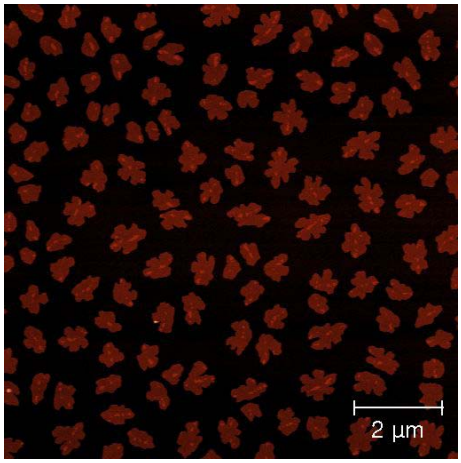

(c) Pos. C

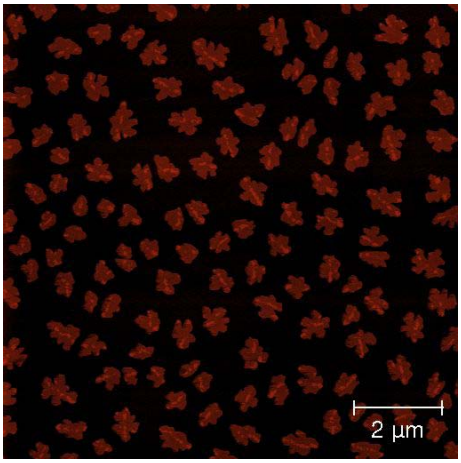

(d) Pos. D

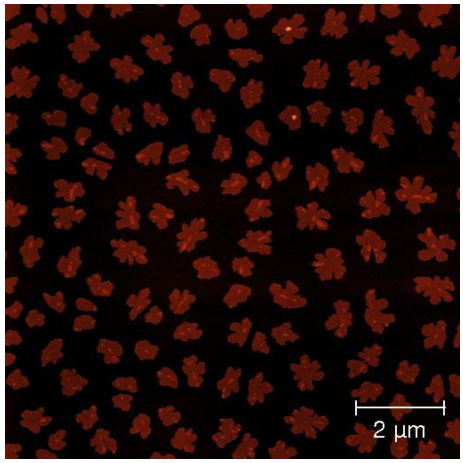

(e) Pos. M

Figure A.7.: **AFM images** ($10x10\ \mu m$) **of sample 3** at different positions acc. to fig.4.10, $\Theta = 0.33\ ML$.

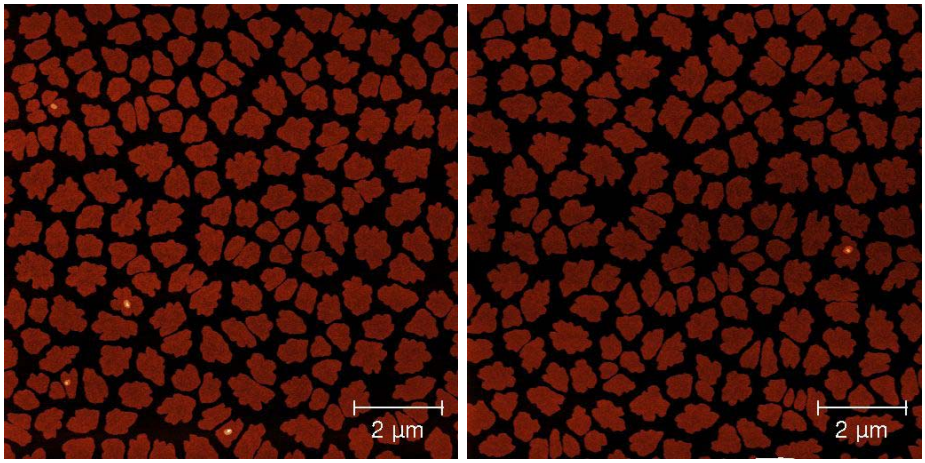

(a) Pos. A (b) Pos. B

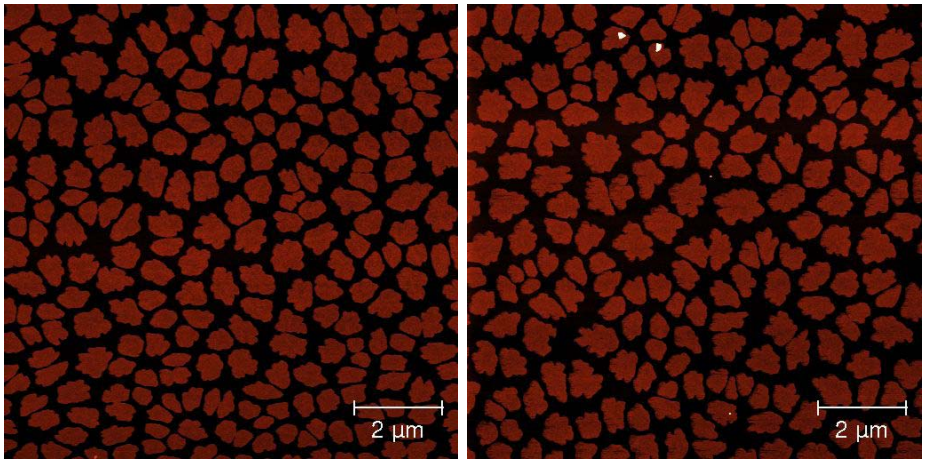

(c) Pos. C (d) Pos. D

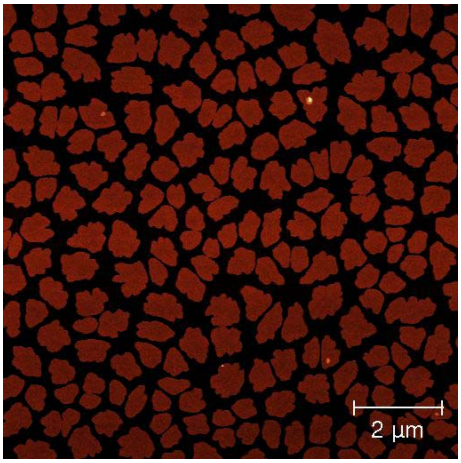

(e) Pos. M

Figure A.8.: **AFM images** ($10x10\ \mu m$) **of sample 4** at different positions acc. to fig.4.10, $\Theta = 0.61\ ML$.

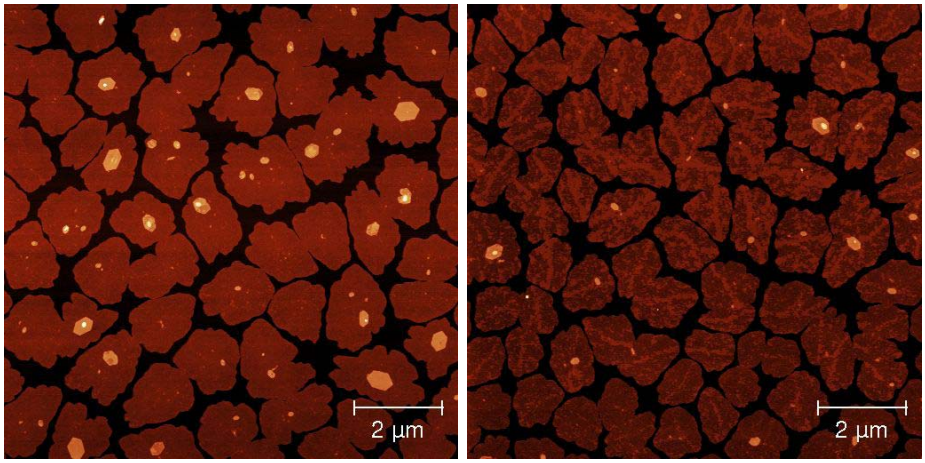

(a) Pos. A (b) Pos. B

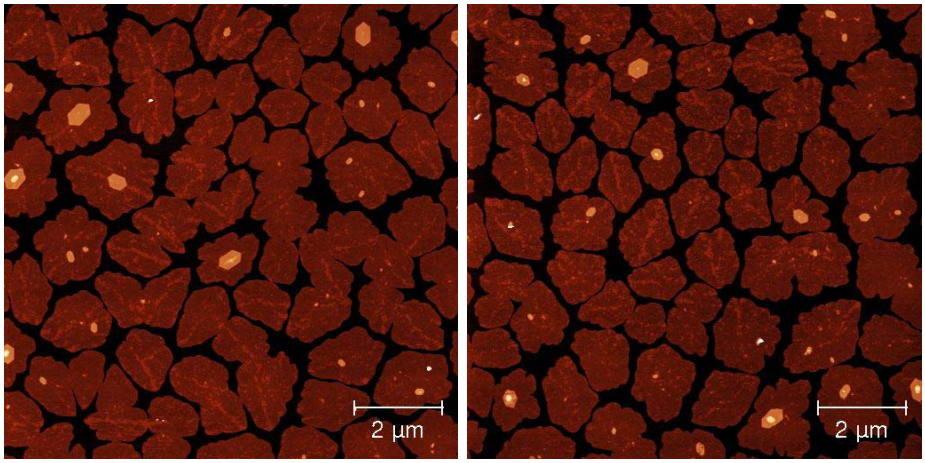

(c) Pos. C (d) Pos. D

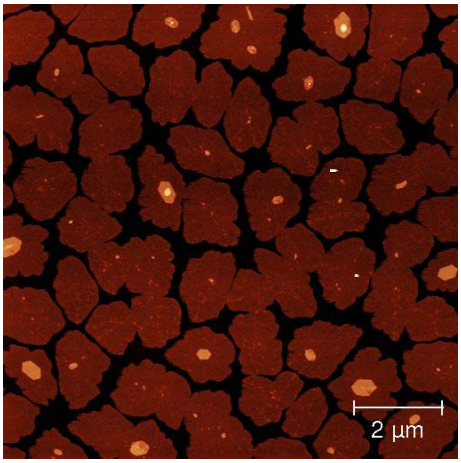

(e) Pos. M

Figure A.9.: **AFM images** ($10x10\ \mu m$) **of sample 5** at different positions acc. to fig.4.10, $\Theta = 0.87\ ML$.

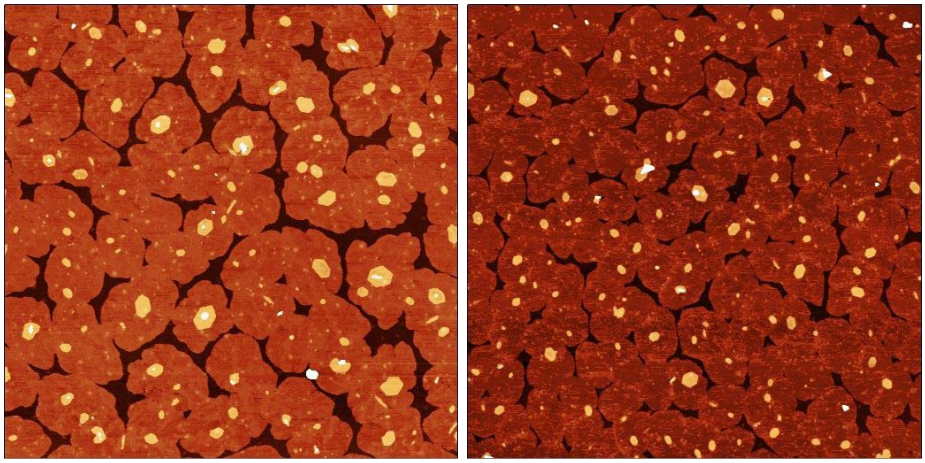

(a) Pos. A

(b) Pos. B

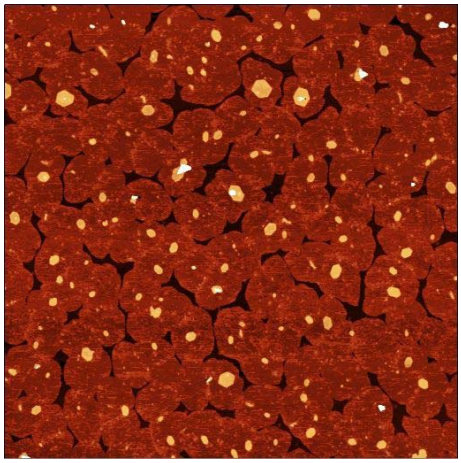

(c) Pos. C

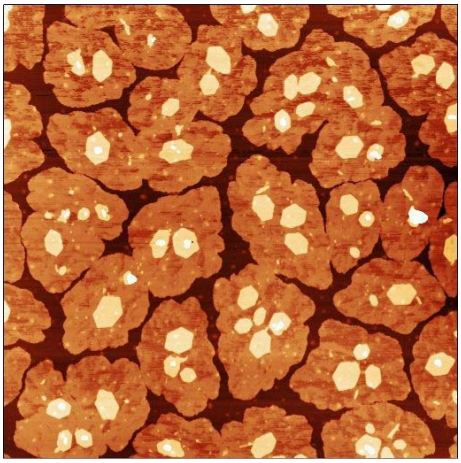

(d) Pos. D

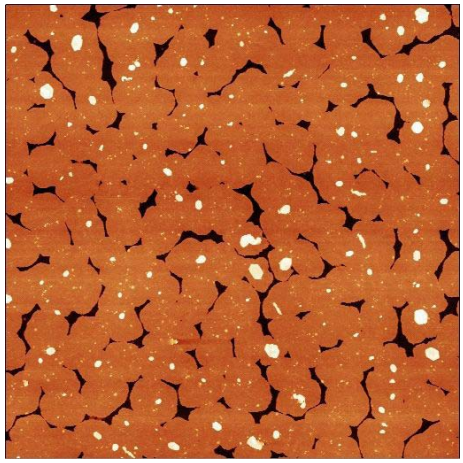

(e) Pos. M

Figure A.10.: **AFM images** ($10x10\ \mu m$) **of sample 21** at different positions acc. to fig.4.10, $\Theta = 0.98\ ML$.

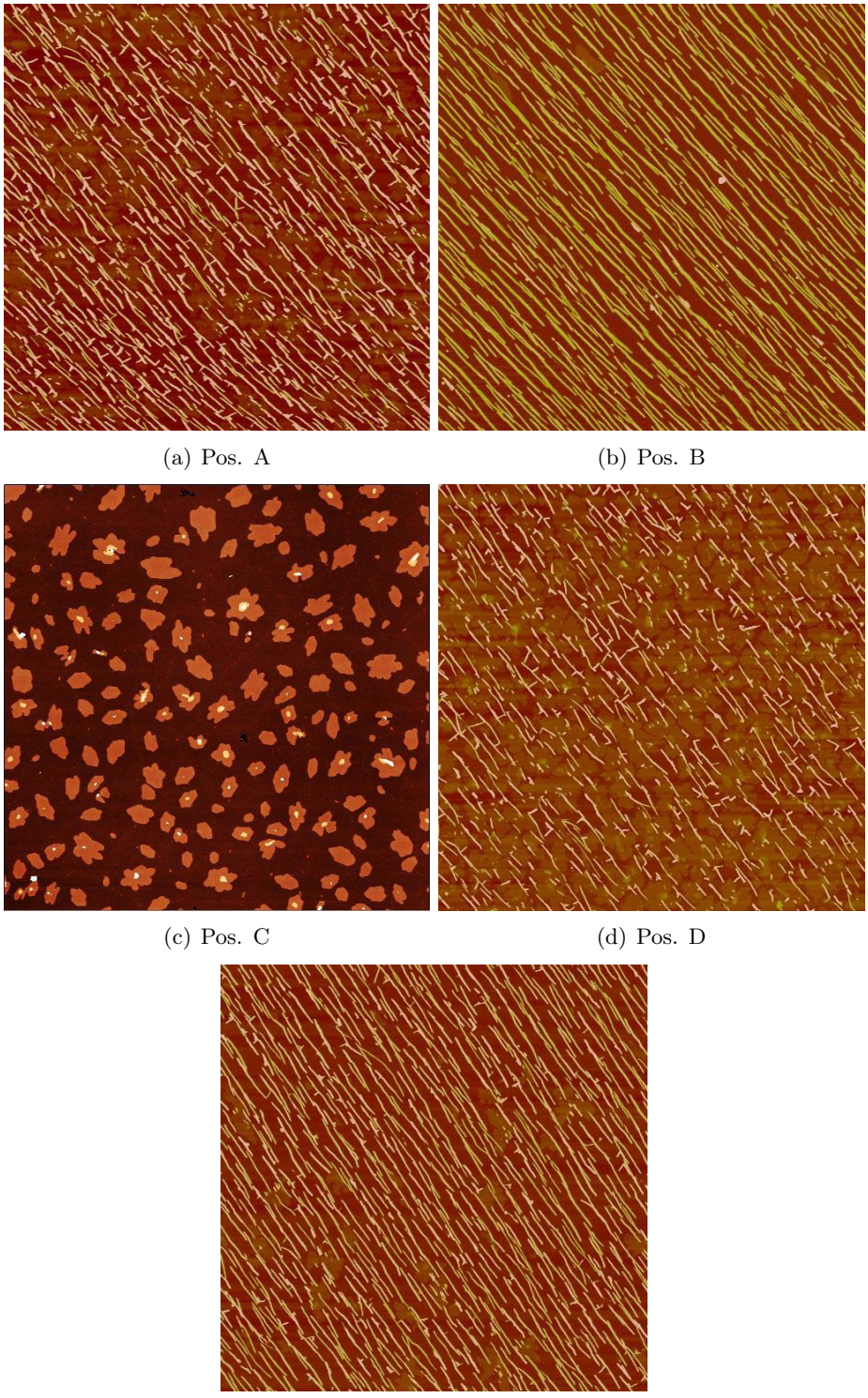

(a) Pos. A

(b) Pos. B

(c) Pos. C

(d) Pos. D

(e) Pos. M

Figure A.11.: **AFM images** ($10x10\ \mu m$) **of sample 6** at different positions acc. to fig.4.10, $\Theta = 1.25\ ML$.

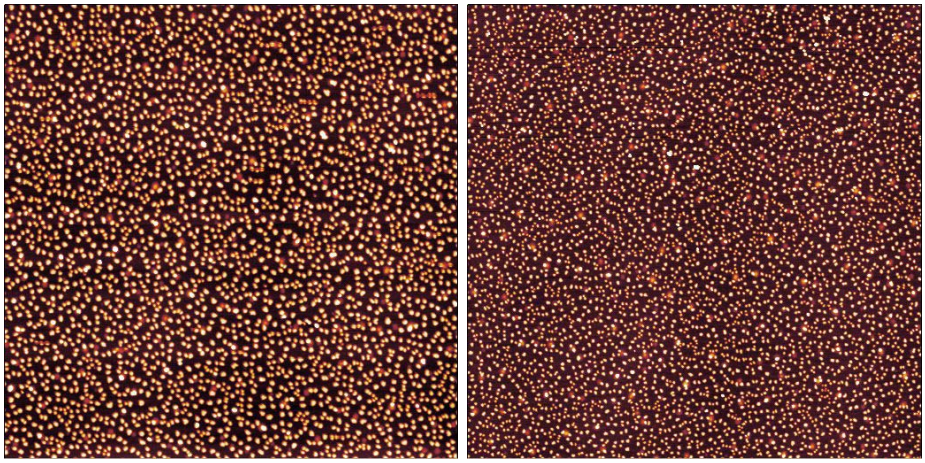

(a) Pos. A

(b) Pos. B

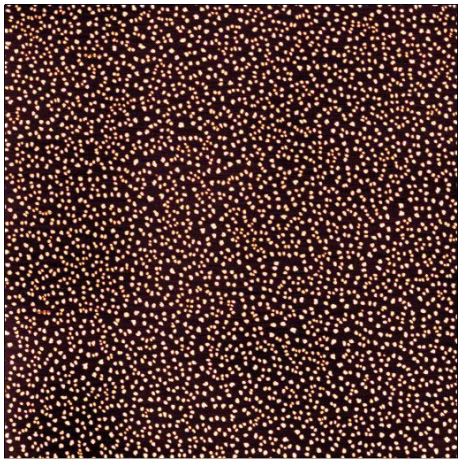

(c) Pos. C

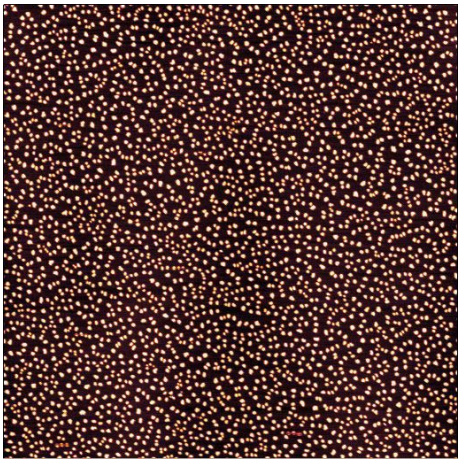

(d) Pos. D

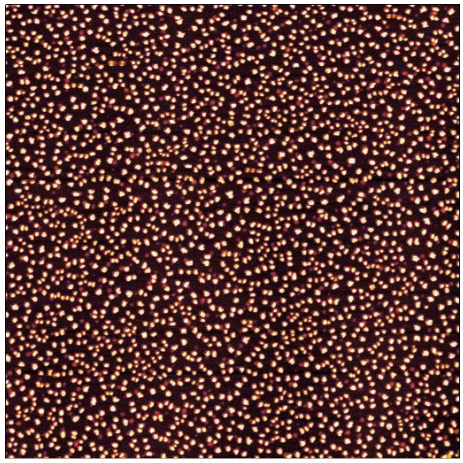

(e) Pos. M

Figure A.12.: **AFM images** ($10x10\ \mu m$) **of sample 15** at different positions acc. to fig.4.10, $T = 150\ K$.

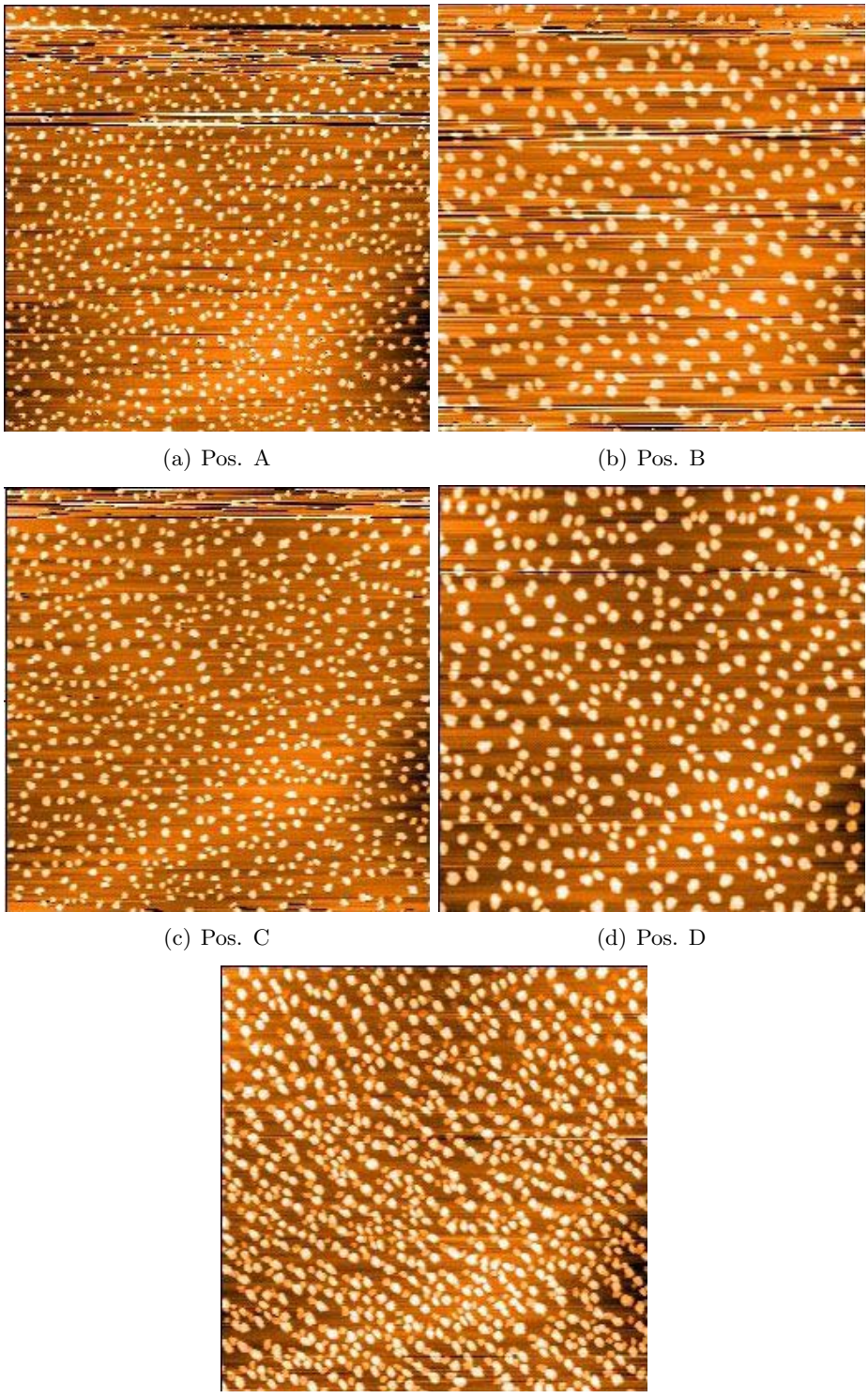

(a) Pos. A

(b) Pos. B

(c) Pos. C

(d) Pos. D

(e) Pos. M

Figure A.13.: **AFM images** ($8.6x8.6\ \mu m$) **of sample 16** at different positions acc. to fig.4.10, only measured by the AFM on TU Graz, $T = 200\ K$.

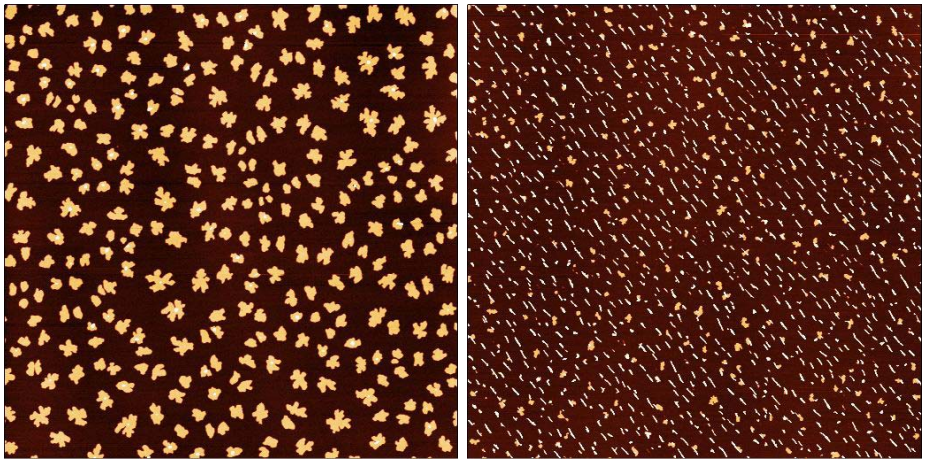

(a) Pos. A

(b) Pos. B

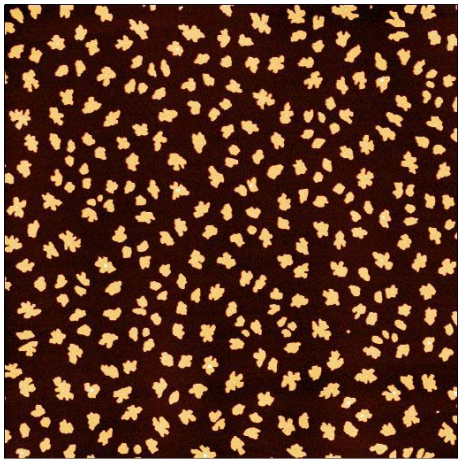

(c) Pos. C

(d) Pos. D

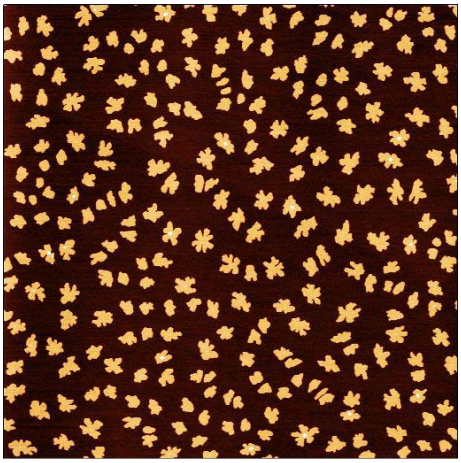

(e) Pos. M

Figure A.14.: **AFM images** ($10x10\ \mu m$) **of sample 8** at different positions acc. to fig.4.10, $T = 250\ K$.

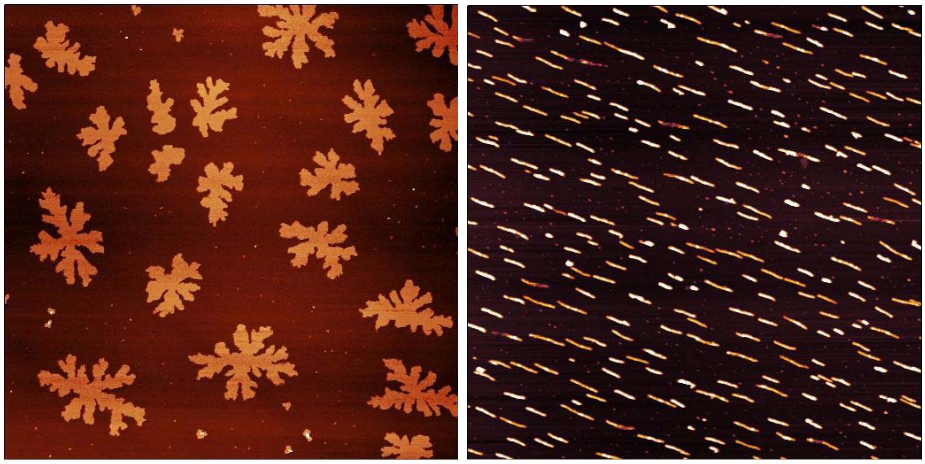

(a) Pos. A

(b) Pos. B

(c) Pos. C

(d) Pos. D

(e) Pos. M

Figure A.15.: **AFM images** ($10x10\ \mu m$) **of sample 9** at different positions acc. to fig.4.10, $T = 350\ K$.

(a) Pos. A

(b) Pos. B

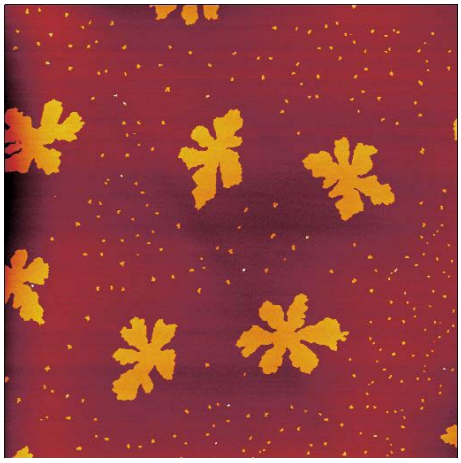

(c) Pos. C

(d) Pos. D

(e) Pos. M

Figure A.16.: **AFM images** ($10x10\ \mu m$) **of sample 17** at different positions acc. to fig.4.10, $T = 400\ K$.

(a) Pos. A

(b) Pos. B

(c) Pos. C

(d) Pos. D

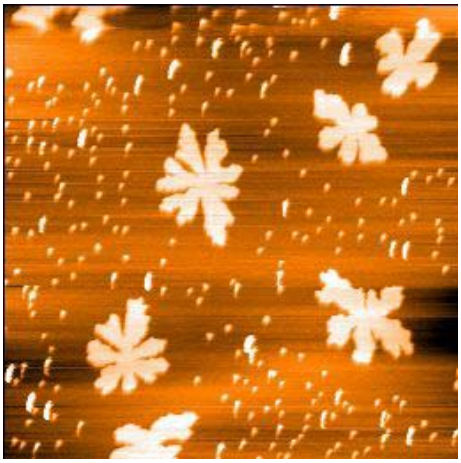

(e) Pos. M

Figure A.17.: **AFM images** ($8.6x8.6\ \mu m$) **of sample 17** at different positions acc. to fig.4.10. This images were obtained by the AFM TU Graz, compare fig.A.16, $T = 400\ K$.

(a) Pos. A

(b) Pos. B

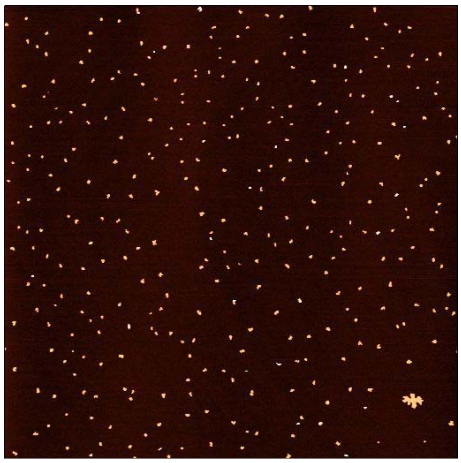

(c) Pos. C

(d) Pos. D

(e) Pos. M

Figure A.18.: **AFM images** ($10x10\ \mu m$) **of sample 19** at different positions acc. to fig.4.10, $r = 0.0056\ ML/min$.

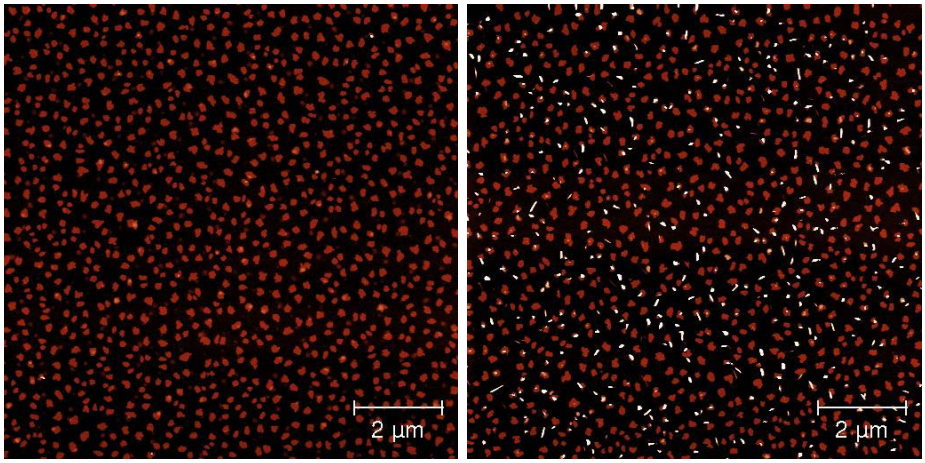

(a) Pos. A (b) Pos. B

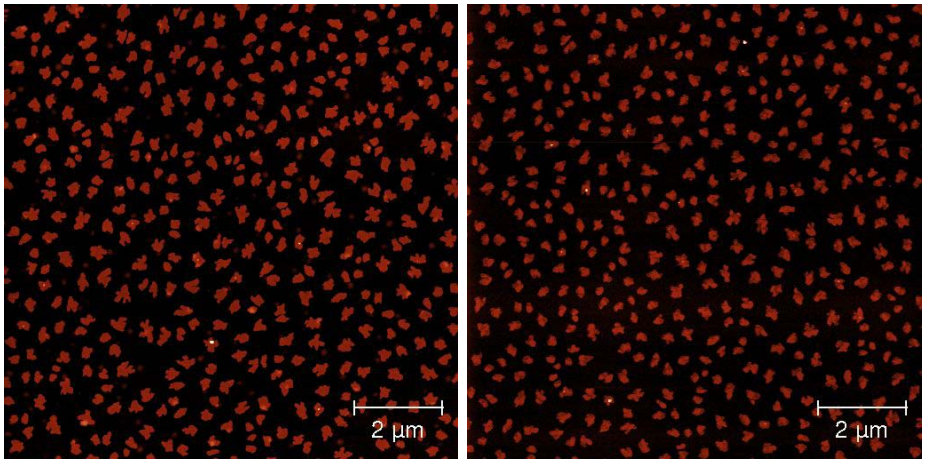

(c) Pos. C (d) Pos. D

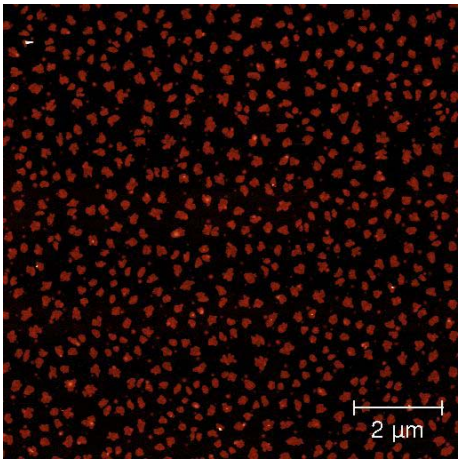

(e) Pos. M

Figure A.19.: **AFM images** ($10x10\ \mu m$) **of sample 2** at different positions acc. to fig.4.10, $r = 0.0451\ ML/min$.

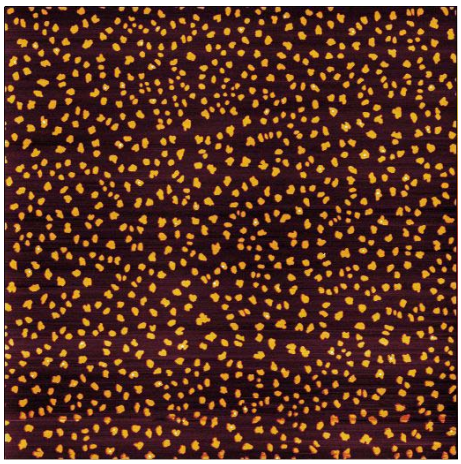

(a) Pos. A

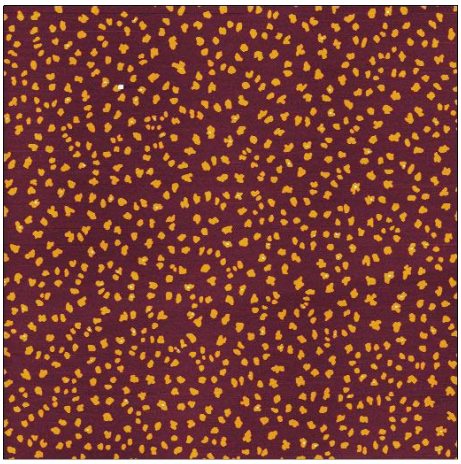

(b) Pos. B

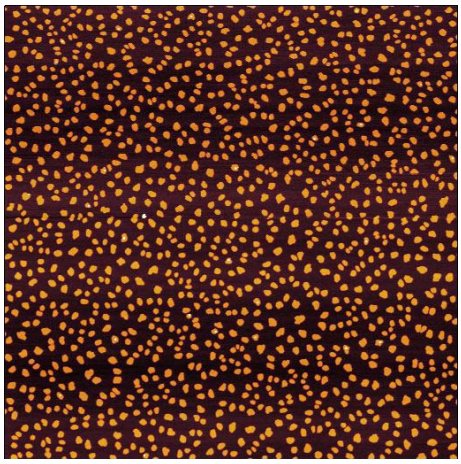

(c) Pos. C

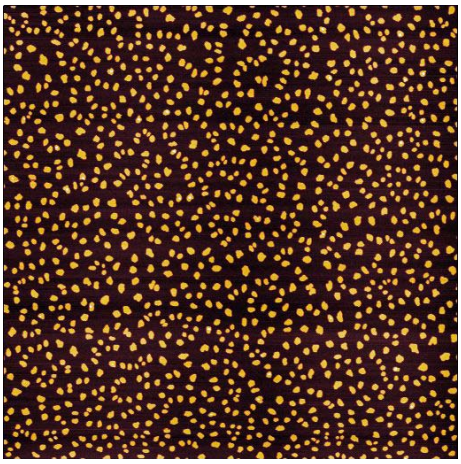

(d) Pos. D

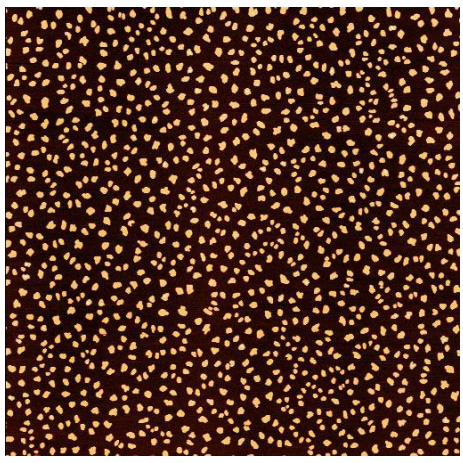

(e) Pos. M

Figure A.20.: **AFM images** ($10x10\ \mu m$) **of sample 18** at different positions acc. to fig.4.10, $r = 0.1167\ ML/min$.

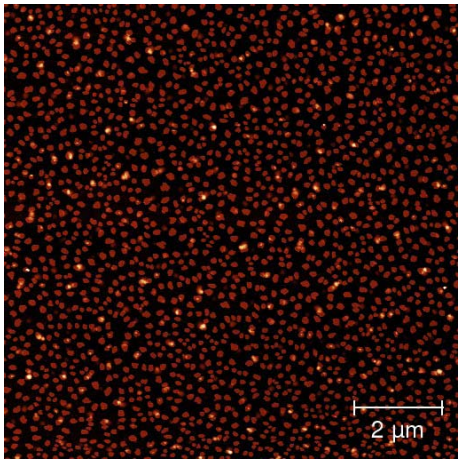

(a) Pos. A

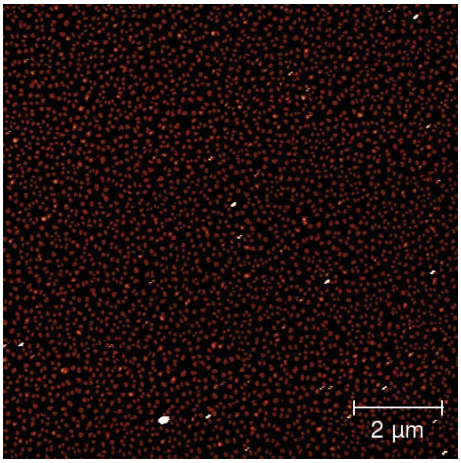

(b) Pos. B

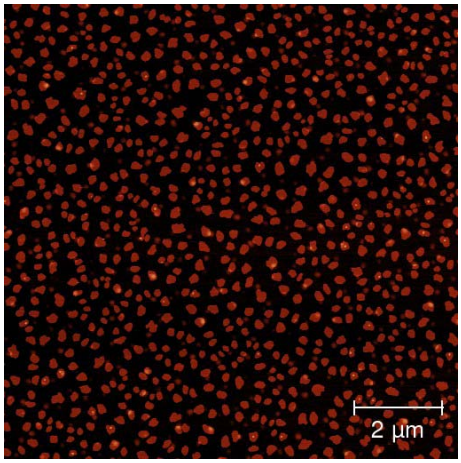

(c) Pos. C

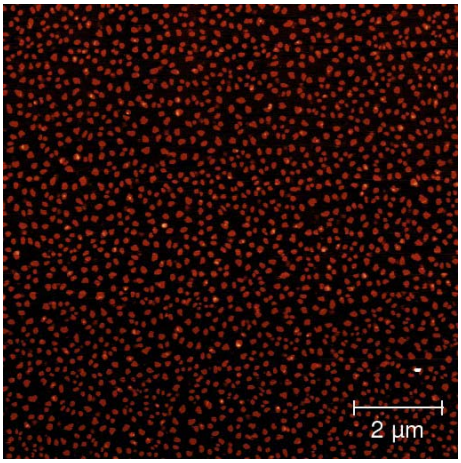

(d) Pos. D

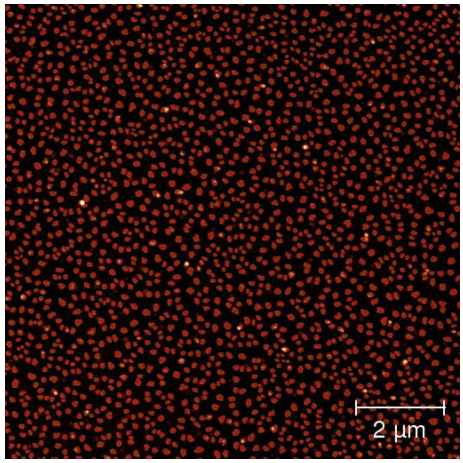

(e) Pos. M

Figure A.21.: **AFM images** ($10x10\ \mu m$) **of sample 20** at different positions acc. to fig.4.10, $r = 0.2958\ ML/min$.

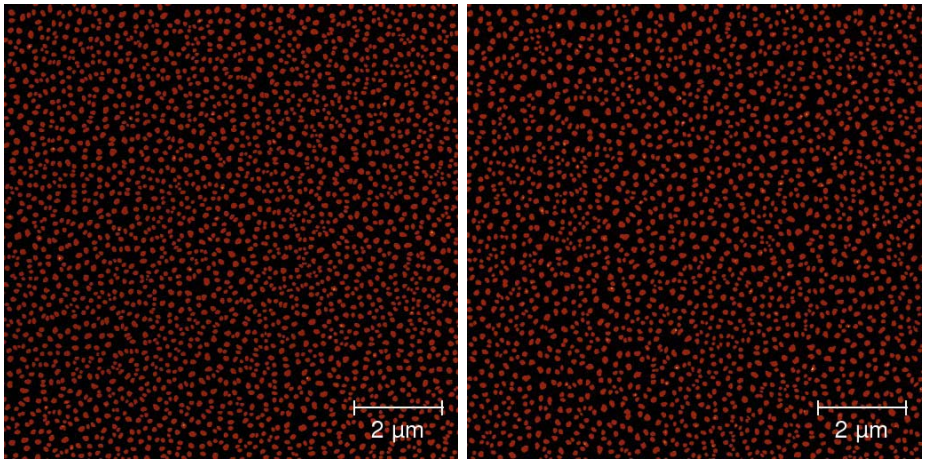

(a) Pos. A (b) Pos. B

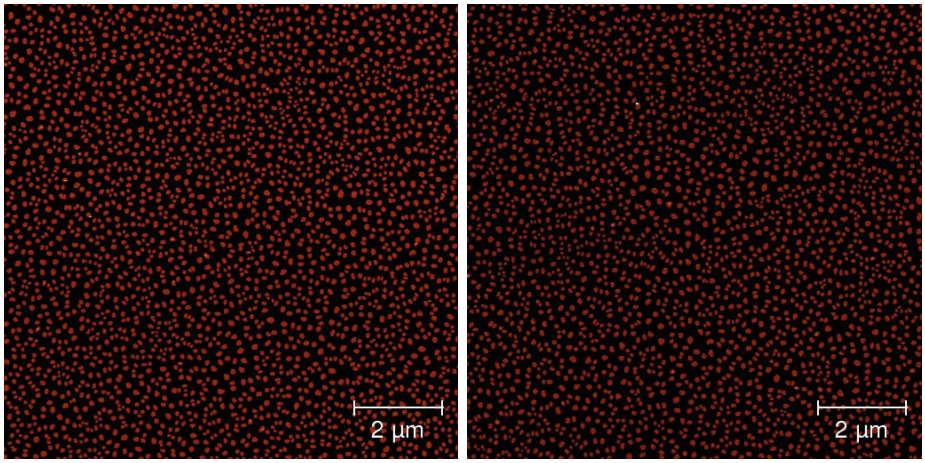

(c) Pos. C (d) Pos. D

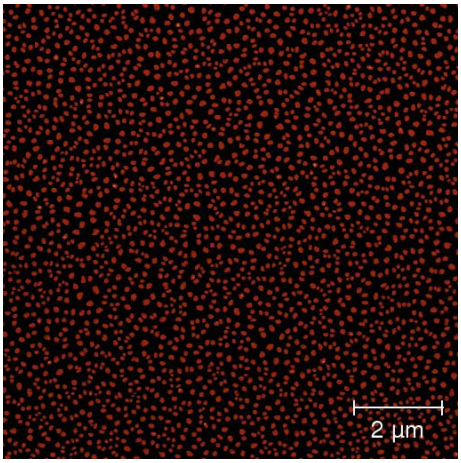

(e) Pos. M

Figure A.22.: **AFM images** ($10x10\ \mu m$) **of sample 22** at different positions acc. to fig.4.10, $r = 0.4810\ ML/min$.

List of Figures

List of Tables

Bibliography

[1] H.E. Katz and J. Huang. Thin-film organic electronic devices. *Annual Review of Materials Research*, 39:71–92, 2009.

[2] S.R. Forrest and M.E. Thomson. Introduction: Organic electronics and optoelectronics. *Chemical Reviews*, 107:923–925, 2007.

[3] T.B. Singh and N.S. Sariciftci. Progress in plastic electronics devices. *Annual Review of Materials Research*, 36:199–230, 2006.

[4] P. Frank. Adsorption, Schichtwachstum und Desorption von p-Hexaphenyl auf Glimmer-Oberflächen. *Master's thesis, TU Graz*, 2006.

[5] A.F. Holleman and E. Wiberg. Lehrbuch der anorganischen Chemie. *de Gruyter*, 1970.

[6] J.A. Venables, G.D.T. Spiller, and M. Hanbucken. Nucleation and growth of thin films. *Reports on Progress in Physics*, 47:399–459, 1984.

[7] K. Oura, V.G. Lifshits, A.A. Saranin, A.V. Zotov, and M. Katayama. Surface science. *Springer*, 2003.

[8] H. Brune. Microscopic view of epitaxial metal growth: nucleation and aggregation. *Surface Science Reports*, 31:121–229, 1998.

[9] T.A. Witten and L.M. Sander. Diffusion-limited aggregation, a kinetic critical phenomenon. *Physical Review Letters*, 47:1400, 1981.

[10] http://apricot.polyu.edu.hk/ lam/dla/.

[11] G.S. Bales and D.C. Chrzan. Transition from compact to fractal islands during submonolayer epitaxial growth. *Physical Review Letters*, 74:4879, 1995.

[12] J. Yang, T. Wang, H. Wang, F. Zhu, G. Li, and D. Yan. Ultrathin-film growth of para-sexiphenyl (i): Submonolayer thin-film growth as a function of the substrate temperature. *The Journal of Physical Chemistry B*, 112:7816–7820, 2008.

[13] R. Ruiz, B. Nickel, N. Koch, L. Feldman, R. Haglund, A. Kahn, F. Family, and G. Scoles. Dynamic scaling, island size distribution and morphology in the aggregation regime of submonolayer pentacene films. *Physical Review Letters*, 91:136102, 2003.

[14] J.G. Amar and F. Family. Critical cluster size: Island morphology and size distribution in submonolayer epitaxial growth. *Physical Review Letters*, 74:2066–2069, 1995.

[15] T. Vicsek and F. Family. Dynamic scaling for aggregation of clusters. *Physical Review Letters*, 52:1669–1672, 1984.

[16] B. Stadlober, U. Haas, H. Maresch, and A. Haase. Growth model of pentacene on inorganic and organic dielectrics based on scaling and rate-equation theory. *Physical Review B*, 74:165302, 2006.

[17] A. Pimpinelli and T.L. Einstein. Capture-zone scaling in island nucleation: Universal fluctuation behavior. *Physical Review Letters*, 99:226102, 2007.

[18] P.W. Palmberg, G.E. Riach, R.E. Weber, and N.C. MacDonald. Handbook of Auger electron spectroscopy. *Physical Electronics Industries, Inc.*, 1972.

[19] G. Ertl and J. Küppers. Low energy electrons and surface chemistry. *Verlag Chemie*, 1974.

[20] SecretDisc. http://de.wikipedia.org/wiki/Cantilever(Mikroskop). 2008.

[21] R.W. Carpick and M. Salmeron. Scratching the surface: Fundamental investigations of tribology with atomic force microscopy. *Chemical Reviews*, 97:1163, 1997.

[22] K. Puntambekar. Structural and electrostatic complexity at a pentacene/insulator interface. *Advanced Functional Materials*, 16:879–884, 2006.

[23] S. Schröder and M. Gottfried. Temperature programmed desorption (TPD) / thermal desorption spectroscopy (TDS). *FU Berlin*, 2002.

[24] P. Frank. Thin film growth of rod-like and disc-shaped organic molecules on insulator and noble metal surfaces. *PhD thesis, TU Graz*, 2009.

[25] Nanosurf. Operating instructions, easyScan 2 AFM. 2005.

[26] Nanosurf. Software reference, easyScan 2. 2005.

[27] P. Klapetek, D. Necas, and C. Anderson. Gwyddion user guide. 2009.

[28] H. Poppa and A.G. Elliot. The surface composition of mica substrates. *Surface Science*, 24:149–163, 1971.

[29] F. Balzer and H.G. Rubahn. Dipole-assisted self-assembly of light-emitting p-nP needles on mica. *Applied Physics Letters*, 79:3860–3862, 2001.

[30] A. Andreev, G. Matt, C.J. Brabec, H. Sitter, D. Badt, H. Seyringer, and N.S. Sariciftci. Highly anisotropically self-assembled structures of para-sexiphenyl grown by hot-wall epitaxy. *Advanced Materials*, 12:629–633, 2000.

[31] R. Resel. Surface induced crystallographic order in sexiphenyl thin films. *Journal of Physics: Condensed Matter*, 20:184009, 2008.

[32] C. Teichert, G. Hlawacek, A.Y. Andreev, H. Sitter, P. Frank, A. Winkler, and N.S. Sariciftci. Spontaneous rearrangement of para-sexiphenyl crystallites into nanofibers. *Applied Physics A*, 82:665–669, 2006.

[33] S. Müllegger. Adsorption and thin film growth of oligo-phenylenes on gold surfaces. *PhD thesis, TU Graz*, 2005.

[34] G. Hlawacek, P. Puschnig, P. Frank, A. Winkler, C. Ambrosch-Draxl, and C. Teichert. Characterization of step-edge barriers in organic thin- film growth. *Science*, 321:108–111, 2008.

[35] P. Frank, G. Hlawacek, O. Lengyel, A. Satka, C. Teichert, R. Resel, and A. Winkler. Influence of surface temperature and surface modifications on the initial layer growth of para-hexaphenyl on mica(001). *Surface Science*, 601:2152 – 2160, 2007.

[36] http://gwyddion.net. 2009.